

# Quantifizierung der physiologischen Belastungsmuster der Tibia von Mäusen mithilfe auf muskuloskelettaler Modellierung basierenden Finite-Elemente-Analysen

DIPLOMARBEIT

zur Erlangung des akademischen Grades

**Diplom-Ingenieurin**

im Rahmen des Studiums

**Biomedical Engineering**

eingereicht von

**Hannah Katharina Fabro, B.Sc.**

Matrikelnummer 11719424

an der Fakultät für Bau- und Umweltingenieurwesen

der Technischen Universität Wien

Betreuung: Associate Prof. Dipl.-Ing. Dr.techn. Stefan Scheiner  
Institut für Mechanik der Werkstoffe und Strukturen, TU Wien

Mitwirkung: Prof. Peter Pivonka, MSc, PhD, DSc  
Maxence Lavaill, PhD  
Natalia Mühl Castoldi, PhD  
School of Mechanical, Medical and Process Engineering, Queensland University of Technology, Brisbane, Australia

Wien, 24. April 2025

  
Hannah Katharina Fabro

Stefan Scheiner



Die approbierte gedruckte Originalversion dieser Diplomarbeit ist an der TU Wien Bibliothek verfügbar  
The approved original version of this thesis is available in print at TU Wien Bibliothek.



# Quantification of habitual loading patterns in the murine tibia using musculoskeletal modeling-informed Finite Element analyses

DIPLOMA THESIS

submitted in partial fulfillment of the requirements for the degree of

**Diplom-Ingenieurin**

in

**Biomedical Engineering**

by

**Hannah Katharina Fabro, B.Sc.**

Registration Number 11719424

to the Faculty of Civil and Environmental Engineering  
at the TU Wien

Advisor: Associate Prof. Dipl.-Ing. Dr.techn. Stefan Scheiner  
Institut für Mechanik der Werkstoffe und Strukturen, TU Wien

Assistance: Prof. Peter Pivonka, MSc, PhD, DSc  
Maxence Lavaill, PhD  
Natalia Mühl Castoldi, PhD  
School of Mechanical, Medical and Process Engineering, Queensland University of  
Technology, Brisbane, Australia

Vienna, April 24, 2025

Hannah Katharina Fabro

Stefan Scheiner



Die approbierte gedruckte Originalversion dieser Diplomarbeit ist an der TU Wien Bibliothek verfügbar  
The approved original version of this thesis is available in print at TU Wien Bibliothek.

# Declaration of Authorship

Hannah Katharina Fabro, B.Sc.

I hereby declare that I have written this Diploma Thesis independently, that I have completely specified the utilized sources and resources and that I have definitely marked all parts of the work - including tables, maps and figures - which belong to other works or to the internet, literally or extracted, by referencing the source as borrowed.

Vienna, April 24, 2025



Hannah Katharina Fabro



# Acknowledgements

Dass die letzten Monate trotz einiger Hürden so reibungslos und positiv verliefen, ist einigen Personen zu verdanken, die ich hier nennen möchte.

Als allererstes will ich mich bei **Stefan Scheiner** für seine unglaublich geduldige, verständnisvolle und erstklassige Betreuung meiner Arbeit bedanken. Nicht nur hat er ohne Kommentar und Klagen die Entwicklung meiner Arbeit weg von seinen Kernexpertisen hingenommen und mich stets bei meinen Unternehmungen unterstützt, was das Einholen von Hilfe von externen Personen anging oder das Sicherstellen, dass nötige Software auf meinem Rechner zeitnah installiert wird. Zusätzlich dazu hat er auch keinerlei Mühe gescheut, präzise Antworten auf meine oft langen E-Mails innerhalb sehr kurzer Zeit zu produzieren oder Zeit für mich freizuschaukeln, wenn ich sie benötigte (auch früh morgens noch aus dem Home-Office). Dafür möchte ich mich mit ganzem Herzen und Verstand bedanken, da ich weiß, dass das absolut nicht selbstverständlich ist.

Als nächstes möchte ich mich bei **Peter Pivonka** bedanken, der mich - nicht zuletzt durch das Ermutigen für die Einreichung eines Abstracts über meine Arbeit bei einem Symposium der International Society of Biomechanics - ebenfalls unglaublich unterstützt und gefördert hat. Da es sich bei dem Konzept für die Arbeit um Peters Idee handelte, war es auch er, der mir unglaublich viele Antworten und neue Inputs, häufig auch ohne mein Einfordern, innerhalb kürzester Zeit zur Verfügung gestellt hat und bereitwillig gemeinsame Meetings spät nachts durchführte und damit den Zeitunterschied zwischen Wien und Brisbane verschwindend gering erscheinen ließ.

Ich bin sehr glücklich, euch zu meinen Riesen zählen zu können.

Außerdem geht mein Dank an / Furthermore, I'd like to thank ...

... **Max Lavaill**, for his humorous support at the beginning of my work and his willingness to answer all kinds of questions both in meetings and via email. Also for patiently tracking down information in 12116 lines of code when I was once again unable to see the wood for the trees.

... **Natalia Mühl Castoldi**, for patiently transferring the Finite Element model from Ansys to Abaqus, explaining the process to me in many mails and answering many questions on the (non-)existence and location of nodes. And all of the other guidance she provided me with in the last months.

... **Sebastian Pech**, für seine Unterstützung mit Abaqus und seine sehr geduldigen und ausführlichen Antworten auf all meine E-Mails mit Fragen.

... **James Charles**, for providing the updated mouse model and his advice on what results to go on with.

... **Corinna Modiz**, für ihren emotionalen Support und die hin und wieder mein Postfach schmückenden aufmunternden Botschaften sowie ihren Rat.

... **Jana Kümmerlin**, für's Korrekturlesen und ihre fachfräuischen Anmerkungen zu muskuloskelettalen Modellen.

... **Jan Vales**, der mir stets mit Problemen den Cluster betreffend geholfen hat.

Und zu guter Letzt möchte ich mich auch bei meiner Schwester Lisa, meinem Freund Johannes und meiner Schwiegermama Margaret bedanken, die mich mit ihren Worten, Gedanken und Anmerkungen die Dinge etwas klarer sehen ließen.



Die approbierte gedruckte Originalversion dieser Diplomarbeit ist an der TU Wien Bibliothek verfügbar  
The approved original version of this thesis is available in print at TU Wien Bibliothek.

# Kurzfassung

Das Mausmodell ist das am häufigsten verwendete Tiermodell, um Fragen der Mechanobiologie des Skeletts zu untersuchen, und es existieren zahlreiche Datensätze über die Reaktion auf externe mechanische Belastung und den Knochenumbau. Derzeit werden die räumlich-zeitlichen Dehnungsmuster des Knochens, auf denen eine Vielzahl von Algorithmen zur Knochenanpassung basiert, aus dem Tibiakompressionstest gewonnen, der den Vorteil hat, dass die externe Belastung des Knochens auf wiederholbare Weise erfolgt. Gleichzeitig wird die Belastung jedoch auf eine unnatürliche, unphysiologische Weise herbeigeführt. Stattdessen würden Daten über die Spannungen und Dehnungen, die durch gewohnheitsmäßige Belastungen wie Gehen oder Laufen hervorgerufen werden, eine bessere Ausgangsbasis darstellen, die bisher in der Literatur jedoch nicht vorhanden sind.

Um diesen Mangel zu beheben, haben wir eine Modellierungspipeline für die Bewertung der Spannungs- und Dehnungsmuster in der Tibia der Maus während der Standphase entwickelt. Zu diesem Zweck wurde ein muskuloskelettales Modell eines Maus-Hinterlaufs verwendet, um physiologische Belastungsbedingungen für den nachfolgenden Finite-Elemente-Analyseschritt zu erhalten. Dazu gehören Gelenkreaktionskräfte und -momente sowie die Kräfte der Muskeln, die am proximalen Teil der Tibia ansetzen.

Spannungen und Dehnungen sowie Biege- und Torsionsmomente wurden für vier Zeitpunkte während der Standphase in zwei Abschnitten von Interesse (37% und 50% vom proximalen Ende des Knochens aus gesehen) bestimmt. Maximale (Druck-/Zug-)Spannungen und Dehnungen traten sowohl im 37%- als auch im 50%-Abschnitt entlang der Längsrichtung auf, mit  $-86.09/87.11$  MPa und  $-4937/5086 \mu\epsilon$  bzw.  $-127.4/123.6$  MPa und  $-7424/7302 \mu\epsilon$ . Das größte Biegemoment trat entlang der nach posterior gerichteten Achse mit  $0.0131$  Nm auf, gefolgt von  $0.0107$  Nm entlang der nach lateral gerichteten Achse. Das maximale Torsionsmoment erreichte  $0.0017$  Nm. Um verschiedene Anwendungen dieser Technik zu untersuchen, wurden drei verschiedene Simulationseinstellungen getestet, und es wurde festgestellt, dass Muskeln, wie sie im Modell realisiert wurden und die in der Nähe eines interessierenden Abschnitts ansetzen, keine starken Auswirkungen auf die Spannungs- und Dehnungsprofile in diesem Abschnitt haben.

Eine Reihe von Einschränkungen dieser Studie muss hervorgehoben werden. Erstens übersteigen die ermittelten Spitzendehnungen die in-vivo-Messungen erheblich. Die Ursachen für diese Diskrepanz müssen noch ermittelt werden. Zweitens wurde festgestellt, dass eine Erhöhung des Elastizitätsmoduls nicht unbedingt zu einer Verringerung der Spannungen und Dehnungen in den Abschnitten führte, was nicht erwartet wurde und wofür mögliche Erklärungen gegeben werden. Drittens ergaben sich bei weiteren Tests des Finite-Elemente-Modells widersprüchliche Ergebnisse hinsichtlich der Verringerung der Muskelkräfte, deren Ursachen ebenfalls noch unbekannt sind. Schließlich haben die kinematischen und kinetischen Inputs für das Muskel-Skelett-Modell auch gewisse Schwachstellen, welche sich negativ auf Qualität und die Genauigkeit des Endergebnisses auswirken könnten.

Trotz dieser Einschränkungen kann der entwickelte Ansatz als ein bedeutender Schritt über den Stand der Technik auf diesem Gebiet hinaus betrachtet werden, und die Einschränkungen können als Grundlage für künftige Forschungsrichtungen dienen, um den derzeitigen Arbeitsablauf weiter zu verbessern.



# Abstract

The mouse model is the most commonly used animal model to address questions in skeletal mechanobiology, and ample data exist on the response to external mechanical loading and bone remodeling. Currently, bone spatio-temporal strain patterns, on which a variety of bone adaptation algorithms are based, are obtained from the tibial compression test, which has the advantage that the external loading of the bone is done in a repeatable way. However, at the same time, the loading is induced in an unnatural, non-physiological way. Instead, data on the stresses and strains induced by habitual loading such as walking or running would serve as a better baseline, which so far do not exist in literature.

To address this short-coming, we developed a modeling pipeline for the assessment of stress and strain patterns in the mouse tibia during the stance phase. To achieve this, a musculoskeletal mouse hindlimb model was employed to obtain physiological loading conditions for the subsequent FE analysis step. These include joint reaction forces and moments as well as forces of muscles attaching to the proximal part of the tibia.

Stresses and strains, as well as bending and torsional moments were determined for four time points during the stance phase in two sections of interest (37% and 50% viewed from the proximal end of the bone). Maximum (compressive/tensile) stresses and strains arose both in the 37% and 50% section along the longitudinal direction, with  $-86.09/87.11$  MPa and  $-4937/5086$   $\mu\epsilon$  and  $-127.4/123.6$  MPa and  $-7424/7302$   $\mu\epsilon$ , respectively. The largest bending moment arose along the axis pointing posteriorly with  $0.0131$  Nm, followed by  $0.0107$  Nm along the axis pointing laterally. The maximum torsional moment reached  $0.0017$  Nm. To investigate different applications of this technique, three different simulation settings were tested and it was found that muscles as realized in the model and which attach near a section of interest do not have strong effects on the stress and strain profiles in that section.

A number of limitations of this study must be emphasized. Firstly, the obtained peak strains substantially exceed *in-vivo* measurements. The sources for this mismatch remain to be identified. Secondly, it was found that increasing the elastic (tensile) modulus did not necessarily reduce the stresses and strains experienced by the sections, which was not expected and for which possible explanations are given. Thirdly, inconsistent results regarding the reduction of muscle forces arose upon further testing of the Finite Element model, the sources for which are also still unknown. Finally, the kinematic and kinetic inputs for the musculoskeletal model also have certain weaknesses that could have a negative impact on the quality and accuracy of the final result.

Despite these limitations, the developed approach may be considered a significant step beyond the state of the art in the field, and the limitations may serve as basis for future research directions, further improving the present workflow.



# Contents

<b>Kurzfassung</b>	ix
<b>Abstract</b>	xi
<b>Contents</b>	xiii
<b>1 Introduction</b>	1
1.1 Structure and function of bones . . . . .	1
1.2 Bone's adaptive response to mechanical loading . . . . .	4
1.3 Animal models for structural adaptations to mechanical loading . . . . .	7
1.4 Alternative approach to determining habitual strain states . . . . .	7
1.5 Description of used methodologies . . . . .	8
1.6 Objective of this work . . . . .	9
<b>2 Methods</b>	11
2.1 Musculoskeletal modeling . . . . .	11
2.2 Data processing . . . . .	16
2.3 Finite Element modeling . . . . .	17
<b>3 Results</b>	23
3.1 Musculoskeletal model . . . . .	23
3.2 Finite Element model . . . . .	27
<b>4 Discussion</b>	43
4.1 Musculoskeletal modeling outcomes . . . . .	43
4.2 Finite Element modeling outcomes . . . . .	49
4.3 Limitations . . . . .	54
<b>5 Conclusion</b>	55
<b>6 Appendix</b>	57
<b>List of Figures</b>	59
<b>List of Tables</b>	61
<b>Bibliography</b>	63



# Introduction

Ever since the first publication of Harold M. Frost [1987] on the mechanostat and subsequent publications on the Utah paradigm (Frost [1997, 2000, 2003]), knowledge about the loading response of bone has become essential to be able to describe the remodeling processes of bone tissue.

## 1.1 Structure and function of bones

Contrary to popular belief, bone is a very dynamic tissue that is constantly repairing and renewing itself to replace brittle bone with new bone tissue and ensure proper calcium homeostasis (Teitelbaum [2007], Rucci [2008], Katsimbri [2017]). Whereas both bone modeling (formation and shaping) and bone remodeling (replacement and renewal) occur in early childhood, bone remodeling predominates in adulthood, with the exception of fracture healing. In order to guarantee both sufficient rigidity and at the same time a minimum of construction material and thus sufficient freedom of mobility, a large part of the bone consists of dense outer cortical and inner trabecular bone. Bone not only gives the body shape, protects internal organs, and provides attachment points for muscles, but also serves as a reservoir for bone marrow and other minerals (Crockett et al. [2011]).

The process of bone tissue renewal is carried out by osteoclasts, osteoblasts and osteocytes, which are each responsible for resorption, new bone formation and control of the process, respectively (Crockett et al. [2011]). Their activity therefore significantly determines the skeletal mass (Teitelbaum [2007]).

### 1.1.1 Bone cell types

Osteoclasts attach themselves to sites of bone resorption before resorbing the underlying bone. The site is then released and the process is either repeated at other sites or, to prevent excessive resorption, stopped by osteoclast apoptosis. Osteoclasts are of hematopoietic origin and develop by fusion of monocytes or macrophages located in the bone marrow (Teitelbaum [2007], Crockett et al. [2011], Kenkre and Bassett [2018]).

Osteoblasts are responsible not only for the formation of new bone on surfaces or in cavities, but also for the differentiation of osteoclast precursors into osteoclasts and thus indirectly for bone resorption. Furthermore, they are responsible for the mineralization of the extracellular matrix and may even have endocrine functions in bone. They are of mesenchymal origin and develop into osteocytes or bone-lining cells (Karsenty et al. [2009], Crockett et al. [2011]).

Osteocytes are the successors of former osteoblasts that, during the process of new bone formation, are engulfed by neighboring osteoblasts in the newly formed osteoid layer. Due to the loss of a large part of their cell organelles during this process, osteocytes are then no longer able to make their original contribution to the growth or remodeling of the tissue. Instead of undergoing apoptosis, they form long extensions through the matrix along small channels (called canaliculi) in order to make contact with other osteocytes in their respective lacunae

## 1. Introduction

and osteoblasts on the surface. This network of gap junctions is thought to be responsible for the active regulation of bone turnover, ion exchange and functional adaptation of bone (Lanyon [1993], Aarden et al. [1994]).

A fourth type of cell, also a successor to osteoblasts and involved in the process of bone remodeling, is the bone lining cell. It is assumed that by covering all surfaces not currently undergoing remodeling, these cells serve to prevent inappropriate interactions of osteoclast precursors with intact bone (Chambers et al. [1985], Kular et al. [2012]).

The overarching goal of the communicating network of osteocytes and osteoblasts is to establish and maintain a structurally appropriate bone architecture. This is achieved by sensing changes in dynamic mechanical loading, processing the associated load-related information and subsequently regulating the continuous remodeling processes in response to the change in load (Lanyon [1993], Bonewald and Johnson [2008]).

### 1.1.2 Bone cell differentiation

This remodeling cycle, which takes place constantly but asynchronously at many different sites in the skeleton, is regulated by cellular and molecular mechanisms (Kenkre and Bassett [2018]).

For remodeling to occur, the cells must be fully differentiated. This process is governed by different molecules due to the different embryonic origins of the cells (Karsenty et al. [2009]) (see Figure 1.1).

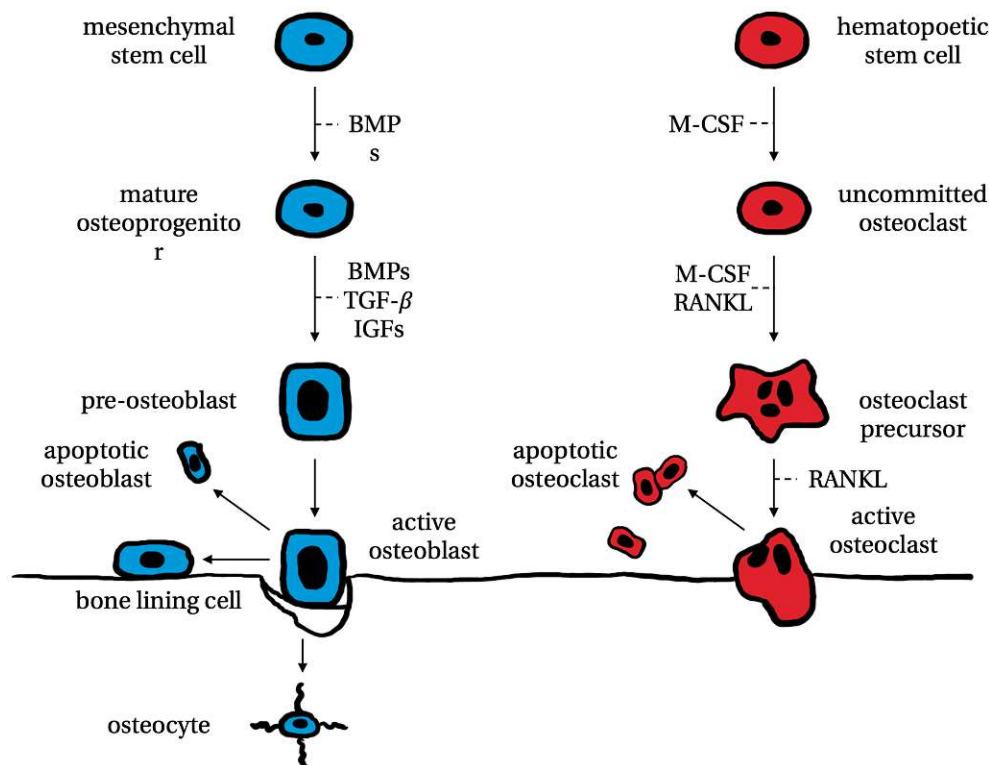


Figure 1.1: Differentiation paths of osteoblast and osteoclast cells including most important factors needed - adapted from Pivonka and Komarova [2010].

The most important osteoclastogenic cytokine is the receptor activator of the nuclear factor  $\kappa$  B ligand (RANKL). When RANKL - itself a tumor necrosis factor (TNF) protein, located in the cell membrane of osteoblasts and their precursors - binds to RANK - its receptor in the cell membrane of bone marrow macrophages -, the bone marrow macrophage is induced to develop into an osteoclast cell (see Figure 1.2). (Teitelbaum [2007]) The expression of RANK itself is stimulated by macrophage colony stimulating factor (M-CSF) even before the fusion of bone marrow macrophages into osteoclast precursor cells. The expression of both factors,

RANKL and M-CSF, is necessary for the survival of the osteoclast even in its mature adult form (Crockett et al. [2011]).

RANK activity in the bloodstream is regulated by osteoprotegerin (OPG), which, like RANKL, is produced by osteoblasts and stromal cells and competes as a decoy receptor with RANKL for binding sites on RANK (see Figure 1.2) (Teitelbaum [2007], Crockett et al. [2011]).

Tumor necrosis factor- $\alpha$ , another factor that positively influences osteoclastogenesis, occurs primarily in inflammatory osteolysis, but also in postmenopausal osteoporosis. Whether TNF- $\alpha$  alone promotes osteoclast differentiation is controversial, but there is evidence that TNF- $\alpha$  has a strong synergistic relationship with RANKL (Teitelbaum [2007]).

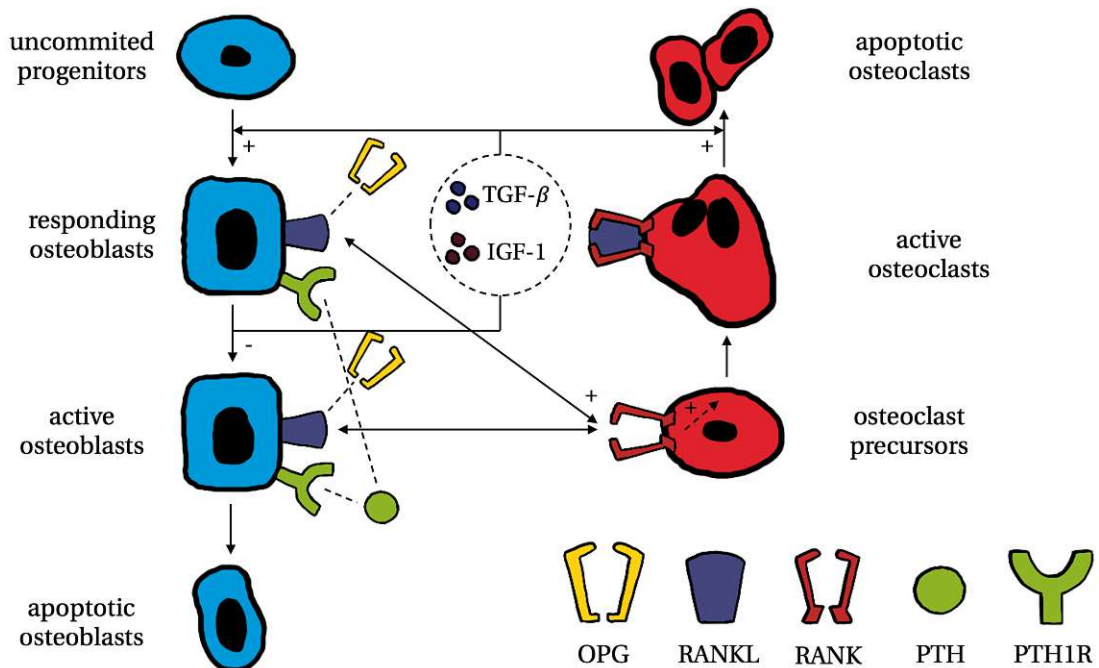


Figure 1.2: Interplay between different cytokines - adapted from Pivonka et al. [2008].

As already mentioned, osteoblasts develop from stromal mesenchymal stem cells. The bone morphogenetic protein (BMP) and the wntless signaling pathway (Wnt) are used for this purpose. For the penultimate developmental step from osteoprogenitor cell to pre-osteoblast cell, parathyroid hormone (PTH) comes into play, which also prevents apoptosis of mature osteoblasts and osteocytes. Finally, the last differentiation step is initiated by insulin-like growth factor 1 (IGF-1), which also plays a role in osteoclast formation (upregulation of RANKL) (Crockett et al. [2011]).

### 1.1.3 Bone remodeling

Bone remodeling can be divided into five phases (see Figure 1.3) (Rucci [2008], Kenkre and Bassett [2018]):

1. Activation phase: Resting osteoblasts on the bone surface (lining cells) are activated by indicators (e.g. altered mechanical stress, presence of certain factors [IGF1, TNF- $\alpha$ , PTH]). This leads to an increased expression of RANKL by the osteoblasts, which subsequently interact with RANK on pre-osteoclasts, causing them to fuse and differentiate into multinucleated osteoclasts. The bone surface is exposed by the lining cells lifting off and forming a raised canopy over the surface to be resorbed.
2. Resorption phase: Osteoclasts attach to the surface and begin to dissolve the bone by acidifying the matrix and releasing lysosomal enzymes for the inorganic and organic components, respectively. Growth factors (BMPs and transforming growth factor (TGF)- $\beta$ ) are released from the matrix and attract osteoblasts.

## 1. Introduction

3. Reversal phase: Although not yet fully researched, it is assumed that the newly created area is prepared for new bone material deposition by cells of the osteoblast lineage by creating a cement line (mineralized matrix) and ensuring that no net bone loss occurs. It is easier for subsequent osteoblasts to attach to this cement line.
4. Formation phase: Recruited osteoblasts produce new bone matrix, which initially consists of collagen-rich osteoid and is mineralized in a secondary step. Subsequently, the osteoblasts differentiate further into lining cells, osteocytes or undergo apoptosis.
5. Termination phase: Bone lining cells cover the newly formed bone in order to prevent further degradation.

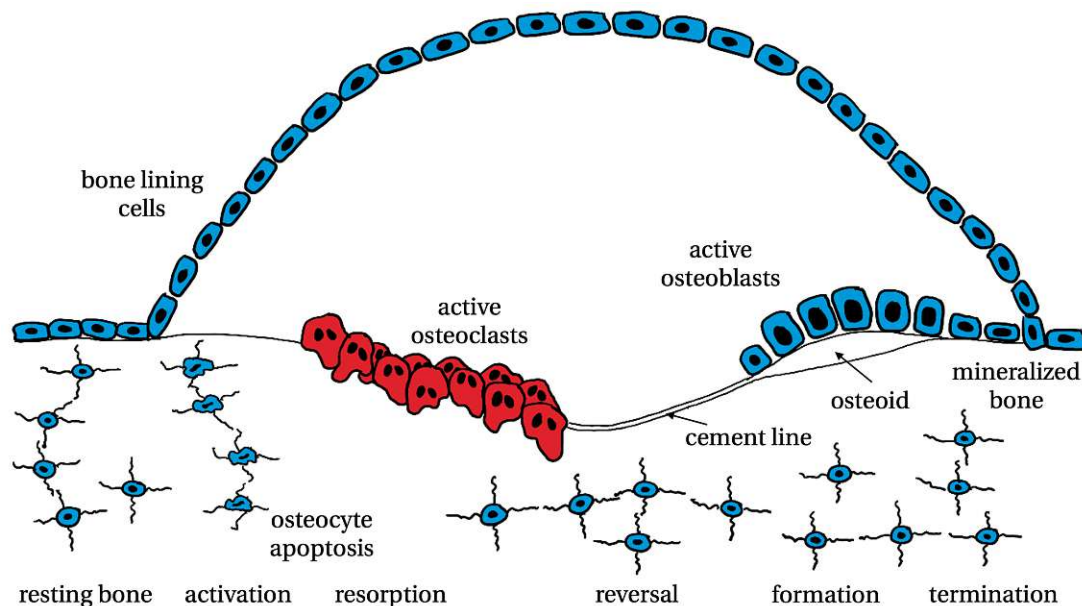


Figure 1.3: The bone remodeling cycle - adapted from Kenkre and Bassett [2018].

## 1.2 Bone's adaptive response to mechanical loading

As already briefly mentioned, the functionality of the skeleton is maintained by constant adjustments to the bone architecture in response to load. In doing so, the body follows the principle set out in Utah Paradigm, Proposition 1: *“Healthy skeletal organs provide only enough strength to keep postnatal voluntary loads, whether chronically subnormal, normal or supra-normal, from causing spontaneous fractures, ruptures, arthroses, or pain.”* (Frost [2000]) This ensures that the maintenance and operation of a body is as energy-efficient as possible, while at the same time retaining a safety margin that protects against fractures in the event of falls and blows (Currey [1984], Pivonka et al. [2017]).

### 1.2.1 Historical background

However, Frost was not the first person to notice this connection between load and bone architecture. As early as in the 17th century, Galileo Galilei [1638] discovered that bones adapt more to the load-bearing capacity than to the size of an animal and thus increase more in circumference than in length (Pivonka et al. [2017]). In the early 19th century, Jean Baptiste Marc Bourgerie [1832] and Charles Bell (1834) established the maximum-minimum principle (Roesler [1987]): *“A maximum of strength of bone is achieved with a minimum of constructional material.”* (Fung and Skalak [1981]) This was extended 35 years later in 1867 by an anatomist named Georg Hermann von Meyer [1867] and an engineer named Karl Culmann, by the realization that the direction of principal stresses determines the structure of cancellous bone, derived from the comparison of crane structures with the internal structure of femurs. At the end of the [1867] publication, von Meyer asked rather rhetorical whether it was possible for the

observed structures to be formed by static conditions, as well as what the internal “metamorphosis” was that would shape these structures in this way, and whether these structures could also be understood in this way if the influence of ligaments and muscles were added to the static loads (Roesler [1987]).

Two years later, Julius Wolff [1869] published the first answers to the questions posed by von Meyer and thus became the center of interest regarding the study of the structure of compact and cancellous bone. In Wolff [1869] and subsequent works, he described two important points: 1) a mathematical description of the connection between the structure of the bone and the structure of the trajectories in Culmann's crane published by von Meyer, and 2) the statical relevance and necessity of the structure of bones. In 1881, another anatomist, Wilhelm Roux [1881], developed the theory of functional adaptation, which contradicted Wolff's original view but was supported by Wolff three years after publication. Thus the three findings, that of the maximum-minimum principle by Bourguery and/or Bell, the trajectory hypothesis by Wolff and the theory of functional adaptation by Roux, were combined under one name; Wolff's Law. The law was challenged several times, for example by Christian Otto Mohr, a pioneer of several seminal concepts of engineering mechanics, such as Mohr's circle or the Mohr-Coulomb failure criterion, and was religiously defended not only by Wolff himself (Roesler [1987]). Ultimately, however, the exact mathematical description of the trajectory hypothesis was refuted (Evans [1957], Hayes and Snyder [1981]). The question of which factors would influence the orientation and remodeling of osteons remained open, however, since ever since the publication of Evans [1957], speculations existed that mechanical stress could not be the only determining factor (Roesler [1987]).

However, not least due to developments in finite element analysis to calculate stress distributions in elastic bodies, Hayes and Snyder [1981] were able to present a quantitative formulation of Wolff's Law. They proved that there is a highly significant connection between calculated stresses and bone-architectural parameters, and that Wolff's trajectory hypothesis is indeed correct, but not the mathematical laws established at the time (Roesler [1987]).

### 1.2.2 Frost's mechanostat

Wolff's law, along with the minimum-maximum principle and the theory of functional adaptation, indicate that the body responds to increased loads with stronger, more mechanically competent bones to improve load distribution. One indicator of how well the body is able to distribute the loads to the load-bearing mineralized matrix is the "habitual" strain state of the bone (Pivonka et al. [2017]). As a control variable, this strain state is also most likely to direct the behavior of osteocytes and their associated surface osteoblasts (Lanyon [1993]).

Mechanical strain is the ratio of the deformation (new length minus the original length) divided by the original length and as such is dimensionless. Common magnitudes of strain in mammalian long bones under physiological loading are  $10^{-4}$  to  $10^{-3}$   $\mathcal{E}$ , which is why the term microstrain ( $\mu\mathcal{E} = 10^{-6}\mathcal{E}$ ) is often used (Pivonka et al. [2017]).

Strain and strain rates can be measured using strain gauges, mostly applied to the midshaft of long bones away from muscle attachment sites (Burr et al. [1996], Fritton and Rubin [2001], De Souza et al. [2005], Sugiyama et al. [2012], Patel et al. [2014]). While in most animals the functional peak strains during walking are between 200 and 1000  $\mu\mathcal{E}$ , in humans, strains occur in the range of 400 to 650  $\mu\mathcal{E}$ . At higher loads such as running, galloping racehorses can reach almost 5000  $\mu\mathcal{E}$ , while humans are assumed to experience 600 to 1000  $\mu\mathcal{E}$ . The highest strains measured in humans were triggered by drop jumps and reached a magnitude of 1900 to 2100  $\mu\mathcal{E}$  (Burr et al. [1996], Yang et al. [2011]).

Frost called the mechanism that converts typical mechanical load/strain into signals that can be processed by bone and other skeletal tissues and initiate the above-mentioned processes in bone *mechanostat*. As an experimental basis, he refers to *in-vivo* studies by Lanyon [1984], Jaworski et al. [1980], Jaworski [1984], Jee et al. [1983], Wronski and Morey [1982, 1983a,b] that demonstrated an increase in cortical bone mass with stress in the range of 1500-2500  $\mu\mathcal{E}$  and a decrease in cortical bone mass with stress below 300  $\mu\mathcal{E}$ . Based on these experiments, Frost hypothesized that bone adapts to both gross overload and gross underload, with the above values representing the thresholds for the respective ranges. Between them is the range in which bone is subject to the natural bone remodeling process (see Figure 1.4) (Frost [1987]).

## 1. Introduction

This view that a certain amount of peak strain determines the onset of the remodeling process is now viewed as outdated. As Skerry [2006] points out, the mechanostat theory has long been misunderstood and peak strain magnitude has been elevated to one of the main indicators, which has no justification in its sole supremacy. Bones, of which there exist also multiple different types, react to a complex, locally acting strain stimulus, which is determined by a multitude of different parameters, of which peak strain magnitude is only one. Others include genetic constitution, age, sex, concomitant diseases, availability of nutrients and exposure to drugs or biochemicals. There can therefore be no universal number on which the setting of the mechanostat is based (Skerry [2006]).

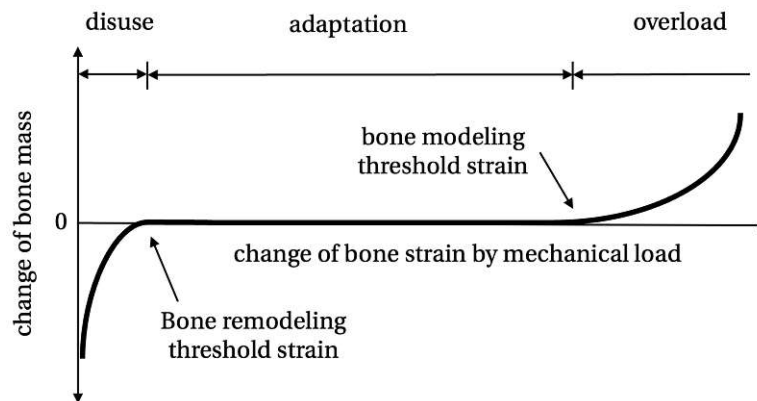


Figure 1.4: Homeostatic bone adaptation mechanism proposed by Frost [1987] - adapted from Sugiyama et al. [2002].

Although the content must be treated with some caution, for the sake of completeness it should also be discussed how Frost and his colleagues imagined the mechanostat to work:

According to Frost [2000], mature bone reacts by removing bone tissue near the bone marrow if dynamic strains remain below the threshold for bone remodeling (within the by Frost coined *disuse window*), resulting in a decrease in bone strength and mass ("resorption modeling"). For strains within the adaptation zone (also called 'lazy zone'), the above described bone remodeling process occurs to preserve existing bone mass (Schönau [1996]). However, if the *bone modeling threshold strain* is exceeded during dynamic loading, mechanically controlled modeling begins to take effect. The bone reacts and again starts modeling processes, this time to increase the local strength with the aim of reducing subsequent strains ("formation modeling") (Frost [2000]). This is implemented either by additional tissue accumulation or by changes of the micro- and macroarchitecture (Takahashi [1995], Forwood and Turner [1995]). The two set points marking the lower and upper limits of the adaptation zone are also called *minimum effective strain(s)* (*MESr and MESm*), for remodeling and modeling, respectively.

### 1.2.3 Alternative hypothesis proposed by Lanyon

In parallel, another hypothesis exists by Lanyon [1987, 1996] based on the idea that bones have a genetically determined minimum mass and that, depending on strain-related stimuli, bone mass builds up in a linear fashion. This counteracts the effect of a (probably hormonally mediated) net drive for resorption, where removal or reduction of the strain-related stimulus consequently results in bone loss.

The concept of a "lazy zone" is therefore not supported. Although the "lazy zone" was demonstrated experimentally (Turner et al. [1994]), it may have resulted from the study design, as no adaptive changes below a certain peak strain could be demonstrated in healthy bones when artificial and natural loads were present in parallel. A further study done by Rubin and Lanyon [1985], which excluded precisely this by making natural loading surgically impossible, supports the linear hypothesis.

A reason for why both theories are still accepted despite not complementing each other is that both give explanations for observed behavior, as Sugiyama et al. [2012] point out.

### 1.3 Animal models for structural adaptations to mechanical loading

Various *in-vivo* and *in-vitro* models have been developed to determine which type of stimulus drives functional adaptation and which cells of the bone translate the mechanical stimuli into tissue adaptation. On the one hand, forces can be applied intrinsically, for example by muscles, or by surgical manipulation of a part of the skeleton in the form of an osteotomy, in which the neighboring regions subsequently experience higher loads. On the other hand, forces and moments can be applied extrinsically by a loading system that applies external pressure to the bone to be deformed, or by the existence of a counterforce such as ground reaction forces (Pivonka et al. [2017]).

Examples of these non-invasive approaches that include a loading system are four-point-bending devices paired with sham loading (lateral compression of long bones without inducing bending) (Turner et al. [1991]), cantilever models (cups on knee and ankle to introduce bending) (Gross et al. [2002]) and axial loading of ulnae of rats (Torrance et al. [1994], Mosley et al. [1997]).

Due to the similarity of the tissue reactions in the form of microtears and stress fractures to those observed in humans, the ulnar loading model has been adopted by numerous groups and used for further studies. Repeated cyclic loading over a large number of cycles is central to the experimental procedure. Due to the development of microcracks and smaller fractures, the ulnar loading model is also used in the investigation of bone remodeling (Pivonka et al. [2017]).

Based on this model, axial loading was applied to the mouse tibia (De Souza et al. [2005]) (called tibial compression test), which had the advantage of triggering both an adaptive reaction in the diaphysis and reactions in the cancellous bone of the metaphysis. As a result, both the ulnar and tibial axial loading models became favored models for studying mechanobiological processes (Pivonka et al. [2017]).

The tibial compression test is a controlled pressure test of the tibia using specially manufactured padded loading cups. After anaesthetizing the test animal, the load is applied over the knee and tarsus during several loading cycles using the loading cups in order to imitate overloading (see Figure 1.5). After the end of the experiment and euthanasia of the test animal, the changes in the architecture of the tibia are analyzed. However, the tibia itself does not have direct contact with the loading cups, as for physiological reasons the load can only be applied via the distal part of the femur and the flexed tarsal bone. As a result, in addition to the non-physiological loading condition, there are also variations between the results of different studies (Pickering et al. [2021]).

### 1.4 Alternative approach to determining habitual strain states

Zumwalt et al. [2006] were the first to present a commercially available force plate for small animals, which presented advantages over previously described models (Heglund [1981], Full and Tu [1991], Rochester and Clarke [1994], Clarke and Still [1999], Ahn et al. [2004]). Because the force plate is not self-constructed, it proved to be more stable than predecessors, and in addition was able to report forces and moments multi-axially. This advance has enabled the recording of kinematic data from rodents, which are commonly used for motor nervous control experiments, addressing the high demand for methods to quantitatively assess the consequences of the changes made to the animals.

Building on these developments, Johnson et al. [2008] developed a musculoskeletal (MS) model of the rat hindlimb. Based on this, Charles et al. [2016] developed and published an openly available MS model of the mouse hindlimb, further enabling the study of mice. The idea for this study was to use the results of the MS model as an input for a subsequent Finite Element (FE) approach.

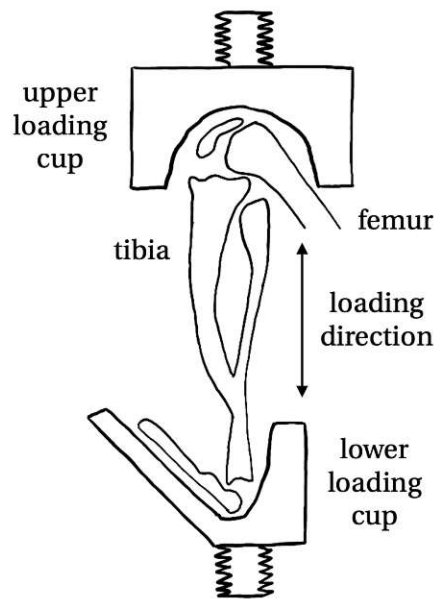


Figure 1.5: Schematic drawing of the tibial compression test - adapted from [De Souza et al. \[2005\]](#).

## 1.5 Description of used methodologies

### 1.5.1 Musculoskeletal modeling

In general, an MS model attempts to represent the body of a living being as closely as possible *in-silico*, with simplifications made to perform certain simulations that would be difficult or impossible to perform or measure in reality. Examples of simulated parameters are, e.g., muscle forces and forces acting in the joints during a certain movement.

Models typically consist of bodies, joints, forces, constraints and controllers. Bodies include 3D bone geometries, axes of rotation, and coordinates of bony landmarks. Joints specify the articulations between the bodies and also define joint centers, while muscles make up a large part of the forces in the model. These include not only muscle attachment points but also the mass, mechanical and inertial properties of each muscle. Other forces are, for example, ground reaction forces (GRFs) or other known external forces acting on the model. Finally, controllers determine the activation of the muscles ([Seth et al. \[2018\]](#)).

As input, MS models require exactly the data generated by the aforementioned advances: kinematic data and information on GRFs obtained from force plates. Electromyography (EMG) data, as an indicator of the activation of underlying muscles, also sometimes serve as an input, but was not used in this study.

### 1.5.2 Finite Element modeling

Finite Element approximations were first described by [Turner et al. \[1956\]](#), proposing the subdivision of the elastic continuum into elements of various shapes and sizes to answer questions about the behaviour of complex structures in response to external influences. This followed on developments of numerical methods to solve partial differential equations, such as by [Southwell \[1946\]](#), [Ritz \[1909\]](#) and [Galerkin \[1915\]](#), as nicely summarized by [Zienkiewicz \[2004\]](#). Ever since, advances in computer-aided calculations and simulations have led to the acceptance of the method also by the biomechanics community. It is used for various sub-areas inside biomechanics, such as for orthopedic or ventricular systems issues ([Erdemir et al. \[2012\]](#)), but also for the structural analysis of bones. In this particular case, displacements, stresses and strains in bone tissue can be assessed in a non-invasive manner, providing a basis for a wide variety of studies.

The creation of an FE model requires precise knowledge of the geometry and material properties of the body under investigation. In the case of bone, the first part of these properties can be

determined on a patient-specific basis using computed tomography (CT). The CT images are then converted into a 3D voxel model in a segmentation step. The elements of different shapes mentioned above are therefore hexahedral. The CT images can also be used to determine in which areas which material parameters are to be defined depending on the type of tissue found. These parameters determine the behavior of the model under load. In the case of the model used, a distinction was made between bone, growth plates and the area where the tibia and fibula meet.

In addition to the geometry, every FE analysis requires a set of load and boundary conditions that assign the external influences mentioned above to the model. In this case, these are the knee joint forces calculated with the MS model and a fixation of the bone at the distal end. This rough simplification is often sufficient to be able to make physiological statements about the behavior of the body, provided that the area of interest is far enough away from the points of force application point (St. Venant's principle). The final step is to determine and interpret the output.

## 1.6 Objective of this work

To the best of the authors' knowledge, there has been one study done by Prasad et al. [2010] that looked at strains in the murine tibia during normal locomotion and obtained loading conditions using an inverse dynamics approach. However, the MS model used for determining the resolved normal and shear forces differs considerably in complexity from the aforementioned mouse hindlimb model of Charles et al. [2016], as discussed in detail later. The model of Prasad et al. [2010], which was state-of-the-art for 2010, can be classified as outdated with today's possibilities of a much more accurate model thanks to higher computational power. It therefore makes sense to repeat and extend the process with a much more detailed model.

The goal of this study was to develop a comprehensive modeling pipeline for the assessment of stress and strain patterns in the mouse tibia during the stance phase. To achieve this goal, the aforementioned MS model was used to generate input data for the subsequently used FE model, as close as possible to the prevailing physiological conditions. After validating the results through comparison with pertinent data found in literature, the sensitivity of the FE model was explored based on variations of the input data, such as the underlying material properties.



Die approbierte gedruckte Originalversion dieser Diplomarbeit ist an der TU Wien Bibliothek verfügbar  
The approved original version of this thesis is available in print at TU Wien Bibliothek.

# Methods

## 2.1 Musculoskeletal modeling

The workflows used for this work are shown in Figure 2.1. Inputs to the sequence of analyses are framed in blue, code for analysis sections is framed in yellow, and intermediate or final results of sections are displayed without a frame.

Normally, inverse kinematics is run first to identify the set of generalized coordinates (joint angles and positions) that best match the recorded motion capture data. Since no such data was available, this step was skipped and the previously recorded kinematics were used as input data for the static optimization.

Inverse dynamics was run separately for validation purposes.

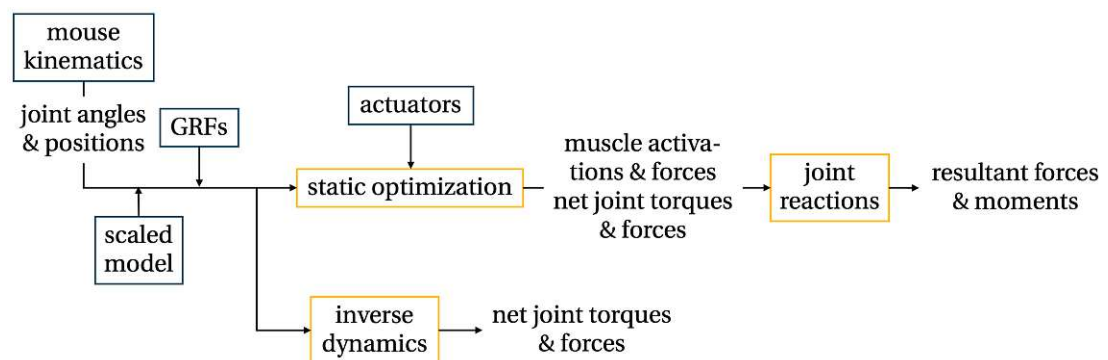


Figure 2.1: Workflows used for this work.

### 2.1.1 Mouse hindlimb models created by Charles et al. [2016]

The subject-specific MS mouse hindlimb models were developed by Charles et al. [2016] using the open-source software OpenSim. Two versions of the model were available to the author and are described below.

The 2018 model is available online and can be downloaded under <https://simtk.org/home/mousehindlimb>. It consists of four segments (pelvis, thigh, shank, toes) (see Figure 2.2) and can be used for simulation with the GRFs and kinematics provided by Charles et al. [2018]. The latter were filtered at 30 Hz during the analysis.

Since the model consists only of the right hindlimb, pelvis was fixed to the ground, prohibiting hip internal/external rotation, but allowing hip flexion/extension (F/E) and hip abduction/adduction (A/A).

The 2024 model was provided by James Charles upon request and is an improvement of the 2018 one, with the addition of the contralateral leg (see Figure 2.3) and an altered and filtered

## 2. Methods



Figure 2.2: Mouse hindlimb model version 2018, with and without muscles.

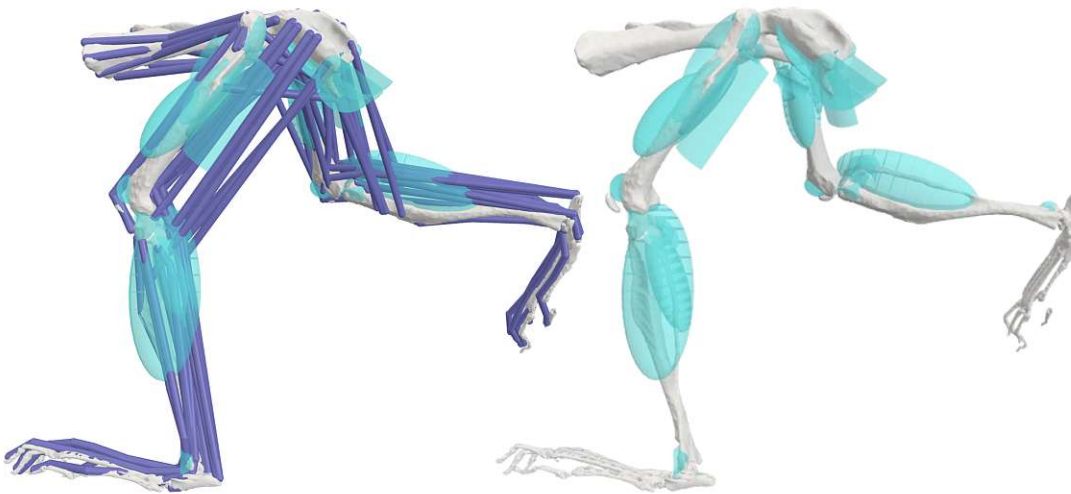


Figure 2.3: Mouse hindlimb model version 2024, with and without muscles. Wrapping surfaces are shown in turquoise.

version of the same kinematics (see Figure 2.4B), moving in space with possible flight phases (phases where both hindlimbs had no contact with the ground,  $GRF = 0$ , see Figure 2.5B). No information was recorded on the forelimbs, allowing no real distinction between true flight phases and "hopping" movement. It also includes wrapping surfaces over which the muscles wrap for a more physiological muscle pathway during the movement. In addition to the four segments mentioned above, the body 'toes' was split into two separate bodies with an additional joint in between, named 'foot' and 'toes'.

In both models, the hip joint was modeled as a ball-and-socket joint with three rotational degrees of freedom (DOFs): F/E, A/A and internal/external rotation. The knee joint as well as the metatarsal phalangeal joint (the latter only available in the 2024 version) were modeled as hinge joints with one DOF (F/E). The ankle joint in turn was again modeled with three rotational DOFs (F/E, A/A and inversion/eversion).

In total, Charles et al. [2016] installed 44 musculotendon units to actuate the models, using the generic Hill-type muscle model described by Millard et al. [2013]. Origins and insertion sites were determined by Charles et al. [2016] from reconstructed  $\mu$ CT scans.

### 2.1.2 Inverse dynamics analysis

Dynamics in general is the study of motion and the forces and moments that produce this motion (see Figure 2.6).

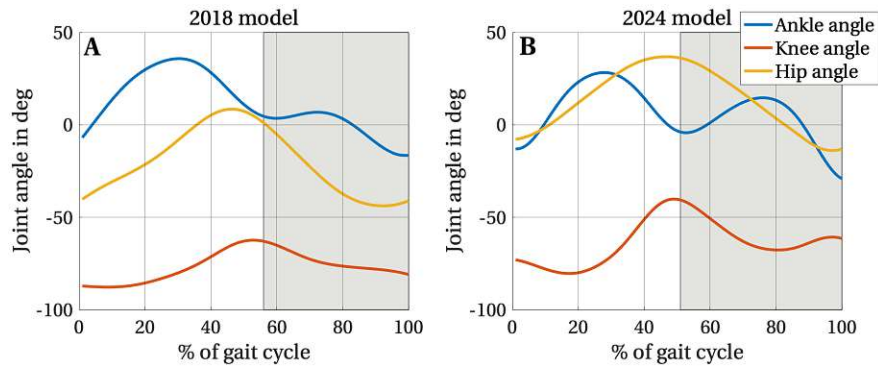


Figure 2.4: Kinematic input to the workflow provided by Charles et al. [2018]: A: Kinematics for the 2018 model, B: Kinematics for the 2024 model (just right leg shown).

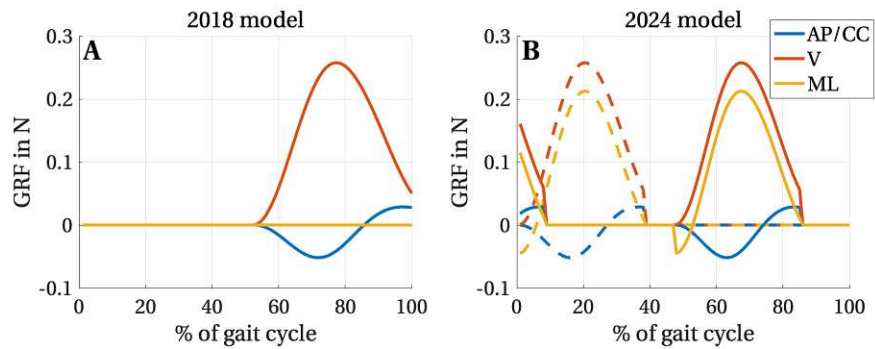


Figure 2.5: Ground reaction forces recorded by Charles et al. [2018] and used by the two models, in anteroposterior (AP)/cranially-caudally (CC), vertical (V) and mediolateral (ML) direction. Indicated in dashed lines are also the forces of the left leg in the 2024 model.

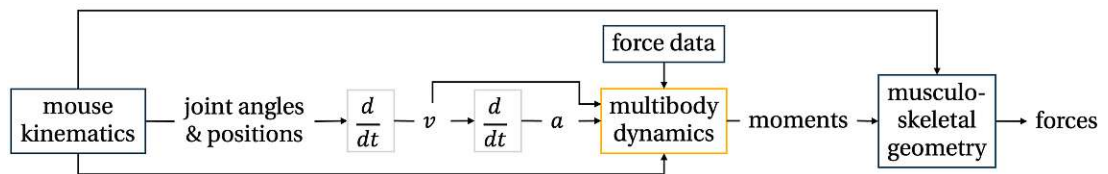


Figure 2.6: The inverse problem.

The inverse dynamics tool of OpenSim solves the classical equations of motion

$$M(q)\ddot{q} + C(q, \dot{q}) + G(q) = \tau, \quad (2.1)$$

where  $q$ ,  $\dot{q}$ ,  $\ddot{q}$  are the vectors of generalized positions, velocities and accelerations,  $M(q)$  is the system mass matrix,  $C(q, \dot{q})$  is the vector of Coriolis and centrifugal forces,  $G(q)$  is the vector of gravitational forces and  $\tau$  is the vector of the general forces (Sherman et al. [2011]).

Since all of the terms on the left-hand side of the equations are known from the experiment (recorded motion & GRFs), the generalized forces can be determined with the inverse dynamics tool. It propagates the equation through time with the use of numerical integrators, giving the trajectories of  $q$ ,  $\dot{q}$  and  $\ddot{q}$ . The results can then be used to estimate how the muscles of the model are activated to generate that motion (Delp et al. [2007]).

Inverse dynamics is also run during the static optimization analysis and therefore need not necessarily be run separately, but was implemented for reasons of workflow validation and comparison to what was published by Charles et al. [2018].

### 2.1.3 Static optimization analysis

The static optimization tool of OpenSim uses the assumptions on force distribution and the MS geometry to estimate the individual muscle forces that cause the model to accelerate. They are applied between the origin and insertion points of the muscles (Delp et al. [2007]).

Since there are more muscles in the model than DOFs to cover, a muscle force distribution problem arises. Theoretically, there are an infinite number of solutions available to achieve the desired motion with the number of muscles that could cause it. The algorithm attempts to determine the “best” set of muscle forces that produce the net joint moments at the discrete time steps, do not violate the defined force limits, and satisfy the optimization of the performance criterion. This performance criterion attempts to mimic the goal of the neural control system by focusing on minimizing the muscle forces required to achieve the desired movement (Crowninshield [1978]).

The equations of motion for the unknown generalized forces  $\tau$  mentioned above are solved subjected to the muscle activation-to-force condition

$$\sum_{m=1}^{n_m} [a_m f(F_m^0, l_m, v_m)] r_{m,j} = \tau_j \quad (2.2)$$

(constrained by force-length-velocity properties), while minimizing the objective function

$$J = \sum_{m=1}^{n_m} (a_m)^2, \quad (2.3)$$

where  $n_m$  is the number of muscles in the model,  $a_m$  is the activation level of the muscle  $m$ ,  $F_m^0$  is the maximum isometric force,  $l_m$  is the length,  $v_m$  is the shortening velocity,  $f$  is the force-length-velocity surface,  $r_{m,j}$  is the moment arm about the  $j^{th}$  joint axis, and  $\tau_j$  is the generalized force acting about the  $j^{th}$  joint axis (Crowninshield [1978]).

As indicated in Figure 2.1 residual and reserve actuators were included in the calculation of the static optimization to compensate for the assumptions met with the setup of the model. The reserve actuators were only used when the muscles of the model were unable to generate sufficient torque to fulfill the kinematic data, which was facilitated by a high cost function. The residual actuators, on the contrary, were not penalized by a cost function, as they mainly replace the missing diagonal front limbs and trunk (Charles et al. [2016]).

### 2.1.4 Joint reaction analysis

The joint reaction analysis tool calculates the forces and moments transferred across the joint surface, which are required to prevent the translation and rotation of the articulating surfaces of the joint relative to each other. The reported forces are the result of all acting forces in the model, including muscle forces, and represent the contributions of all un-modeled (soft-tissue) joint structures that cooperate to produce the recorded joint kinematics (Schutte et al. [1993]).

The loads are specific to the muscle force data and the joints of interest and can be reported for the bodies and coordinate reference frames of interest (see Figure 2.7).

### 2.1.5 Muscle force direction analysis

In order to extract accurate muscle attachment sites and vectors for the duration of the stance phase, the *Muscle Force Direction* plug-in (van Arkel et al. [2013], Phillips et al. [2015]) was added to the standard OpenSim set-up and run on OpenSim v4.1 (in contrast to v4.5 for the rest of the simulation). The analysis allows the distinction between anatomical and effective muscle attachments (see Figure 2.8), which for some muscles made a difference due to wrapping surfaces incorporated in the model lying in the muscles' paths.

The finally chosen attachment site type for each implemented muscle in the FE model can be seen in Table 2.1. The attachment point of M. biceps femoris posterior caudal (BFP caudal),

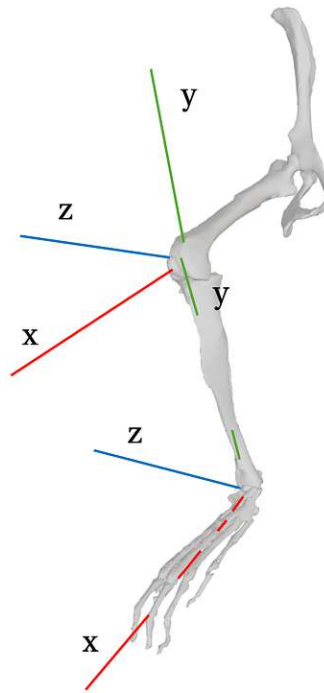


Figure 2.7: Coordinate reference frames, in which the results for the joint reaction analysis are given. Results for the knee joint are given in its child frame, results for the ankle joint in its parent frame to ensure applicability to the tibia.

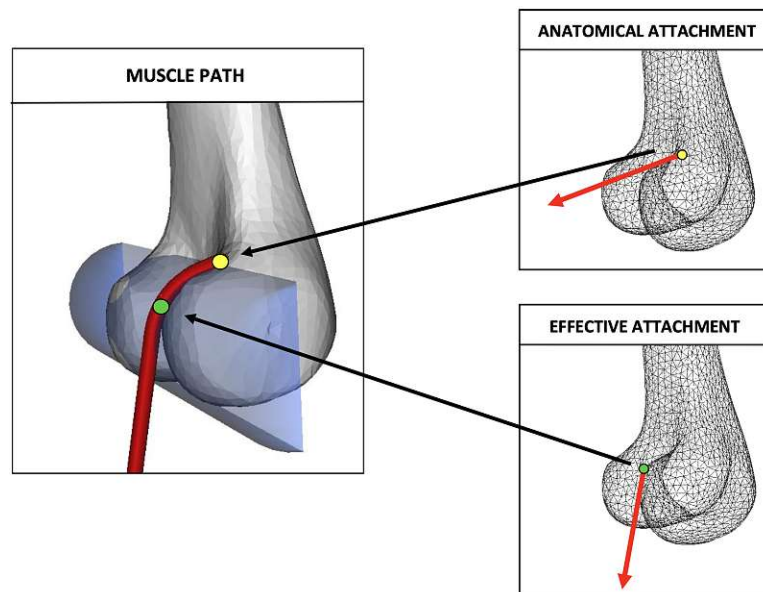


Figure 2.8: Difference between anatomical and effective attachment sites. Figure taken from the *Muscle Force Direction* plug-in user's guide, version 2020, downloadable in combination with the plug-in from [https://simtk.org/projects/force\\_direction](https://simtk.org/projects/force_direction).

defined in the MS model to attach on the interosseus membrane, was shifted to an area on fibula where the muscle spans over, resulting in a semi-effective attachment point. For the muscles M. rectus femoris (RF), M. vastus lateralis (VL), M. vastus medialis (VM) and M. vastus intermedius (VI), the effective attachment points were on the distal end of femur. Since the femoral bone is not part of the FE model (only tibia and fibula), anatomical attachment sites on the tibial surface were chosen for these muscles. M. tibialis posterior (TP) was therefore the only muscle implemented with effective attachment points, as all other implemented muscles' effective attachment points were also their anatomical. As the orientation of the force vectors also depends on the site of attachment, they were chosen to comply with the attachment type.

## 2. Methods

Muscle name	Attachment point modeling
SM	effective = anatomical
ST	effective = anatomical
BFP cranial	effective = anatomical
BFP mid	effective = anatomical
BFP caudal	adapted
RF	anatomical
VM	anatomical
VL	anatomical
VI	anatomical
SOL	effective = anatomical
TP	effective

Table 2.1: Attachment point modeling of included muscles in the model.

### 2.1.6 Utilization of results

In this work, joint reaction forces and moments for both knee and ankle joint as well as muscle forces are calculated for both models (2018 and 2024 version) to allow for a comparison between them.

However, only the results of the joint reaction analysis for the knee joint of the 2024 model and associated muscle forces are relevant for the subsequent steps. The 2018 model was validated by Charles et al. [2018] and works perfectly, but, as the 2024 model is more sophisticated and accurate, it was ultimately used to generate the input for the FE model.

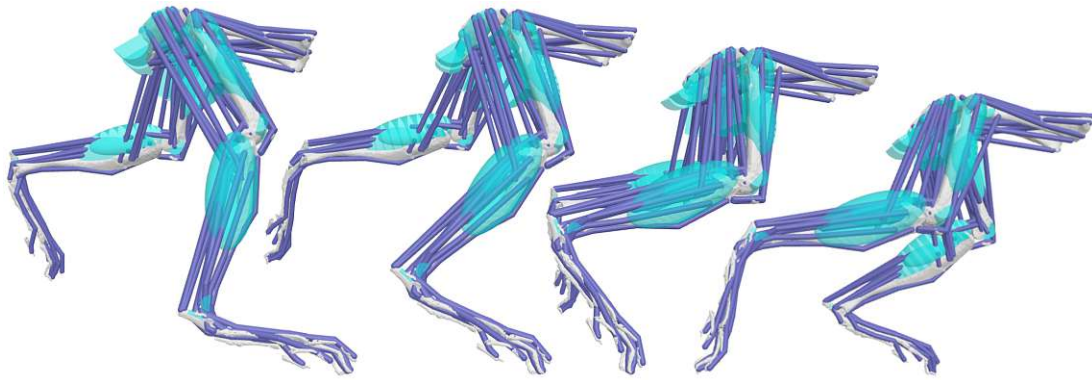
Furthermore, only muscles attaching to the proximal part of the tibia were included in the model (see Figure 2.12), as modeling of muscles attaching to the distal end is made redundant by the boundary conditions (see Chapter on FE modeling).

## 2.2 Data processing

The data were extracted from the models using the MATLAB code available online and further processed in MATLAB R2022b (Mathworks, Natick, MA), applying a linear interpolation to all results over the course of one gait cycle, also for reasons of comparability. From this point on, only the results for the right leg were used, as suggested by James Charles due to reliability reasons.

In order to obtain an overview of the mechanical load on the tibia during walking in mice, four time points were selected that divide the stance phase into three equal sections (see Figure 2.9). Data for these time points were extracted from the data set with a custom MATLAB script, before a rigid point transformation was applied to the results with the aim to register them to the FE model bone. The transformation matrix was determined using MATLAB's built-in *pcregistericp* algorithm (Besl and McKay [1992], Chen and Medioni [1992], Segal et al. [2009], Korn et al. [2014], Park et al. [2017]), for which the FE bone was registered (see Figure 2.10) to the mesh of the FE model (obtained from Pickering et al. [2021], see section below), which was exported from Abaqus and reduced in size and complexity using Meshlab (Cignoni et al. [2008]) first (see Figure 2.11).

The registering process was carried out in two steps: a first "initial guess" transformation chosen manually to pre-align the bones and, as a second step, the above described *pcregistericp* algorithm. The final transformation matrix' A entries (both matrices multiplied and used on the MS results) were:



$$\text{TP1: } t = t_{\text{stancebegin}} \quad \text{TP2: } t = \frac{1}{3} t_{\text{stanceend}} \quad \text{TP3: } t = \frac{2}{3} t_{\text{stanceend}} \quad \text{TP4: } t = t_{\text{stanceend}}$$

Figure 2.9: Time points 1-4 for which the results of the MS model served as an input for the FE model.

$$A = \begin{bmatrix} -0.9992 & -0.0341 & -0.0228 & -0.0002 \\ -0.0234 & 0.0184 & 0.9996 & -0.0004 \\ -0.0337 & 0.9992 & -0.0192 & 0.0325 \\ 0 & 0 & 0 & 1.0000 \end{bmatrix}.$$

Muscle attachment points of the MS model were also registered to the FE bone, with a final step of manually choosing points on the surface of the model closest to the registered point location to ensure connection to the surface using Meshlab's Pick Points tool.

## 2.3 Finite Element modeling

### 2.3.1 Description of model

This study used an already existing FE model previously employed to find an equivalent point load location representing the load on the tibial plateau applied by cups during the tibial compression test for the analysis of the diaphysis [Pickering et al. \[2021\]](#). It incorporates two different materials considered to exhibit linearly elastic behavior, bone ( $E = 17 \text{ GPa}$ ,  $\nu = 0.3$ ) and soft tissue ( $E = 10 \text{ MPa}$ ,  $\nu = 0.3$ ), to account for regions classified as growth plates as well as the tibiofibular interface. The voxel-based model was transferred from Ansys (Ansys Inc, Canonsburg, Pennsylvania) to Abaqus 2022 (Simulia (Dassault Systèmes), Vélizy-Villacoublay, France) and uses hexahedral, eight-node brick elements with reduced integration (C3D8R).

The most distal 10% of nodes were locked in all three translational directions, with rotations not being possible due to the element choice (see orange part in [Figure 2.12](#)). Forces were only applied on the proximal part of the tibia. On the one hand in the knee joint, which is located proximally slightly anterolaterally outside the bone, and on the other hand in the muscle attachment points on the bone surface.

For the application of forces and moments where the knee joint was defined in the MS model, a reference point was defined in the FE model. Subsequently, the approximate areas where the femoral condyles touch the tibial plateau (see [Figure 2.13](#)) were constrained to the movement of the reference point via two multi-point constraint orders type beam, the first connecting the reference point to a point located on the area, to which the whole area was then constrained to via the second multi-point constraint (for a schematic drawing, see [Figure 2.15](#)). Multi-point constraints type beam install rigid beams between nodes defined in primary and secondary node sets to constrain the displacement and rotation of the secondary node set ([Hibbitt \[1984\]](#)). The movement of the reference point, in which the forces and moments derived for the knee joint were applied, was not restricted.

All muscle forces were applied as concentrated forces to their respective attachment site node connected to neighboring nodes within a radius of approximately 0.07 mm via multi-point constraints to avoid stress concentration (see red dots on [Figure 2.12](#)).

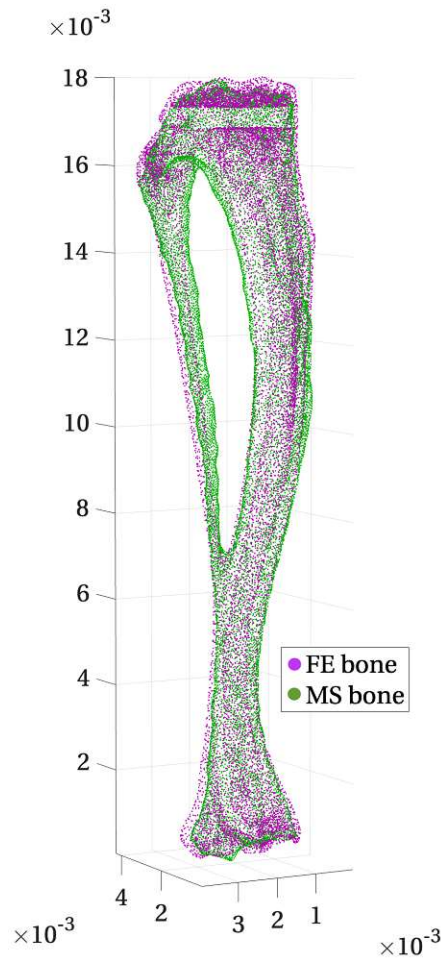


Figure 2.10: Result of the registering of bones on top of each other, in green: MS bone getting registered to the pink FE bone.

Applied force and moment values for the four time points can be viewed in the appendix (see Table [6.1](#) and [6.2](#)).

Results are mainly reported for the sections at 37% and 50% of the total length of the bone, viewed from the proximal end (see Figure [2.14](#)).

### 2.3.2 Variations of the model

The following studies were carried out to check influences of the studied parameters on the simulation results:

1. Variation of the elastic (tensile) modulus (from 17 GPa to 21 GPa)
2. Variation of the number of muscles included in the model (exclusion of M. semitendinosus; simulation including only the 5 main players)
3. Variation of the size of the force constraint area

The exclusion of M. semitendinosus was carried out to check for the influence a single muscle has on the local stress and strain profile despite the inclusion of multi-point constraints over the neighboring nodes to reduce stress concentration. The effect was evaluated at the site of attachment (approx. 30% section) and neighboring sites (25% and 35% sections).

To check for the influence of smaller muscles, a simulation was run using only muscles that at one point during the stance phase produced forces above 0.05 N. Those were M. biceps femoris posterior caudal, M. semimembranosus, M. rectus femoris, vastus medialis and M.

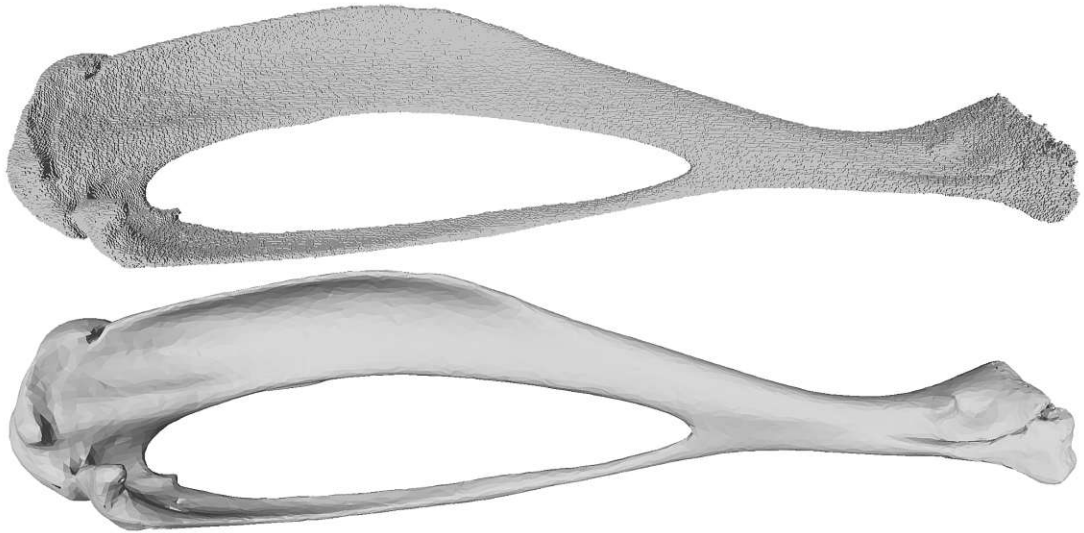


Figure 2.11: Comparison of meshes: Top: Mesh as exported from Abaqus, voxel-based. Bottom: Mesh after smoothing and simplification (reducing face count from 1,462,476 to 29,976)

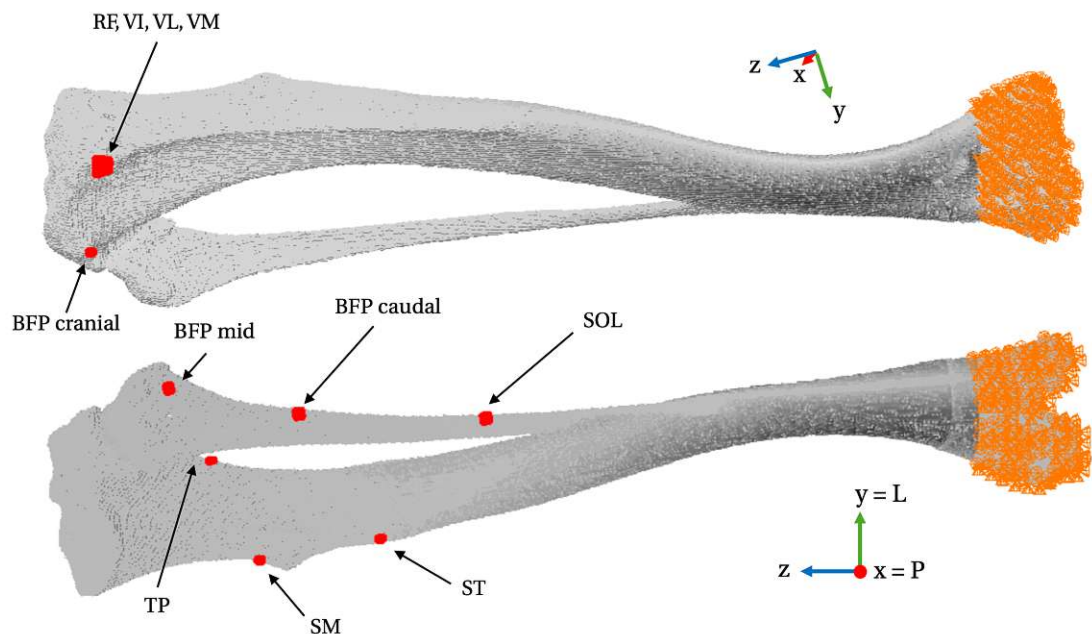


Figure 2.12: Voxel-based FE model used for the analysis. Indicated in orange are the most distal 10% of nodes which were fixed in all DOFs. Red spots are multi-point constraint areas for the respective muscle attachment points.

vastus lateralis. The effect was evaluated at the sections of interest (37% and 50%) and at sections 20%, 25%, 30%, 35% and 40% viewed proximally.

Lastly, the influence of the size of the area, of which the nodes were restricted to the movement of a single node located on the tibial plateau, which in turn was restricted to the node where the knee joint reaction forces and moments were applied to, was determined. This can be imagined like sketched in Figure 2.15. The area, colored in red in the schematic drawing, was reduced in size to the one shown in Figure 2.13 as can be seen in Figure 2.16. The effect was again evaluated at the sections of interest (37% and 50%).

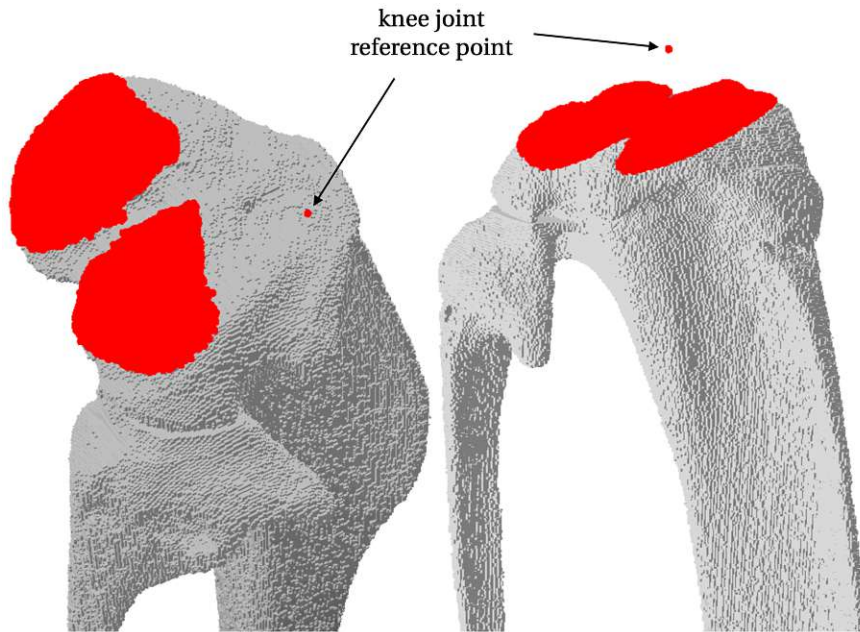


Figure 2.13: Location of knee joint reference point and multi-point constrained area on the tibial plateau.

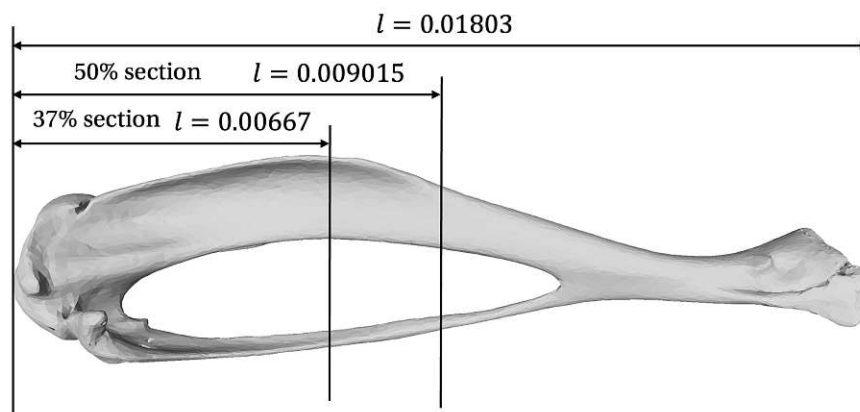


Figure 2.14: Illustration of the locations of the sections of interest.

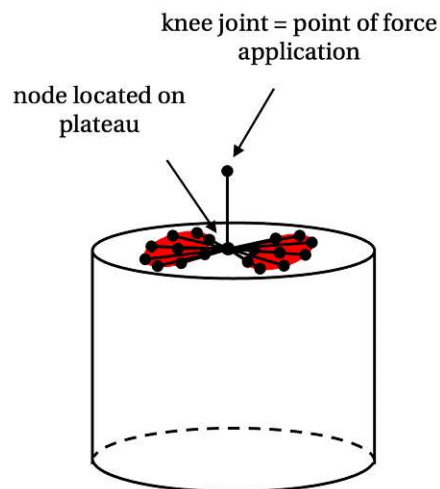


Figure 2.15: Schematic drawing of the constraints used in the application of the knee joint reaction forces and moments.

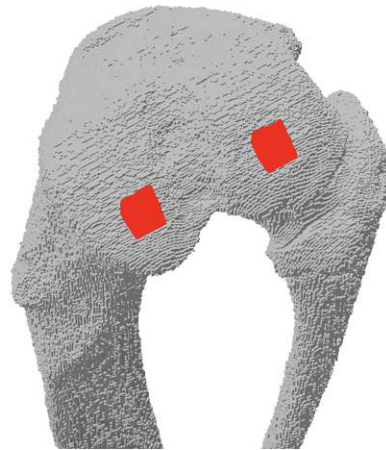


Figure 2.16: Location and size of smaller multi-point constrained area on the tibial plateau tested.



# Results

## 3.1 Musculoskeletal model

### 3.1.1 Muscle and joint reaction forces based on original model (2018 version)

#### Static optimization results - muscle forces

Muscle forces computed by the static optimization algorithm over the gait cycle for the 2018 model are reported in Figure 3.1

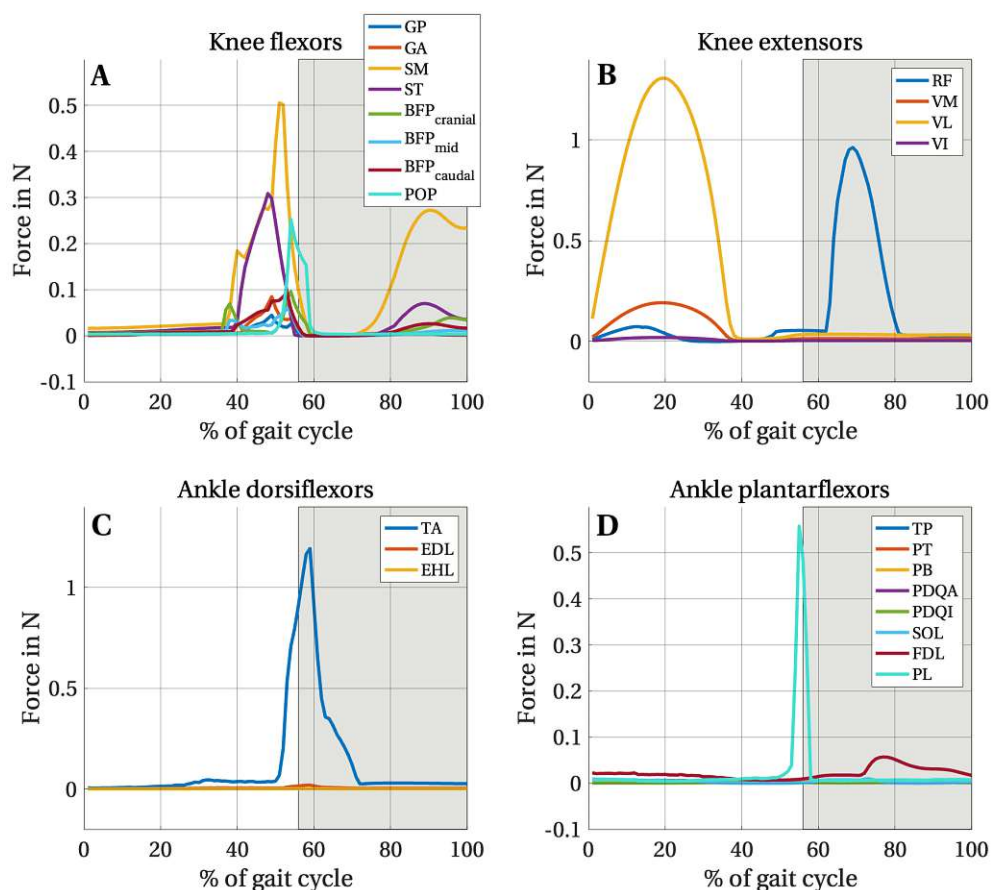


Figure 3.1: Muscle forces of the 2018 model. Muscles are grouped after their function, A: knee flexors, B: knee extensors, C: ankle dorsiflexors, D: ankle plantarflexors.

Of the muscles in Figure 3.1A, the M. semimembranosus (SM) & M. semitendinosus (ST), both originating from the pelvis, show the highest forces of the knee flexor muscles, namely 0.506

### 3. Results

N and 0.309 N, respectively. Also worth mentioning is the M. popliteus (POP), which rises to 0.252 N at the beginning of the stance phase.

The further course of SM cannot be explained physiologically, which is one of the reasons why the 2024 model was preferred subsequently.

Knee extension during the swing phase is mainly facilitated by M. vastus lateralis (VL, maximum value: 1.306 N) in the model, while M. rectus femoris (RF) dominates during the stance phase (maximum value: 0.951 N, see Figure 3.1B).

Regarding the ankle dorsiflexors, mainly M. tibialis anterior (TA) is causing the movement (maximum value: 1.454 N, see Figure 3.1C).

Ankle plantarflexion is mainly caused by M. peroneus longus (PL) at first ground contact, while push-off is mediated through M. flexor digitorum longus (FDL), with maximum values of 0.558 N and 0.057 N, respectively (see Figure 3.1D).

#### Joint reaction results knee joint

The highest compression forces in the knee joint during stance phase arise along the y-direction (pointing proximally), amounting to -12.81 times body weight (xBW) at ground contact. The forces then fall back approximately to the level they were at before ground contact. Forces in x-direction (pointing cranially) are higher during swing phase (maximum value: 6.616 xBW) than during stance phase (maximum value: -3.23 xBW). Forces in z-direction (pointing laterally) are in comparison to the forces into the other directions small, peaking at ground contact with a maximum value of -1.1997 xBW (see Figure 3.2A).

Almost no moment was calculated around the z-axis except for a sharp peak at the transition from swing to stance phase (maximum value: -0.814 Nmm). Around the x-axis, a rise in the calculated moment occurs at ground contact (maximum value: 1.525 Nmm), lasting for half of the stance phase, before dropping below zero for the rest of the stance phase. The moment around the y-axis is positive during the swing phase (maximum value: 0.515 Nmm) before dropping to negative values, peaking at the transition between swing and stance phase (-0.992 Nmm), and remaining in the negative sector for the rest of the stance phase (see Figure 3.2B).

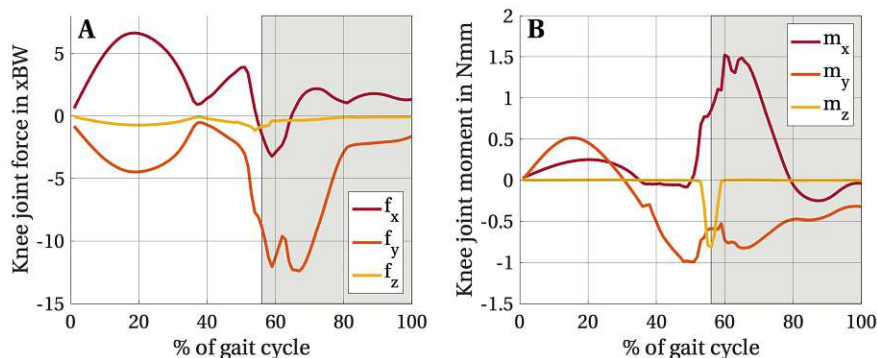


Figure 3.2: Forces (A) and moments (B) prevailing in the knee joint of the 2018 model during the gait cycle, calculated by the joint reaction analysis tool.

#### Joint reaction results ankle joint

Forces in the ankle joint are all characterized by sharp peaks at the transitions from swing to stance phase.

The peak of forces into x-direction peaks at 2.675 xBW. Highest are the forces in y-direction, amounting to -17.674 xBW, while forces in z-direction only rise to -2.526 xBW (see Figure 3.3A).

The moments of the ankle joint all first rise to positive values (with 1.112 Nmm, 0.378 Nmm and 3.485 Nmm as maximum values for  $M_x$ ,  $M_y$ , and  $M_z$ , respectively), before falling to negative values in y- and z-direction (-0.246 Nmm and -2.533 Nmm) (see Figure 3.3B).

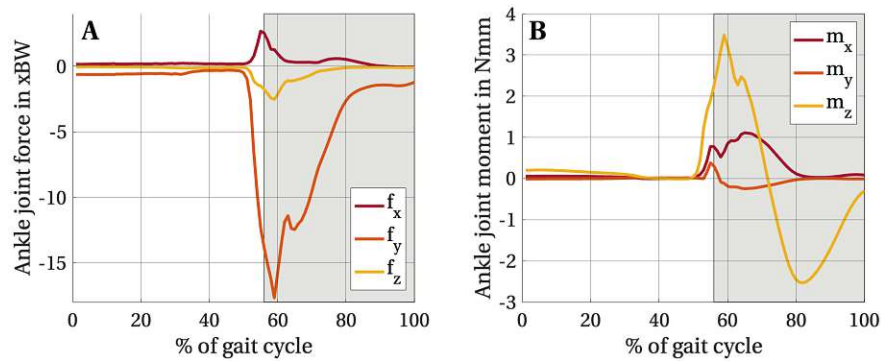


Figure 3.3: Forces (A) and moments (B) prevailing in the ankle joint of the 2018 model during the gait cycle.

### 3.1.2 Muscle and joint reaction forces based on updated model (2024 version)

#### Static optimization results - muscle forces

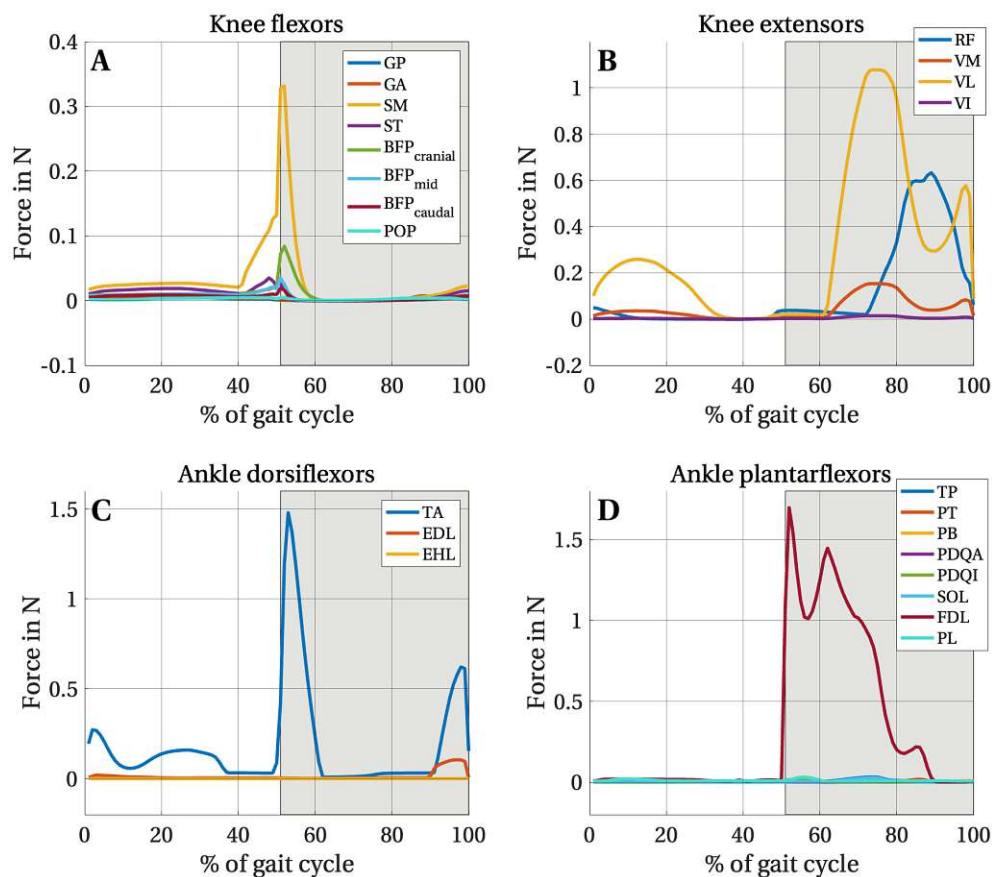


Figure 3.4: Muscle forces of the 2024 model. Muscles are grouped after their function, A: knee flexors, B: knee extensors, C: ankle dorsiflexors, D: ankle plantarflexors.

Similar to the results of the 2018 model, *M. semimembranosus* (SM) dominates of the knee flexor muscles (maximum value: 0.314 N). *Musculus biceps femoris posterior* (BFP) cranial follows second with a maximum at 0.082 N (see Figure 3.4A).

With the knee extensors, it is again the *M. tibialis anterior* (TA) that governs the movement with a maximum value of 1.454 N at first ground contact and 0.639 N at push-off. *Musculus extensor digitorum longus* (EDL) also contributes with 0.104 N (see Figure 3.4B).

Ankle dorsiflexion during the swing phase is again facilitated by *M. vastus lateralis* (VL, maxi-

### 3. Results

imum value: 0.258 N) in the model, now also dominating during the stance phase (first peak maximum value: 1.078 N), while M. rectus femoris (RF) rises just to 0.632 N (see Figure 3.4C).

In contrast to the 2018 model, ankle plantarflexion is now mainly caused by M. flexor digitorum longus (FDL) during most of the stance phase with a maximum value of 1.687 N right after ground contact (see Figure 3.4D).

#### Joint reaction results knee joint

In comparison to the 2018 model, the highest compression forces in the knee joint during the stance phase still arise along the y-direction, but on a smaller scale, getting to -6.585 xBW at initial ground contact and staying above the initial level for the duration of the stance phase. Same holds true for the forces in z-direction, rising to -2.82 xBW at the middle of the stance phase. Forces into the x-direction are rising to positive values after an initial dip to negative values, peaking at 6.353 xBW at the middle of the stance phase (see Figure 3.5A).

The moment around the x-axis first peaks to a negative value of -2.308 Nmm before rising to 6.230 Nmm during the middle of the stance phase. With a similar shape, but smaller values, the moment around the y-axis stays nearly 0 for all of the swing phase before rising to 2.534 Nmm. The moment around the z-axis is substantively smaller, with positive values during the swing phase (maximum value: 0.290 Nmm), one negative peak at the transition between swing to stance phase (maximum value: -0.389 Nmm) and a rise back to positive values for the rest of the stance phase (see Figure 3.5B).

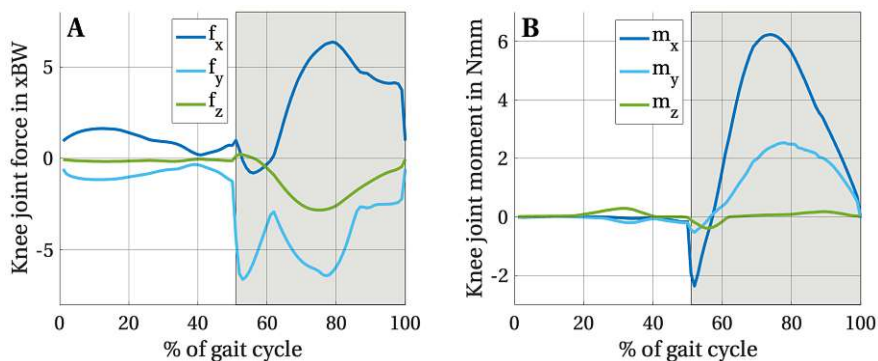


Figure 3.5: Forces (A) and moments (B) prevailing in the knee joint of the 2024 model during the gait cycle.

#### Joint reaction results ankle joint

The forces in the ankle joint are all close to 0 xBW during the swing phase, only rising after initial ground contact. As in the 2018 model, the forces are highest in y-direction, although seemingly mirrored along the x-axis of the plot: while negative in the 2018 model, the forces in the 2024 along the y-direction rise to 16.396 xBW. Second largest are the forces along the x-direction, rising to -8.584 xBW and falling slowly back to 0 xBW over the course of the stance phase. Forces along the x-direction, in contrast to the other two arising forces, do not peak at the initial ground contact but only peak at the middle of the stance phase with a maximum value of 1.789 xBW (see Figure 3.6A).

The moments of the ankle joint are again close to 0 Nmm for most of the swing phase. The moment around the x-axis first falls to -0.922 Nmm before rising to 1.393 Nmm during large parts of the stance phase, before falling back down to 0 Nmm at the end of the stance phase. The moment around the y-axis rises shortly before plummeting down to -2.329 Nmm, reaching its minimum at the middle of the stance phase, before rising up again to baseline. The moment around the z-axis is - compared to the other moments of the ankle joint in the 2024 model - rather small, with a peak in the second half of the stance phase, reaching a value of 0.386 Nmm (see Figure 3.6B).

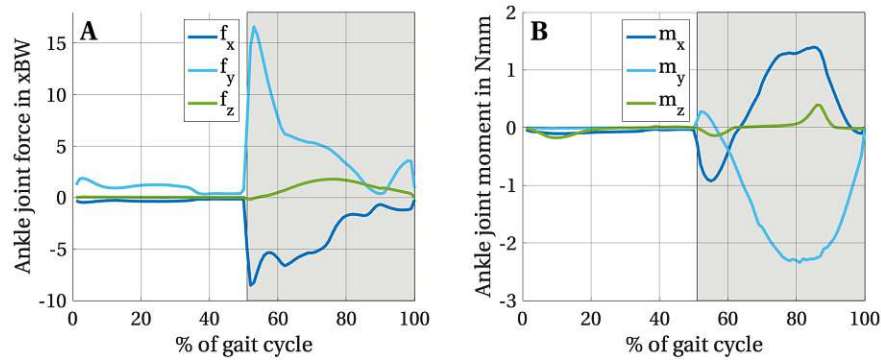


Figure 3.6: Forces (A) and moments (B) prevailing in the ankle joint of the 2024 model during the gait cycle.

## 3.2 Finite Element model

### 3.2.1 Results for $E = 17$ GPa

#### Stress results for all time points

Maximum tensile stresses along the longitudinal axis (S33) at the 37% section arise at time point (TP) 2 with 87.11 MPa at the lateroposterior part, while maximum compressive stresses along the longitudinal axis at the 37% section amount to -86.09 MPa at the medial side at TP3. In TP4, the area where the largest tensile stresses are present shifts from the lateroposterior part to a larger region along the lateral side, leading up to the anterior edge. Maximum values of stresses into the lateral and posterior direction are significantly lower for all four TPs and less spacially allocatable, with a maximum tensile stress along the laterally pointing axis (S22) of 10.37 MPa arising in TP3, and a maximum compressive stress along the same axis of -18.69 MPa in TP2. Maximum values along the posteriorly pointing axis (S11) amount to 11.53 MPa for tensile (TP2) and -13.21 MPa for compressive (TP3) stresses at the 37% section (see Figure 3.7).

For the 50% section, both tensile and compressive maximum stresses along the longitudinal axis are calculated for TP3 with 123.5 MPa at the lateral and -127.4 MPa at the medial side, respectively. The same holds true for the two other axes, where maximum values are calculated for TP3. The maximum tensile stress along the laterally pointing axis is calculated to 18.48 MPa, compressive stress reach values of -20.70 MPa at its maximum. For the axis pointing posteriorly, maximum stresses rise to 20.70 MPa and -17.98 MPa (see Figure 3.8).

While the neutral lines of TP1-TP3 seem to stay approximately constant at the same position, the axis starts to rotate between TP3 and TP4, resulting in an anti-clockwise rotated position in TP4.

#### Shear stress results for all time points

Maximum shear stresses for the 37% section arise along the longitudinal axis in lateral direction for TPs 2 and 3 with maximum values of 18.51 MPa and -14.71 MPa, respectively. Shear stresses along the axis pointing posteriorly in lateral direction are smallest for all four time points (see Figure 3.9).

For the 50% section, shear stresses along the axis pointing posteriorly in lateral direction only reach larger values confined to small areas, remaining in a range of -0.9765 MPa to 1.836 MPa

### 3. Results

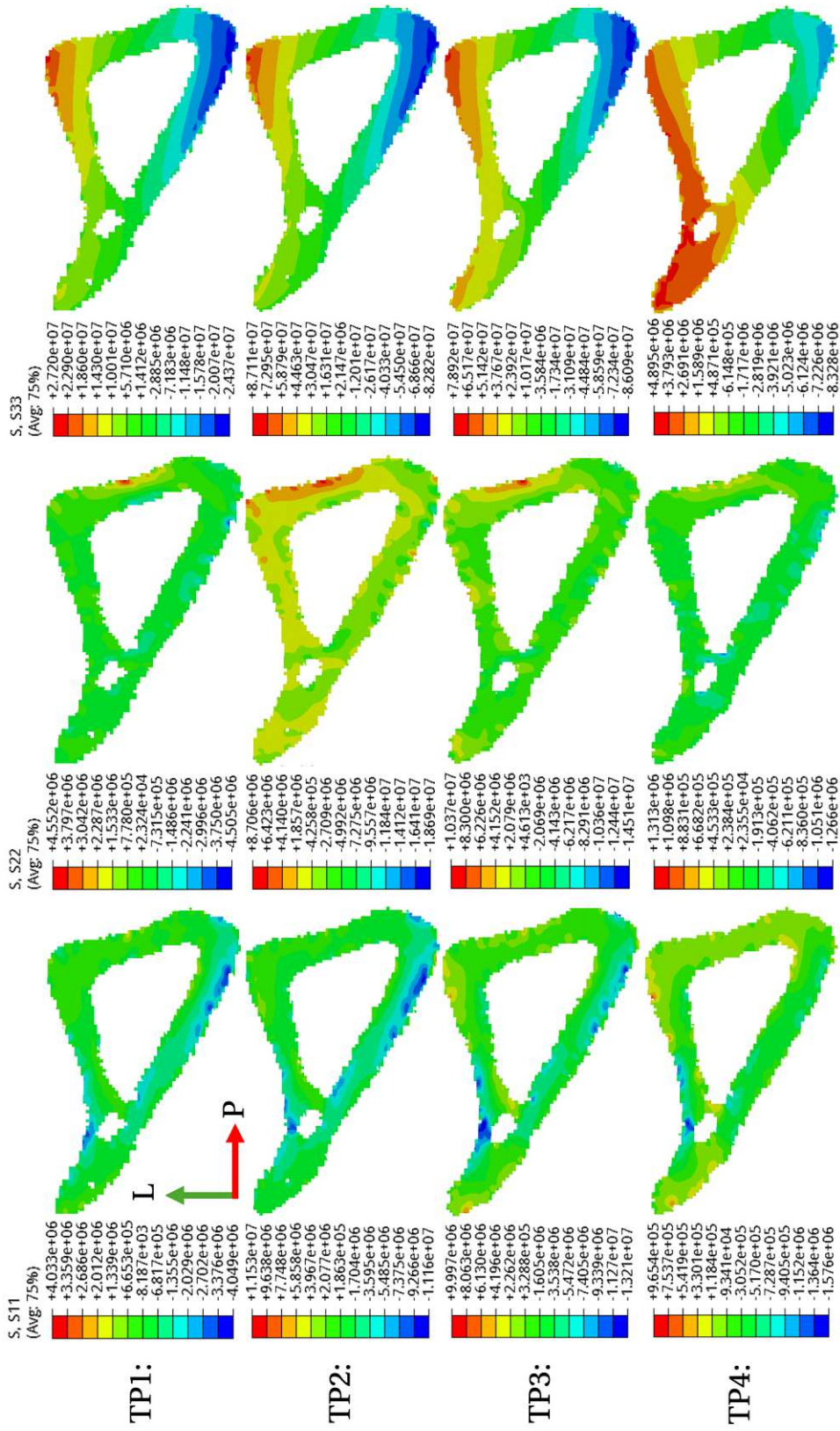


Figure 3.7: Stress results for the 37% section,  $E = 17 \text{ GPa}$ . Time points 1 to 4 are displayed top to bottom, stresses in the direction of the main axes are displayed from left to right in ascending order.

for the majority of the area of the 50% section. For the other two shear stress components of the stress tensor, profiles are more distinctly graded. Shear stresses along the axis pointing posteriorly in longitudinal direction are smallest at the anterior side with a minimum value of -25.5 MPa for TP3, and largest at the lateral side with a maximum of 24.36 MPa (also TP3). The largest shear stresses, although, are computed for the longitudinal axis in lateral direction for TP3 with maximum values of 32.12 MPa and -29.46 MPa for the 50% section (see Figure 3.10).

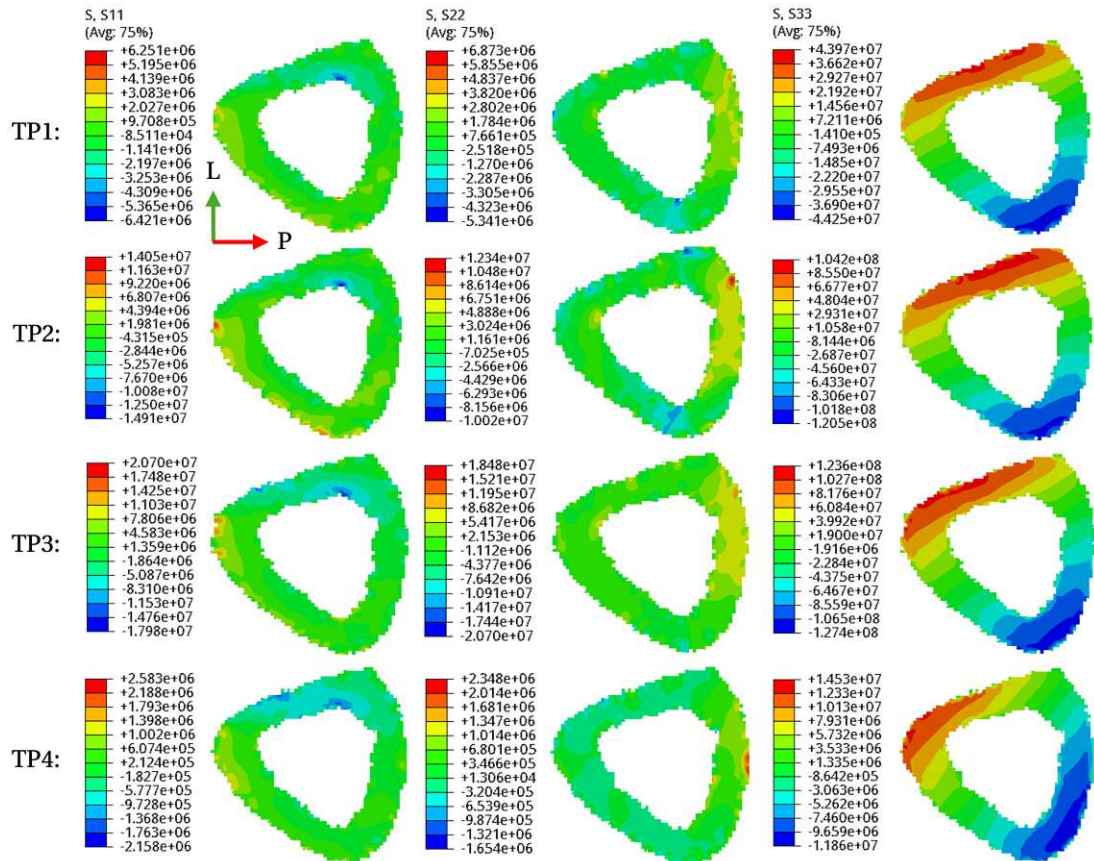


Figure 3.8: Stress results for the 50% section,  $E = 17$  GPa. Time points 1 to 4 are displayed top to bottom, strains in the direction of the main axes are displayed from left to right in ascending order.

### Strain results for all time points

Maximum strains are again calculated in longitudinal direction, with strains in the lateral and posterior direction following with a small gap. Maximum tensile strains are computed for the lateral side of the 37% section, amounting to  $5086 \mu\epsilon$  in TP2, while maximum compressive strains arise at the medial side of the 37% section in TP3 with a value of  $-4937 \mu\epsilon$ . In contrast to the locations of tensile and compressive strains in the longitudinal direction, strain profiles are exactly opposite for strains into the posterior and lateral direction (see Figure 3.11).

The same inversion of strain distribution is repeated for the 50% sections, where maximum tensile strains arise for the longitudinal direction at TP3 with  $7302 \mu\epsilon$  at the lateral side, while for the posterior and lateral directions, tensile strains are largest at the medial side. Maximum compressive strain is calculated for TP3 with a value of  $-7424 \mu\epsilon$  (see Figure 3.12).

### Bending and torsional moments for all time points

Comparing the two sections of interest, higher torsional moments occur in the 37% section, with a maximum torsional moment of  $0.001672$  Nm at TP3. Regarding the bending moment in the x-direction, it can be summarized that higher values are calculated for the 50% section, with a maximum of  $0.01307$  Nm at TP2. Bending moments in the y-direction remain lower

### 3. Results

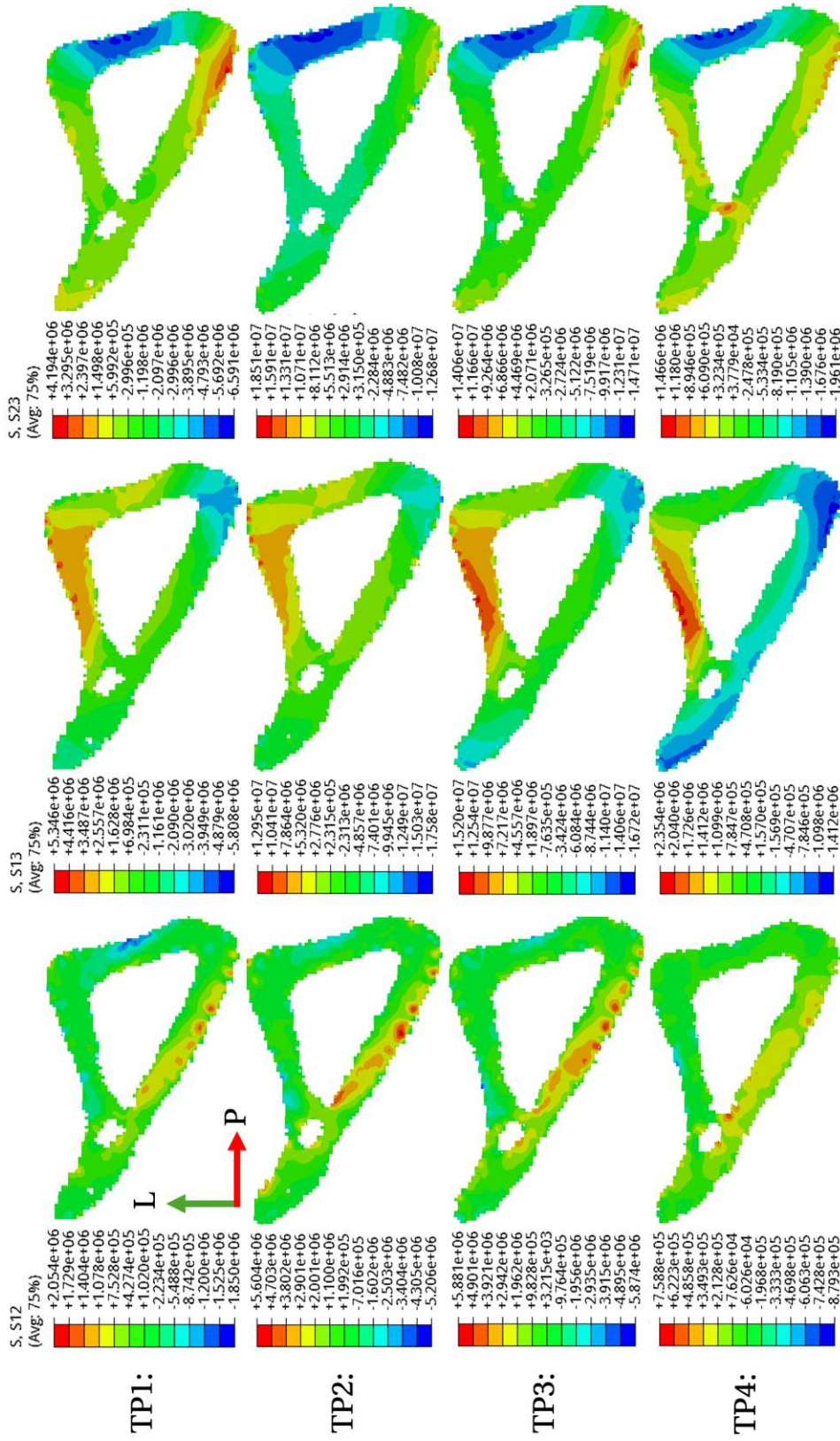


Figure 3.9: Shear stress results for the 37% section,  $E = 17 \text{ GPa}$ . Time points 1 to 4 are displayed top to bottom, shear stresses are displayed from left to right in ascending order.

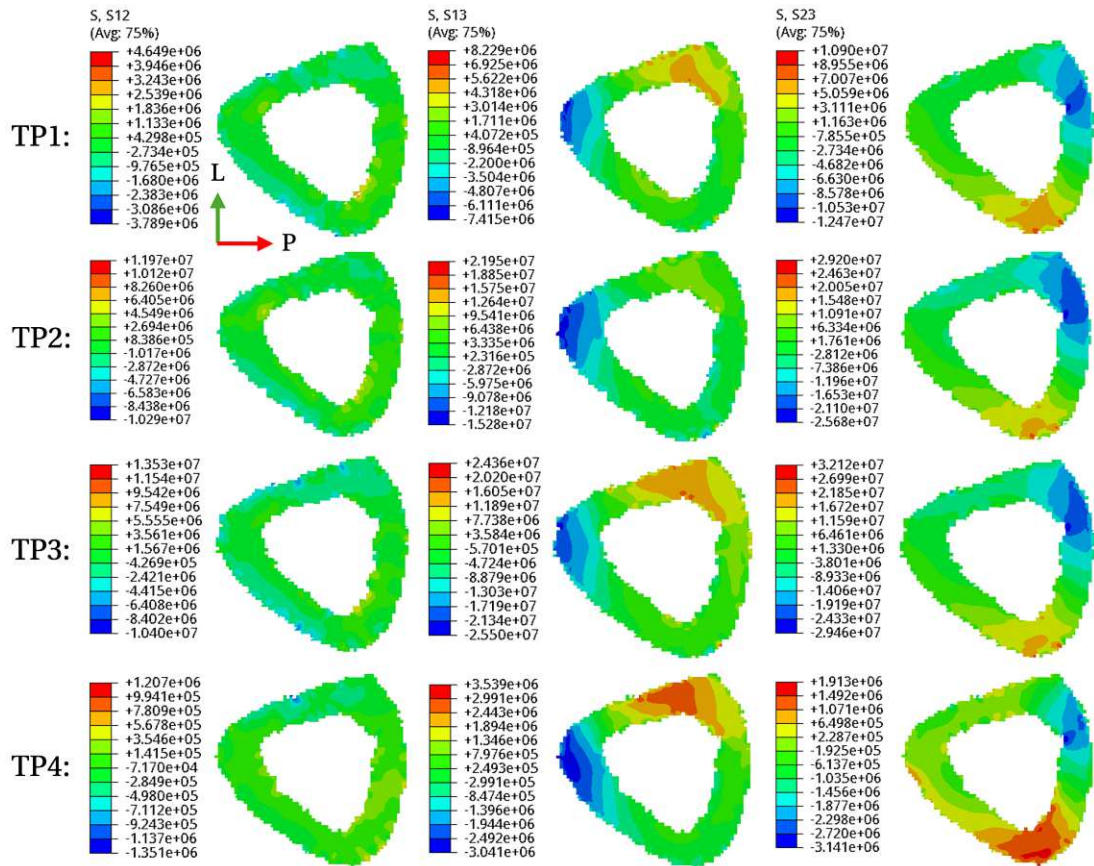


Figure 3.10: Shear stress results for the 50% section, E = 17 GPa. Time points 1 to 4 are displayed top to bottom, shear stresses are displayed from left to right in ascending order.

	TP1	TP2	TP3	TP4
<b>37% section</b>				
Torsional moment $M_T$ [Nm]	0.000576	0.001042	0.001672	0.0002868
Bending moment $M_x$ [Nm]	0.00334	0.01109	0.01087	0.0006931
Bending moment $M_y$ [Nm]	0.001613	0.004679	0.008744	0.001125
<b>50% section</b>				
Torsional moment $M_T$ [Nm]	0.0004131	0.0008601	0.001461	0.0002526
Bending moment $M_x$ [Nm]	0.004864	0.01307	0.01257	0.0008661
Bending moment $M_y$ [Nm]	0.002702	0.005631	0.01070	0.001

Table 3.1: Bending and torsional moments for all time points, E = 17 GPa.

in magnitude than those in the x-direction, but are also higher in the 50% section, with a maximum value of 0.0107 Nm at TP3 (see Table 3.1 and Figure 3.13).

### 3.2.2 Results for E = 21 GPa

#### Stress results for all time points

A change in the elastic (tensile) modulus to 21 GPa results in higher values for tensile and compressive stresses along the longitudinal axis at the 37% section with 87.19 MPa (TP2) and -86.71 MPa (TP3), respectively. A different trend is observed for stresses along the other axes, with maximum stresses along the axis pointing laterally rising to 12.43 MPa (TP3), surmounting

### 3. Results

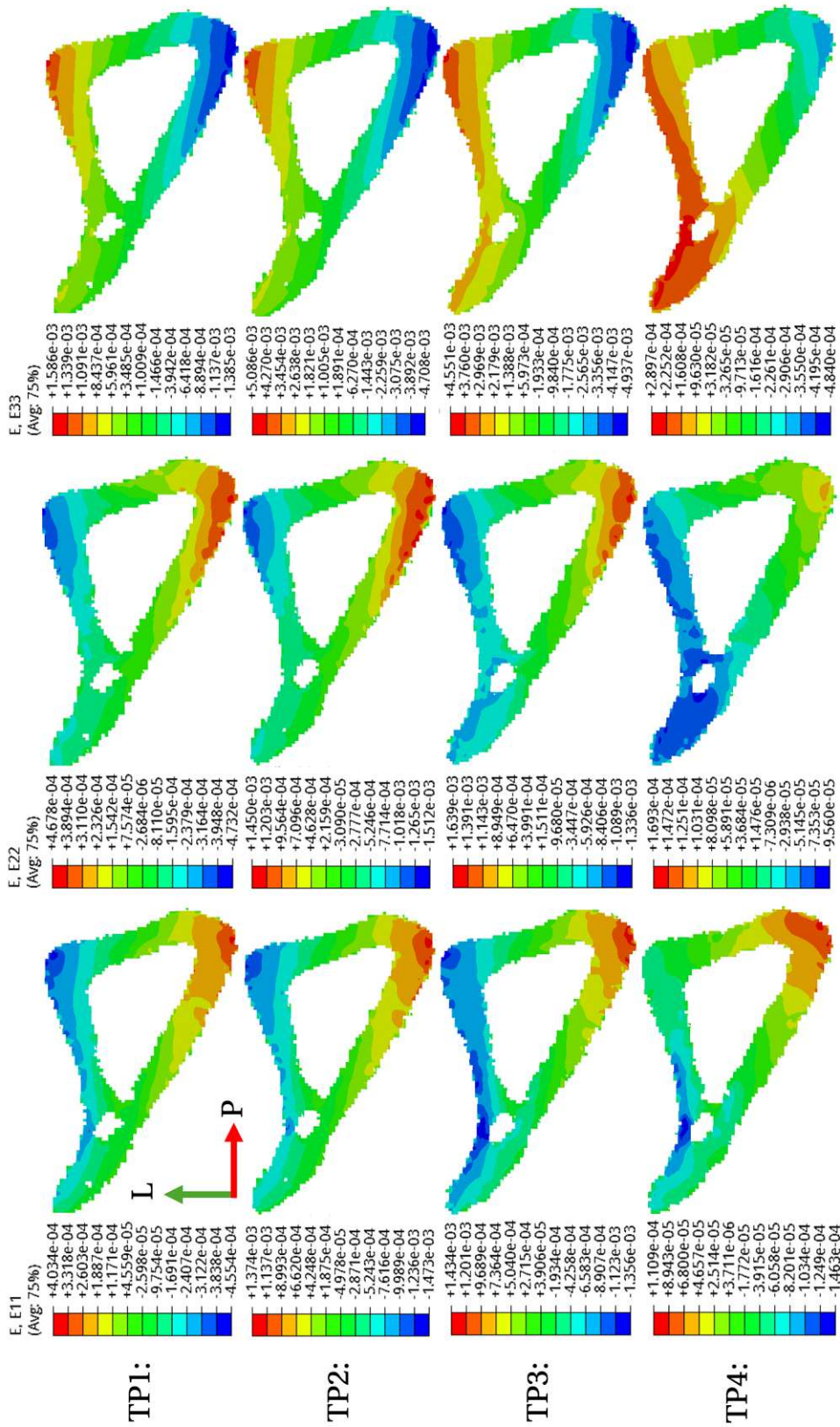


Figure 3.11: Strain results for the 37% section,  $E = 17 \text{ GPa}$ . Time points 1 to 4 are displayed top to bottom, strains in the direction of the main axes are displayed from left to right in ascending order.

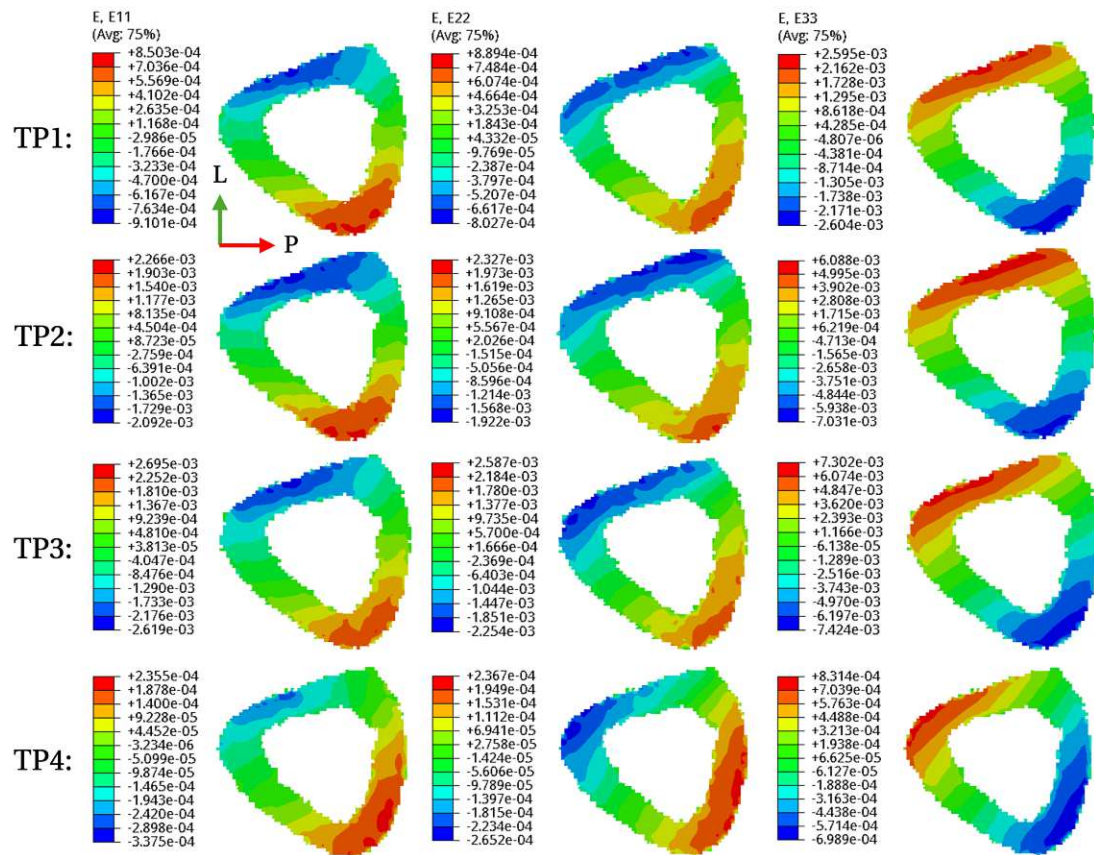


Figure 3.12: Strain results for the 50% section, E = 17 GPa. Time points 1 to 4 are displayed top to bottom, strains in the direction of the main axes are displayed from left to right in ascending order.

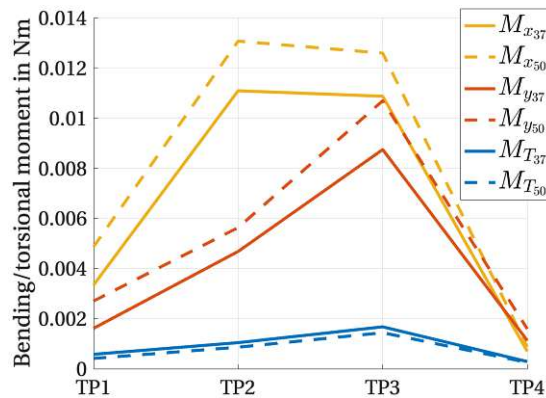


Figure 3.13: Graphical representation of Table 3.1

### 3. Results

the value of the stress along that axis under the 17 GPa condition, and -13.58 MPa (TP2), which is lower than in the 17 GPa simulation. Maximum tensile and compressive stresses along the axis pointing posteriorly reach values of 9.995 GPa (lower than in the 17 GPa simulation) and -13.22 GPa (nearly constant with regard to the 17 GPa simulation) (both TP3), respectively (see Figure 3.14).

As at the 37% section, a change in the elastic (tensile) modulus to 21 GPa results in slightly higher tensile maximum stresses along the longitudinal axis for the 50% section, with 123.6 MPa. Maximum compressive stresses remain unchanged along the longitudinal axis with a value of -127.4 MPa. Regarding the axis pointing laterally, maximum tensile and compressive stresses are present at TP3 with 18.48 MPa and -20.70 MPa and therefore also did not change as compared to the 17 GPa simulation. Stresses in the direction of the axis pointing posteriorly are calculated to 20.71 MPa and -17.98 MPa and by this only changed minimally with respect to the 17 GPa simulation (see Figure 3.15).

#### Shear stress results for all time points

For the 37% section, maximum shear forces are again observed along the longitudinal axis in lateral direction for TP3 with maximum values of 15.10 MPa and -14.71 MPa, where tensile shear stresses decreased with regard to the 17 GPa simulation, and compressive shear stresses remain the same. Compressive shear stresses in general occur for most TPs and directions at the posterior side of the bone. A strong exception from this rule is the shear stress along the axis pointing posteriorly in longitudinal direction in TP4, where compressive shear stresses were located on the medial side leading up to the anterior edge. Tensile shear stresses along the axis pointing posteriorly in lateral direction and along the longitudinal axis pointing laterally are located on the medial side, while tensile shear stresses along the axis pointing posteriorly in longitudinal direction are located on the lateral side (see Figure 3.16).

Regarding the 50% section, the same shear stress profiles are observed regarding shear stresses along the axis pointing posteriorly in lateral direction. Highest shear stresses arise along the longitudinal axis in lateral direction with values of 32.12 MPa and -29.46 MPa for TP3, showing no change to the 17 GPa simulation (see Figure 3.17).

#### Strain results for all time points

In comparison to the 17 GPa simulation, maximum tensile strains with an elastic (tensile) modulus of 21 GPa amount to 4121  $\mu\epsilon$  in TP2 for the 37% section, while maximum compressive strains arise in TP3 with a value of -4092  $\mu\epsilon$ , which implies a non-neglectable reduction by 18.99% and 17.12%, respectively.

For the 50% sections, maximum strains arise at TP3 along the longitudinal axis with 5911  $\mu\epsilon$  at the lateral side and -6011  $\mu\epsilon$  at the medial side, signifying an even greater reduction by 19.05% and 19.03%, respectively.

The maximum values of the FE simulations for 17 GPa and 21 GPa are also shown in Table 3.2. Indicated in bold are values that are greater in the 21 GPa simulation compared to the 17 GPa simulation.

#### 3.2.3 Results for different amounts of muscles included

##### Exclusion of *M. semitendinosus*

Musculus semitendinosus (ST) attaches to the medial side of the bone (see Figure 3.20) close to the sections of interest with a maximum force of 0.025 N (TP1). Comparing the results of the simulation where ST was included to one run without ST, the existence of ST was found to increase compressive stress values along the longitudinal axis by 0.78% at the section of attachment (approx. 30% section) and decrease tensile stresses by 0.25%. Regarding strains, the inclusion of ST resulted in an increase in maximum tensile strains by 0.30% and a decrease in maximum compressive strains by 0.28%.

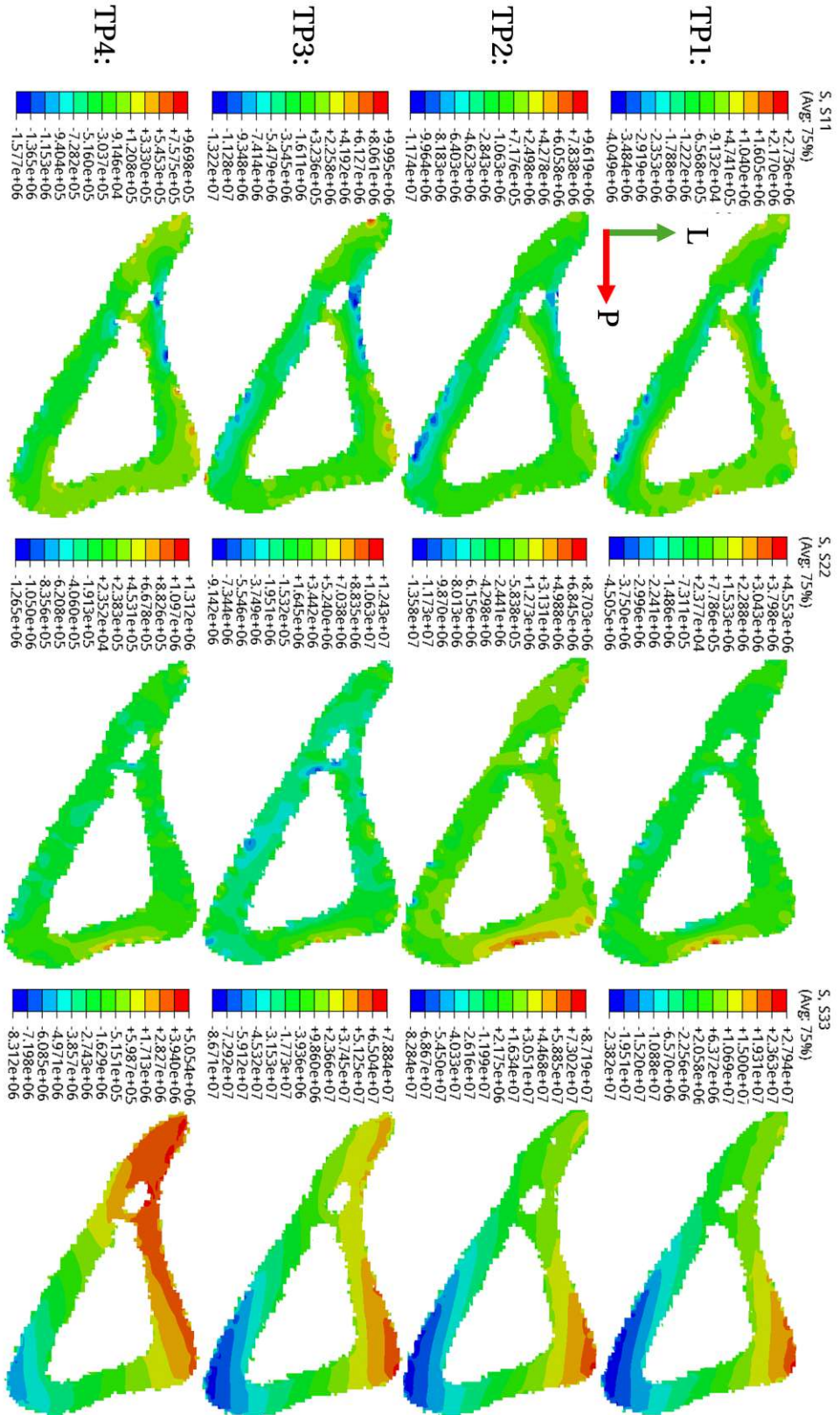


Figure 3.14: Stress results for the 37% section,  $E = 21 \text{ GPa}$ . Time points 1 to 4 are displayed top to bottom, stresses in the direction of the main axes are displayed from left to right in ascending order.

### 3. Results

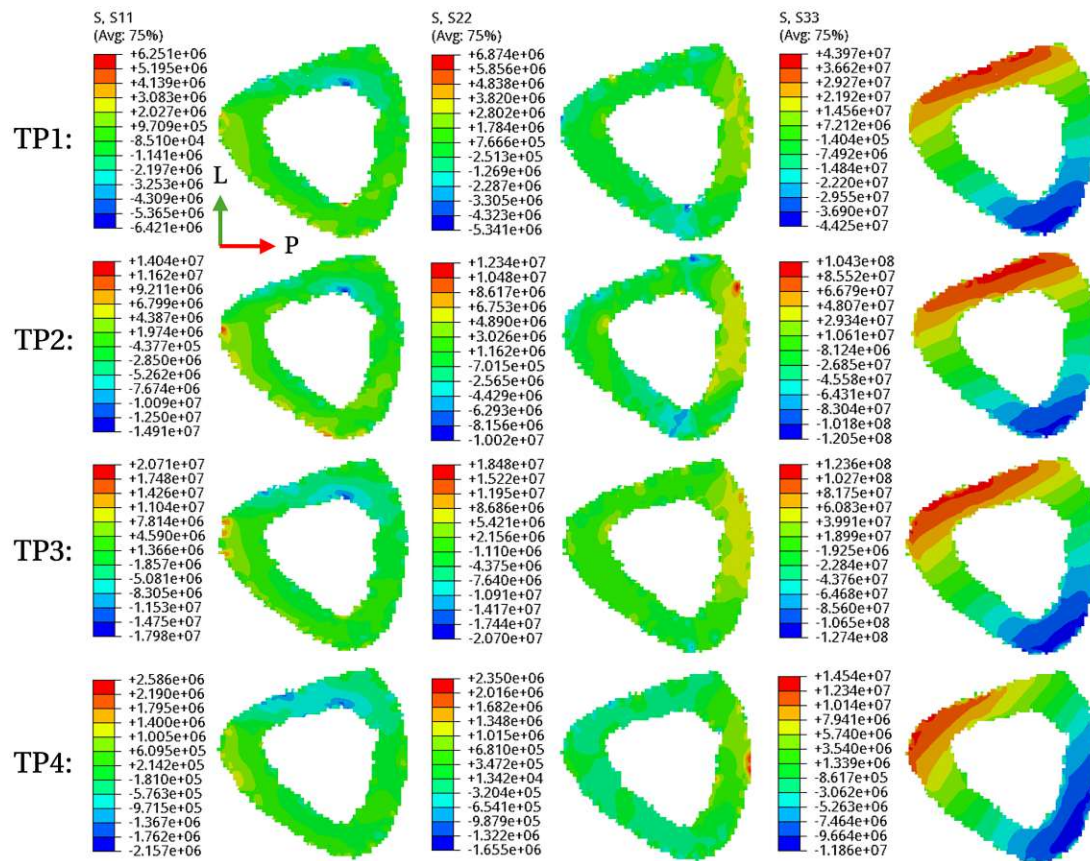


Figure 3.15: Stress results for the 50% section,  $E = 21$  GPa. Time points 1 to 4 are displayed top to bottom, stresses in the direction of the main axes are displayed from left to right in ascending order.

#### Including only muscles producing forces higher than 0.05N in the simulation

Muscles producing forces above 0.05 N for at least one point during the stance phase were M. biceps femoris posterior caudal, M. semimembranosus, M. rectus femoris, M. vastus medialis and M. vastus lateralis. Using only these five muscles and an elastic (tensile) modulus of 21 GPa, maximum stresses along the longitudinal axis of 4.81 MPa and -7.47 MPa are calculated for the 37% section, and 13.62 MPa and -11.44 MPa for the 50% section for TP3. Compared to the results of the simulation with all muscles included, the values for stress, regardless whether tensile or compressive and at which section, are significantly lower (94.48% lower for tensile, 91.39% lower for compressive stresses at the 37% section, 88.98% lower for tensile and 91.02% lower for compressive stresses at the 50% section). Regarding the stress profile, a slight rotation of the neutral line is observed, making the stress profile of TP3 appear similar to the profiles of TP4 in the simulations with all muscles included (see Figure 3.22).

Maximum strains along the longitudinal axis arise on the lateral side with  $228.1 \mu\epsilon$  and  $-351.9 \mu\epsilon$  on the medioposterior side for the 37% section at TP3. For the 50% section, maximum tensile and compressive strain values climb to  $630.9 \mu\epsilon$  and  $-545.8 \mu\epsilon$ , respectively (see Figure 3.22). This again poses a reduction in strains by 94.46% for tensile strains and 91.40% for compressive strains of the 37% section, and 89.33% for tensile strains and 90.92% for compressive strains of the 50% section.

Strain and stress profile progression from the 40% section proceeding proximally to the 20% section can be seen in Figure 3.21. As nicely visible in this figure, strain and stresses are larger at the diaphysis part.

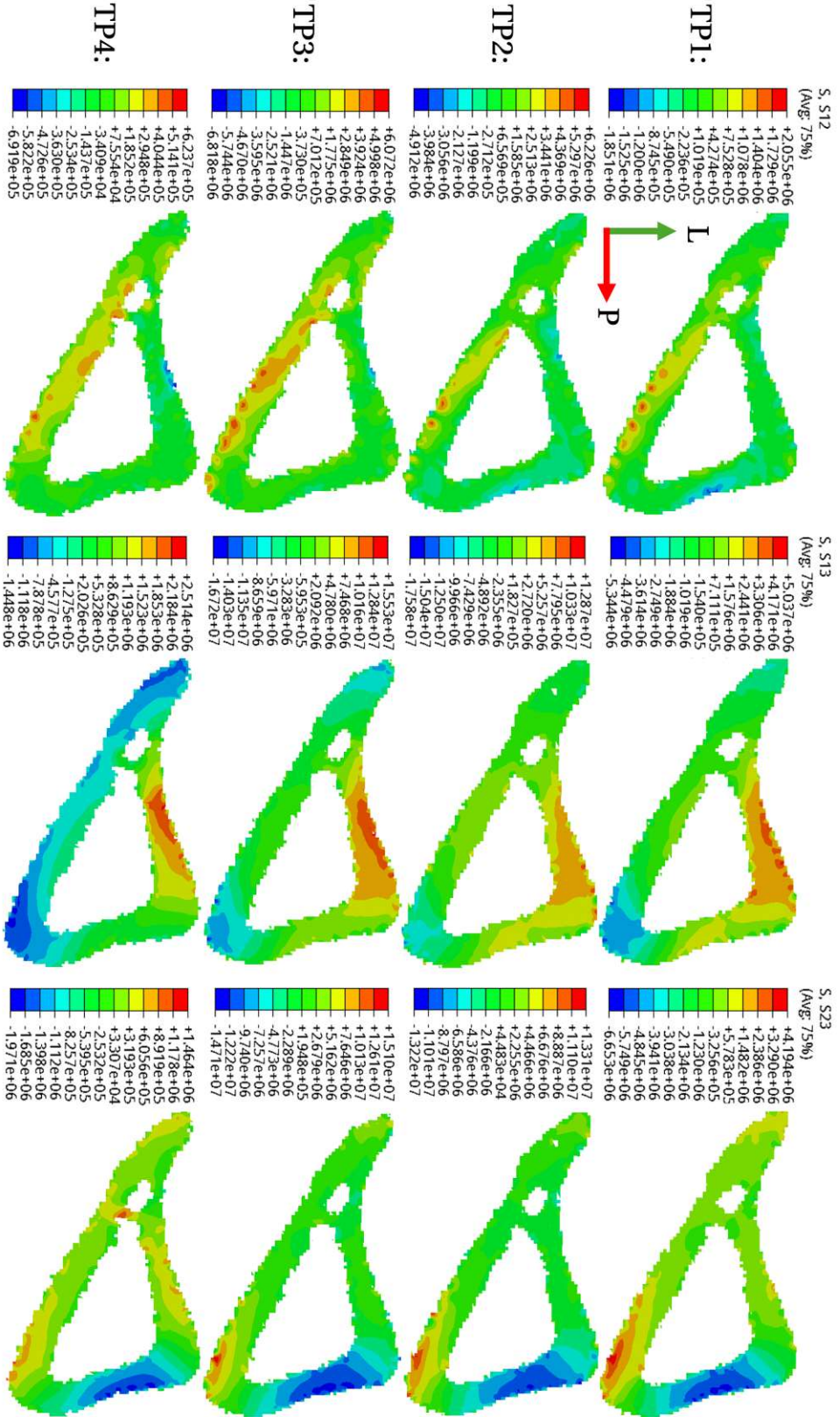


Figure 3.16: Shear stress results for the 37% section,  $E = 21 \text{ GPa}$ . Time points 1 to 4 are displayed top to bottom, strains are displayed from left to right in ascending order.

### 3. Results

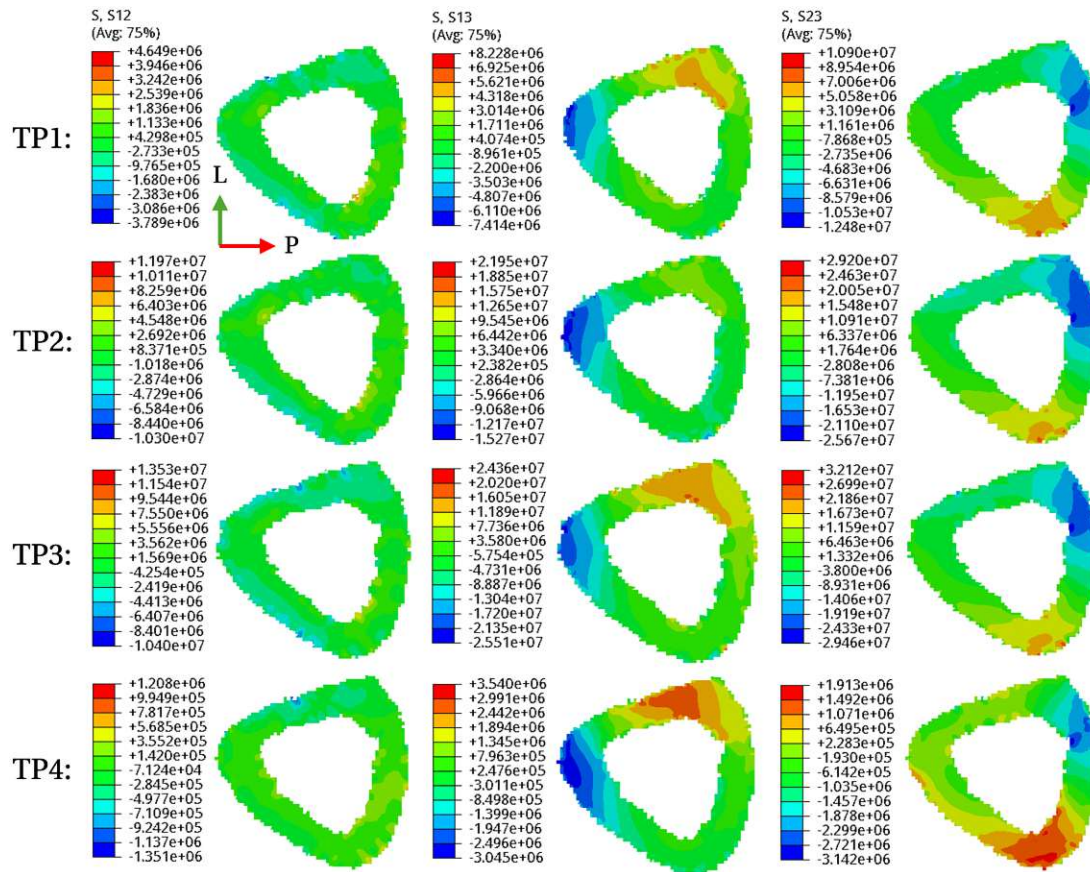


Figure 3.17: Shear stress results for the 50% section,  $E = 21$  GPa. Time points 1 to 4 are displayed top to bottom, shear strains are displayed from left to right in ascending order.

#### 3.2.4 Results for different force constraint areas

A reduction of the size of the force application constraint area results in an increase of stresses in tensile regions at the 37% section by 2.79% from 27.20 MPa to 27.96 MPa and a reduction of compressive stresses by 2.27% from 24.37 MPa to 23.83 MPa. Regarding strain in the 37% section, maximum values computed for the smaller area for TP1 are  $1613 \mu\epsilon$  and  $-1375 \mu\epsilon$ , signifying an increase by 1.70% and a reduction by 0.72%, respectively (see Figure 3.23).

For the 50% section, the area change had no effect on strain and stress.

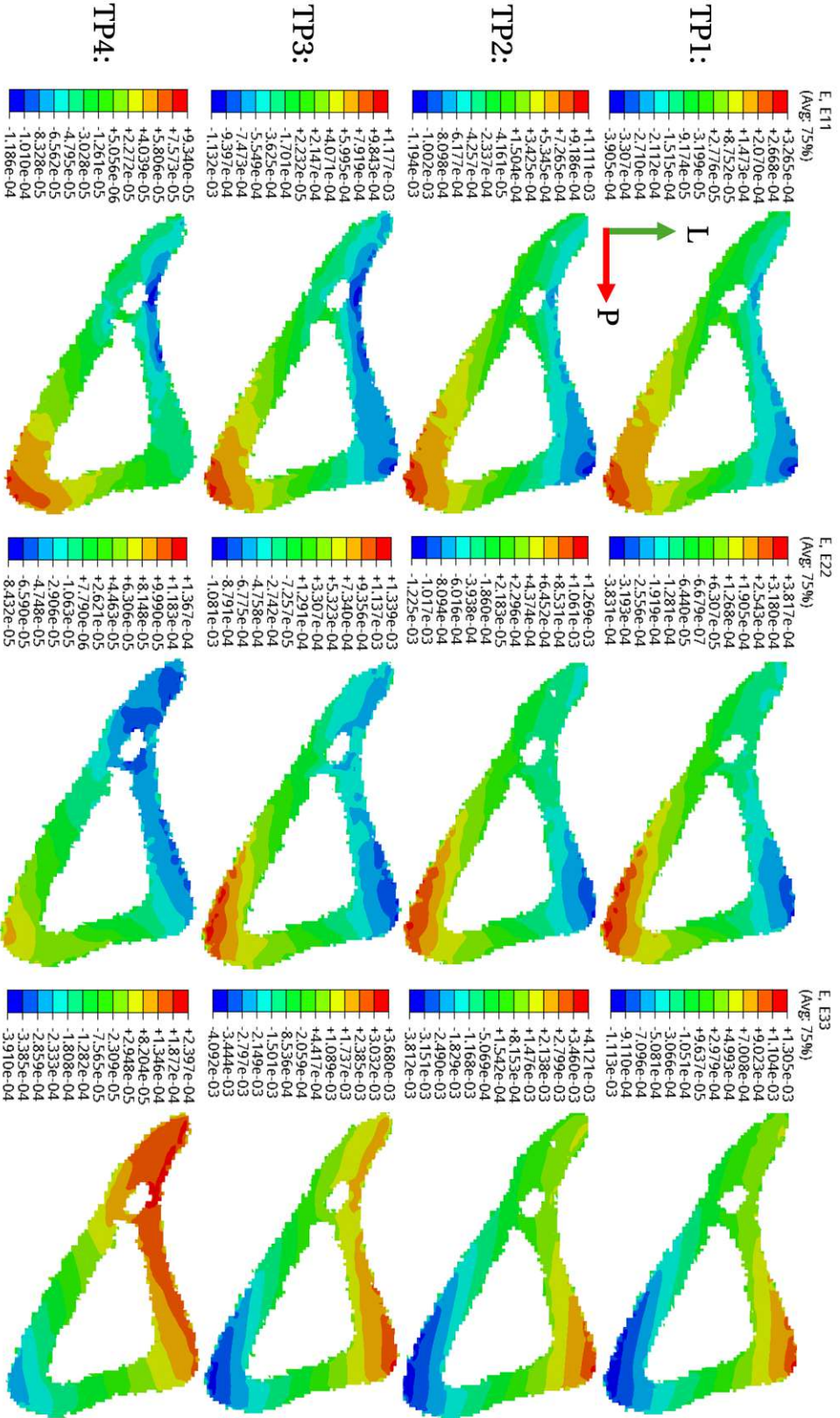


Figure 3.18: Strain results for the 37% section,  $E = 21$  GPa. Time points 1 to 4 are displayed top to bottom, strains in the direction of the main axes are displayed from left to right in ascending order.

### 3. Results

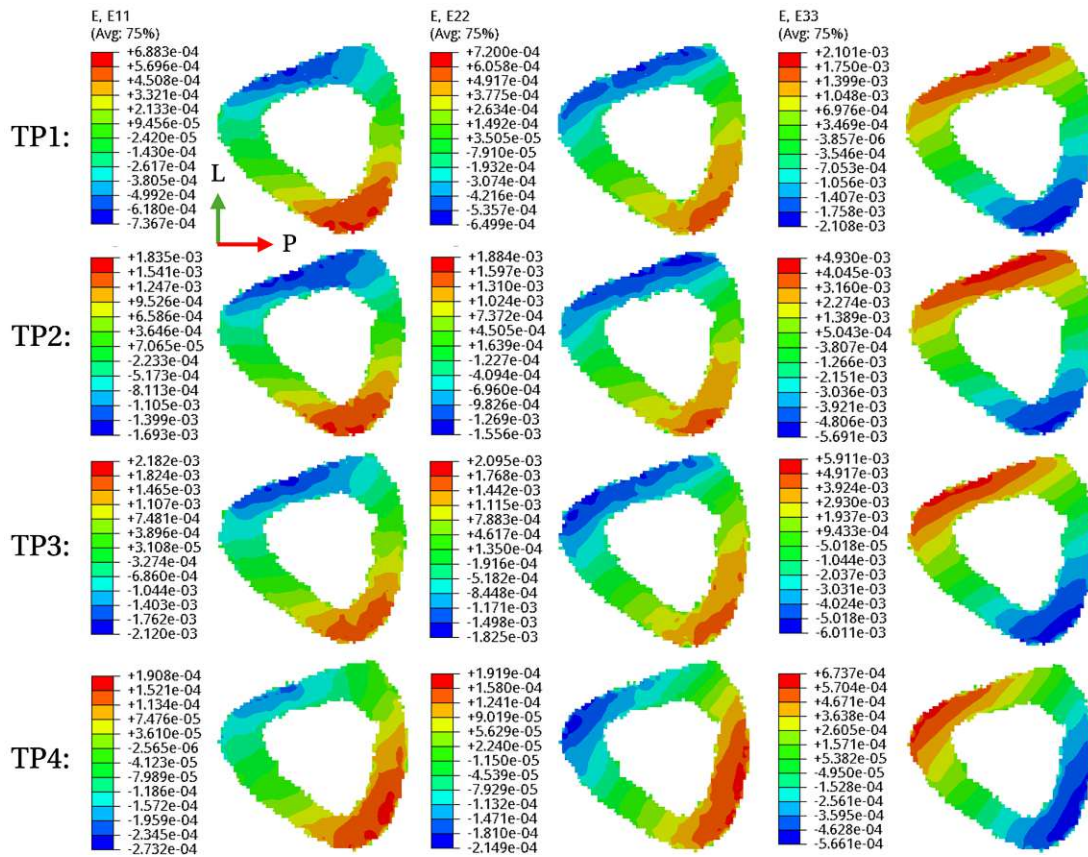


Figure 3.19: Strain results for the 50% section,  $E = 21$  GPa. Time points 1 to 4 are displayed top to bottom, strains in the direction of the main axes = are displayed from left to right in ascending order.

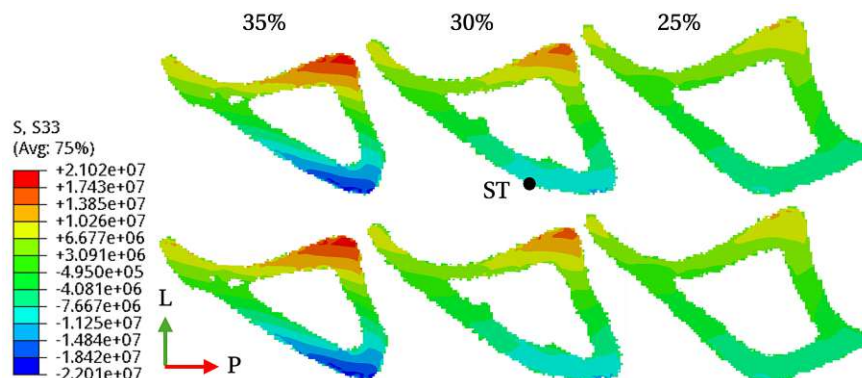


Figure 3.20: Stress results for the 30% section,  $E = 21$  GPa, where *M. semitendinosus* attaches to the surface medially.

		37%		50%	
		17 GPa	21 GPa	17 GPa	21 GPa
<b>max stress [MPa]</b>					
S11	tensile	11.53 (TP2)	9.995 (TP3)	20.70 (TP3)	<b>20.71 (TP3)</b>
S11	compressive	-13.21 (TP3)	<b>-13.22 (TP3)</b>	-17.98 (TP3)	-17.98 (TP3)
S22	tensile	10.37 (TP3)	<b>12.43 (TP3)</b>	18.48 (TP3)	18.48 (TP3)
S22	compressive	-18.69 (TP2)	-13.58 (TP2)	-20.70 (TP3)	-20.70 (TP3)
S33	tensile	87.11 (TP2)	<b>87.19 (TP2)</b>	123.6 (TP3)	123.6 (TP3)
S33	compressive	-86.09 (TP3)	<b>-86.71 (TP3)</b>	-127.4 (TP3)	-127.4 (TP3)
<b>max shear stress [MPa]</b>					
S12	tensile	5.881 (TP3)	<b>6.226 (TP2)</b>	13.53 (TP3)	13.53 (TP3)
S12	compressive	-5.874 (TP3)	<b>-6.818 (TP3)</b>	-10.40 (TP3)	-10.40 (TP3)
S13	tensile	15.20 (TP3)	<b>15.53 (TP3)</b>	24.36 (TP3)	24.36 (TP3)
S13	compressive	-17.58 (TP2)	-17.58 (TP2)	-25.50 (TP3)	<b>-25.51 (TP3)</b>
S23	tensile	18.51 (TP2)	15.10 (TP3)	32.12 (TP3)	32.12 (TP3)
S23	compressive	-14.71 (TP3)	-14.71 (TP3)	-29.46 (TP3)	-29.46 (TP3)
<b>max strain [<math>\mu\epsilon</math>]</b>					
E11	tensile	1434 (TP3)	1177 (TP3)	2695 (TP3)	2182 (TP3)
E11	compressive	-1473 (TP2)	-1194 (TP2)	-2619 (TP3)	-2120 (TP3)
E22	tensile	1639 (TP3)	1339 (TP3)	2587 (TP3)	2095 (TP3)
E22	compressive	-1512 (TP2)	-1225 (TP2)	-2254 (TP3)	-1825 (TP3)
E33	tensile	5086 (TP2)	4121 (TP2)	7302 (TP3)	5911 (TP3)
E33	compressive	-4937 (TP3)	-4092 (TP3)	-7424 (TP3)	-6011 (TP3)

Table 3.2: Maximum values of the FE simulations for 17 GPa and 21 GPa. Indicated in bold are values that are greater in the 21 GPa simulation compared to the 17 GPa simulation.

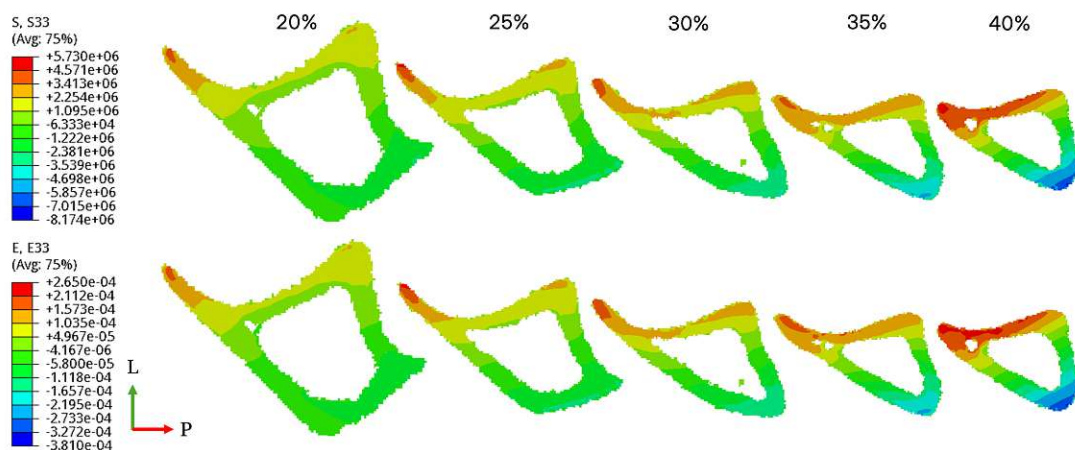


Figure 3.21: Stress and strain results for sections 20 to 40% using only muscles producing forces above 0.05N.

### 3. Results

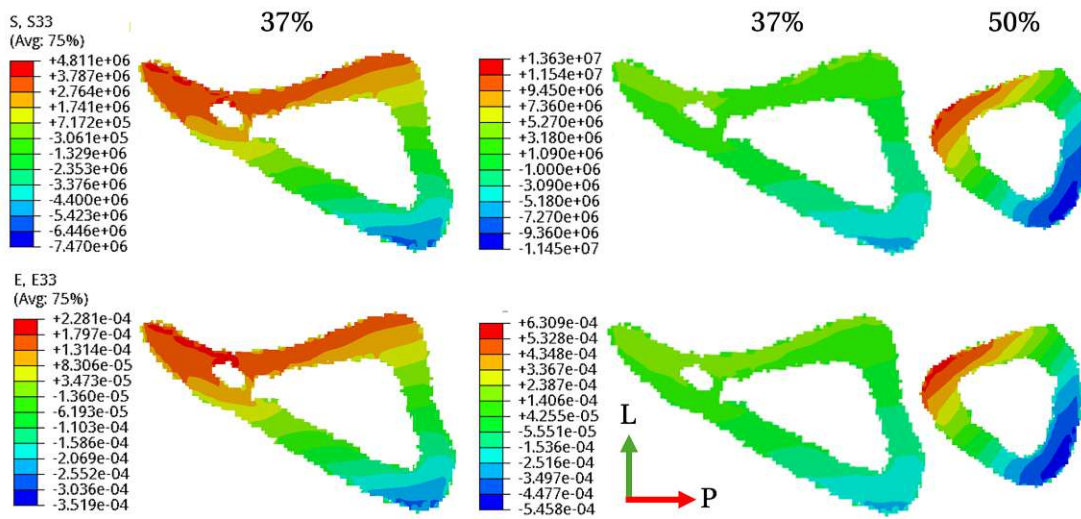


Figure 3.22: Stress and strain results for sections 37% and 50% using only muscles producing forces above 0.05N. Left: 37% section with adjusted value range to section, middle and right: both sections using the same value range.

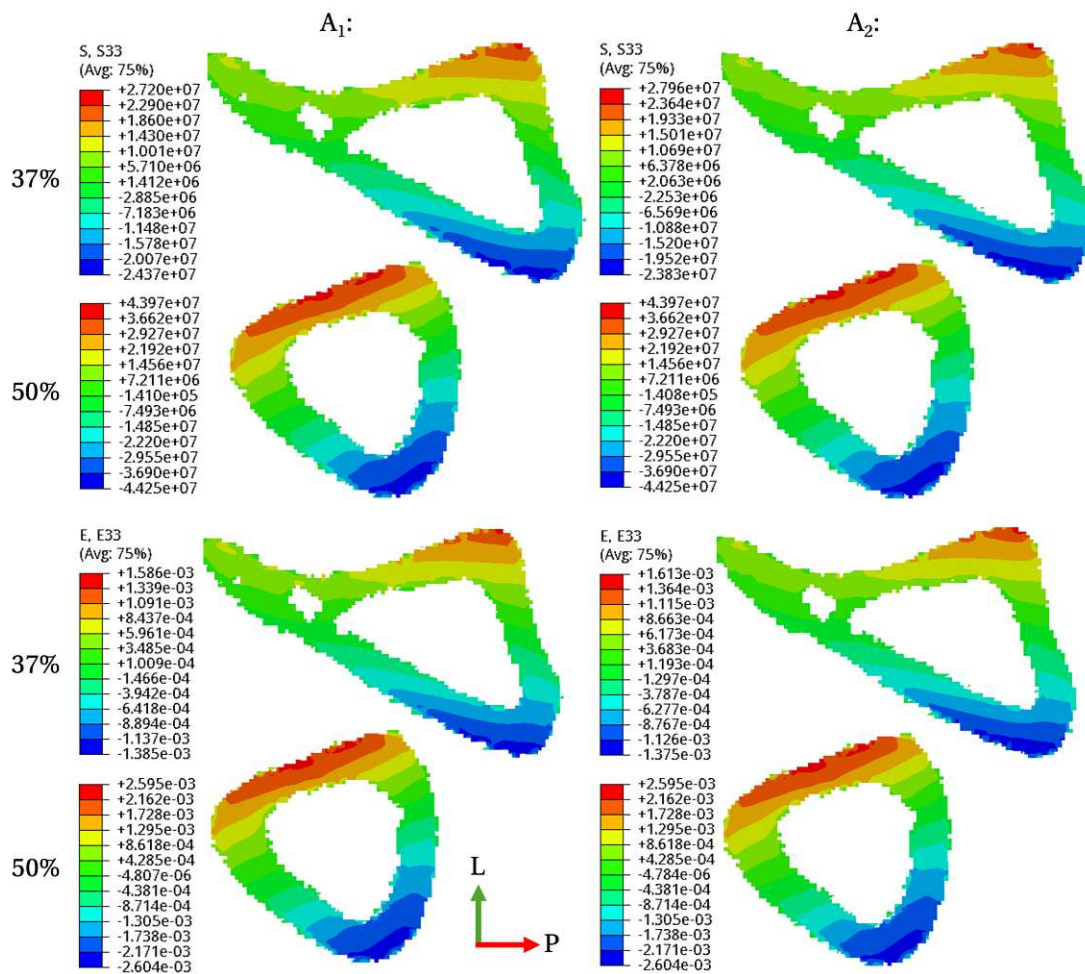


Figure 3.23: Effect of area of force constraint variation, evaluated for TP1 with 17 GPa.

# Discussion

We sought to develop a comprehensive modeling pipeline for the assessment of stress and strain patterns in the mouse tibia during the stance phase. We pursued this goal by combining state-of-the-art MS and FE models and explored variations of both, which are discussed now.

## 4.1 Musculoskeletal modeling outcomes

### 4.1.1 Comparison of the two models of Charles et al. and their results

#### Inverse kinematics and ground reaction force data

Comparing the kinematic input data (visible in Figure 2.4) of the two used models, the biggest difference is observed at the hip angle, which is shifted to almost exclusively positive values in the 2024 model, while staying mostly in the negative range in the 2018 model. This results from the different bearings of the models. The 2018 model's hip is fixed in space to the ground, while in the 2024 model, the whole model is moving in space, which influences the orientation of the pelvis (nicely visible when comparing Figures 4.2 and 4.3). This difference of being fixed to the ground as well as slight differences in the models also explain the differences in the other two curves for knee and ankle angle.

Regarding the altered GRFs with focus on the right leg, a third component was added to the force profile into the mediolateral direction. Its course hints that James Charles expects there to be a slight loading into medial direction (small peak with  $-0.045\text{N}$ ), before considerable loading mainly into the lateral direction was implemented (rise to  $0.212\text{N}$ ) (see Figure 2.5).

#### Inverse dynamics results

The differences in kinematics still had tremendous influences on the results of the inverse dynamics step, as can be seen in Figure 4.1. While we were able to reproduce the graph 4.1A of Charles et al. (2018) paper for the 2018 model, the results of the 2024 model differed significantly from the 2018 results. The net hip adduction moment, due to the above mentioned reasons, was highly increased (see Figure 4.1B) and therefore also hidden in the second 2024 model plot (4.1C), where it becomes apparent that the ankle flexion moment was the only parameter still following a similar shape as it exhibited in the 2018 model. 2024's knee extension moment also shows similarities to its 2018 version, but rising to higher values during the second phase of the stance phase and staying positive until the termination of the stance phase. The resulting larger extension of the knee joint is nicely visible upon comparing Figures 4.2 and 4.3. The hip flexion moment, negative for the whole of the 2018 stance phase is showing a similar shape to the 2024 knee flexion moment, also climbing to positive values and remaining there, resulting in this increased hip flexion visible in Figure 4.3 for initial contact and loading response.

#### Static optimization results

Comparing muscle activations of the 2018 (Figure 3.1) to the 2024 model (Figure 3.4), three differences become apparent: In the 2018 model, more muscles are involved in knee flexion

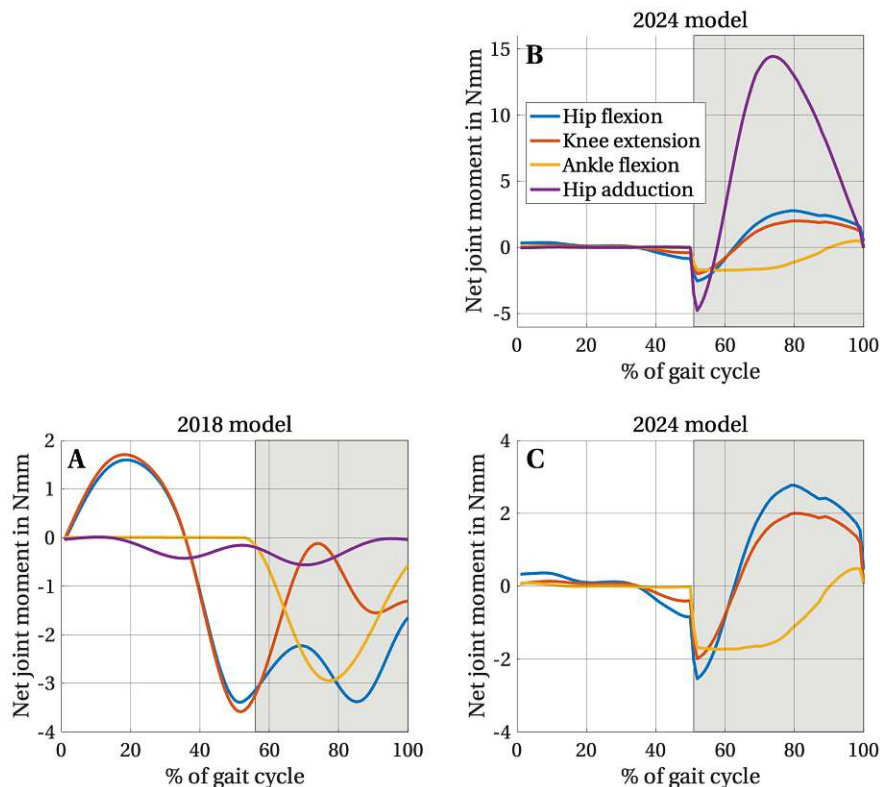


Figure 4.1: Results of inverse dynamics tool: A: Results of 2018 model; B: Results of 2024 model including hip adduction; C: Results of 2024 model without hip adduction for better comparison.

(primarily SM, ST and POP), while in the 2024 model, SM was determined as mainly active. For knee extension during swing phase, VL is active in both models, but to a much greater extension in the 2018 model. During stance phase, RF is the main player in extending the knee in the 2018 model, while it only plays a supporting role to VL in the 2024 model. The last striking difference is that in the 2018 model, the ankle plantarflexion is attributed to PL, while in the 2024 model, the movement is carried out by FDL.

All muscle activities appear plausible when looking at Figures 2.4, 4.2 and 4.3. At the start of the swing phase, knee extensors are active, resulting in a rather elongated hindlimb. During the second half of the swing phase, primarily during the terminal swing phase, the knee flexion angle increases due to the activity of knee flexors (SM, ST and POP in the 2018 model and SM in the 2024 model) reflected in both the graphs of Figure 2.4 and the graphical representation of the models (Figures 4.2 & 4.3). At the beginning of stance phase, the knee is most flexed before knee extensors peak again (RF in the 2018 model and VL and RF in the 2024 model), causing an extension of the knee joint.

Regarding the ankle joint, activity was only computed for time points close to the transition from swing to stance phase, where dorsiflexors followed on plantarflexors in the 2018 model. There was no “push-off” as known from human gait analysis in the 2018 model. The 2024 model showed increased dorsiflexor activity at the end of the stance phase, which also does not equate to push-off, but could be counted as physiological as a measure to increase ground clearance in the pre-swing phase. One possible explanation for the difference in the models regarding the ankle joint could be the splitting of the ‘toes’ segment of the 2018 model into two distinct segments ‘foot and ‘toes’ in the 2024 model. The prolonged activity of FDL during the stance phase in the 2024 model could make sense in that the muscles counteracting dorsiflexion taking place during loading response (i.e. plantarflexors) need to increase their force to keep the joint stable. Another possible explanation could also be artifacts in the reconstruction of the kinematic data due to the splitting of the body ‘toes’.

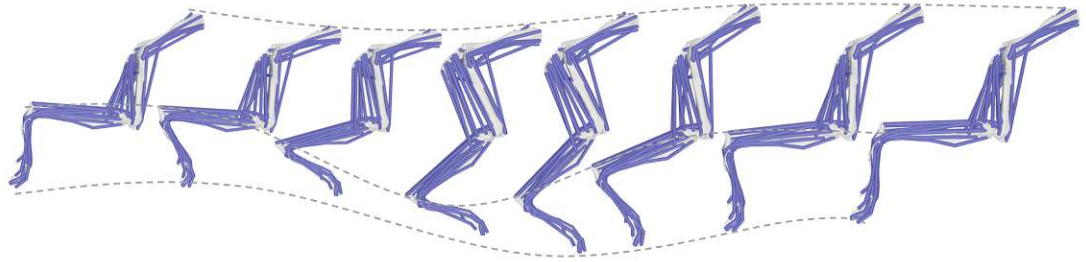
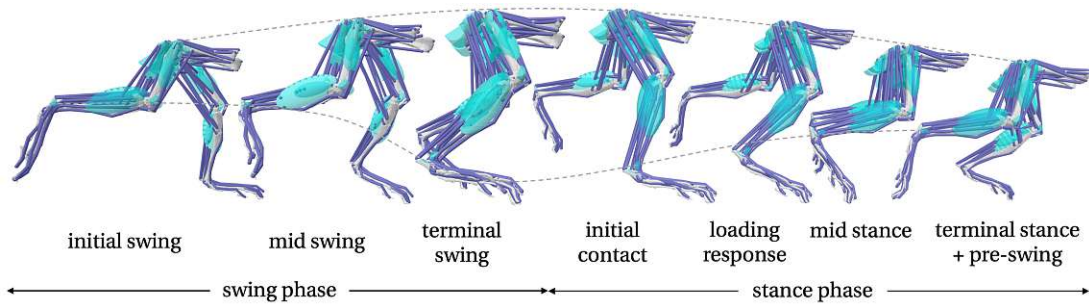


Figure 4.2: One whole gait cycle of the 2018 model.

Figure 4.3: One whole gait cycle of the 2024 model, including terminology for the single phases (adapted from [Harris and Wertsch \(1994\)](#)).

### Joint reaction analysis results for the knee joint

Regarding the knee joint, the changes manifested in lower forces in the x- and y-direction during the swing phase in the 2024 model, with overall similar shapes of the curve progressions in the stance phase, but slightly higher values or the force in x-direction and lower values for the force in y-direction (see [Figure 4.4A and C](#)).

When taking the coordinate reference frame definitions of the single segments (see [Figure 2.7](#)) into account, the above recorded observations correspond to less force needed to keep the tibial bone from slipping off the femoral condyles in opposite direction of the force of gravity vector (decreased force in x-direction), and less force needed to keep the articulating surfaces of the bones on top of each other (decreased force in y-direction).

During stance phase, the force in y-direction becomes negative, indicating force acting on the joint due to loading by the body weight upon ground contact of the hindlimb. Why this is significantly lower in the 2024 model (approximately half of the force in y-direction of the 2018 model), cannot be explained. However, given the physiological load of running, forces of 6xBW are more plausible than up to 12xBW, as they occur in the 2018 model. The rise of the force in x-direction during stance phase to higher values can also be explained by increased need to keep the tibial bone from slipping off the femoral condyles due to increased load on the joint.

Regarding the changes in the moment curves, the biggest difference lies in the course of the torsional moment around the y-axis, which is positive in the 2024 and negative in the 2018 model during the stance phase (see [Figure 4.4B and D](#)). This could be explained through the additional ground reaction force included in the 2024 model in z-direction that used to be 0 for the whole gait cycle in the 2018 model as explained above. This GRF component could also serve as an explanation for the course and the higher maximum of the bending moment around the x-axis especially during the second part of the stance phase (see [Figure 4.4D](#)).

### Joint reaction analysis results for the ankle joint

Subsequently, we expected larger deviations of the 2024 model from the 2018 one at the ankle joint, being closer to the point of GRF application. The changes induced to the 2024 model resulted in an inversion of joint reaction forces in x- and y-direction in comparison to the 2018 model (see [Figure 4.5A and C](#)). Forces in y-direction, peaking to positive values of more than

## 4. Discussion

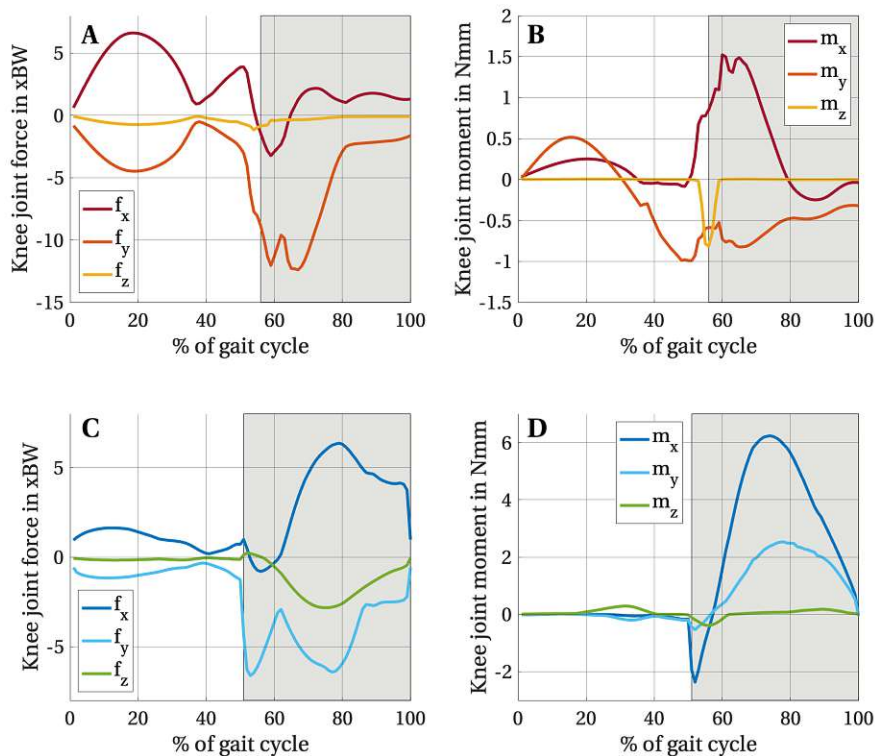


Figure 4.4: Results of joint reaction analysis tool for the knee joint: A & B: Results of 2018 model; C & D: Results of 2024 model

11xBW at the beginning of the stance phase, were mainly responsible for counteracting the force generated on the articulating surface of the body ‘foot’ by the loading with body weight due to initial contact to ground. In x-direction, negative values were computed for the 2024 model at initial contact to ground, indicating that the joint had to compensate to avoid sliding of the tibial bone into cranial direction (to the front). Both explanations of the calculated numbers make physiological sense.

The slight differences in the force in z-direction could be explained by the additional GRF in z-direction, as already mentioned above. Overlaying the GRF in z-direction course with the course of the force in z-direction of the 2018 model would result in something similar to what was calculated for the force in z-direction of the 2024 model.

Regarding the moments of the 2024 model (see Figure 4.5B and D), the moment around the z-axis showed a completely different course, staying close to zero for the most part, indicating that muscle forces in addition to other forces acting on the joint were well balanced (comparing the values of the muscles in Fig 3.4C and D). In comparison, in the 2018 model, ankle dorsiflexors exhibited a force two times as high as ankle plantarflexors.

The moment around the x-axis, influenced by the additional GRF component in z-direction, mimicked the latter’s course by dipping to negative values first before rising to positive values slightly higher than in the 2018 model. The moment in y-direction was negative for the majority of the stance phase, indicating more torsion than in the 2018 model, also explainable by the existence of an additional GRF component in mediolateral direction.

### 4.1.2 Comparison of the 2024 model to Prasad et al. 2010 MS model

For an overview of the differences between the model used by Prasad et al. (2010) to characterize gait induced normal strains, please also see Table 4.1.

The most important differences between the models of Prasad et al. (2010) and Charles et al. (2018) are the different running speeds (the mice of Charles et al. (2018) ran almost double the speed the mice in the data Prasad et al. (2010) used), the different ages and weights of the mice and the different amounts of muscles used in the models. While Charles et al. (2018) collected

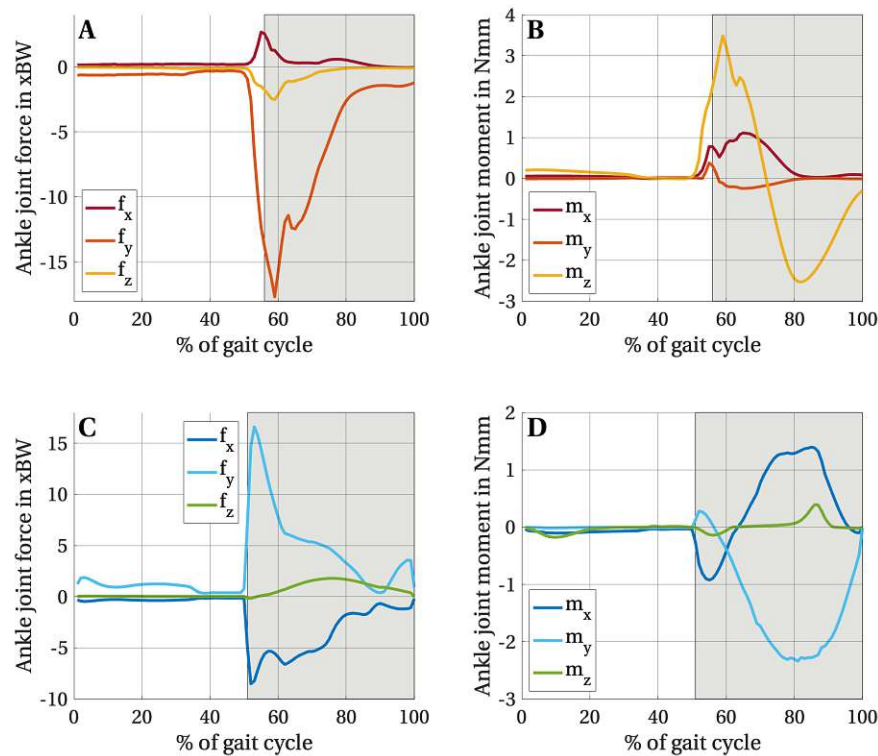


Figure 4.5: Results of joint reaction analysis tool for the ankle joint: A & B: Results of 2018 model; C & D: Results of 2024 model

own data, Prasad et al. [2010] used a collection of previously published data to construct their model. These include kinematics from Akay et al. [2006] and Leblond et al. [2003], GRFs from Zumwalt et al. [2006] and data on mouse anatomy from Leblond et al. [2003] and Lepicard et al. [2006]. Their analysis was ground on a model with the same five segments as Charles et al. [2016] used, modeled as one-dimensional rigid links, whose kinematics were determined by joint angles and hip crest height. The crucial difference is that they included only one muscle termed “calf muscle” that balanced out ankle moments calculated from kinematics and GRF data. Charles et al. [2016] instead used 44 musculotendon units to actuate the model, which are also then incorporated in the FE model.

They also used an FE analysis for the subsequent study of gait induced normal strains, but in contrast to the present study, applied the results of the inverse dynamics step to the distal end of the tibia. Furthermore, this study used an additional step (joint reaction analysis) to apply joint reaction forces and moments to the proximal part instead.

Prasad et al. [2010] did not publish results of the inverse dynamics step, making it hard to compare the different loading conditions for the subsequent FE analysis. But results of the FE analysis will be discussed in the FE section.

#### 4.1.3 Comparison of the 2018 & 2024 model results to other results in literature

Dienes et al. [2022] were the first to calculate 3D joint-by-joint kinetics needed for the actuation of rat models and quantified the forces experienced by the hindlimb joints. They modified the previously mentioned rat hindlimb model developed by Johnson et al. [2008], but recorded own kinematic and GRF data (Dienes et al. [2019]). In contrast to the data recorded by Charles et al. [2018], motion capture was carried out with reflective markers placed on shaved skin close to joint centers and GRFs were recorded in 3DOFs, which allowed for better spatial reconstruction of the location of the respective reference points in space to calculate joint angles. The running speed was predetermined by placing rats on treadmills running at a speed of 0.4 m/s. Furthermore, their rats weighted an average of  $180.0 \pm 7.8$ g, which is nine times the weight of the mice of Charles et al. [2018]. They were also slightly older with an age of 12 weeks.

#### 4. Discussion

	Prasad et al. [2010] model	Charles et al. 2024 model
Age and weight of mice	16 weeks, female, $\approx 24$ g	42 days, male, $(20.9 \pm 0.8)$ g
Kinematics	derived from Akay et al. [2006] and Leblond et al. [2003], planar hindlimb motion (no ML components)	own, recorded with 2 cameras (dorsally and laterally) and reconstructed with markers on skin
Mouse running speed	$\approx 0.3$ m/s	$\approx 0.59$ m/s
GRFs	adapted from Zumwalt et al. [2006]	own, custom-built strain gauge based acrylic force plate
Mouse anatomy	from Leblond et al. [2003], Lepicard et al. [2006]	own (Charles et al. [2016])
Analysis	11 time points	continuous
Number of bodies	5	5
Number of muscles	1	44

Table 4.1: Comparison of the model used by Prasad et al. [2010] to the model used in this study

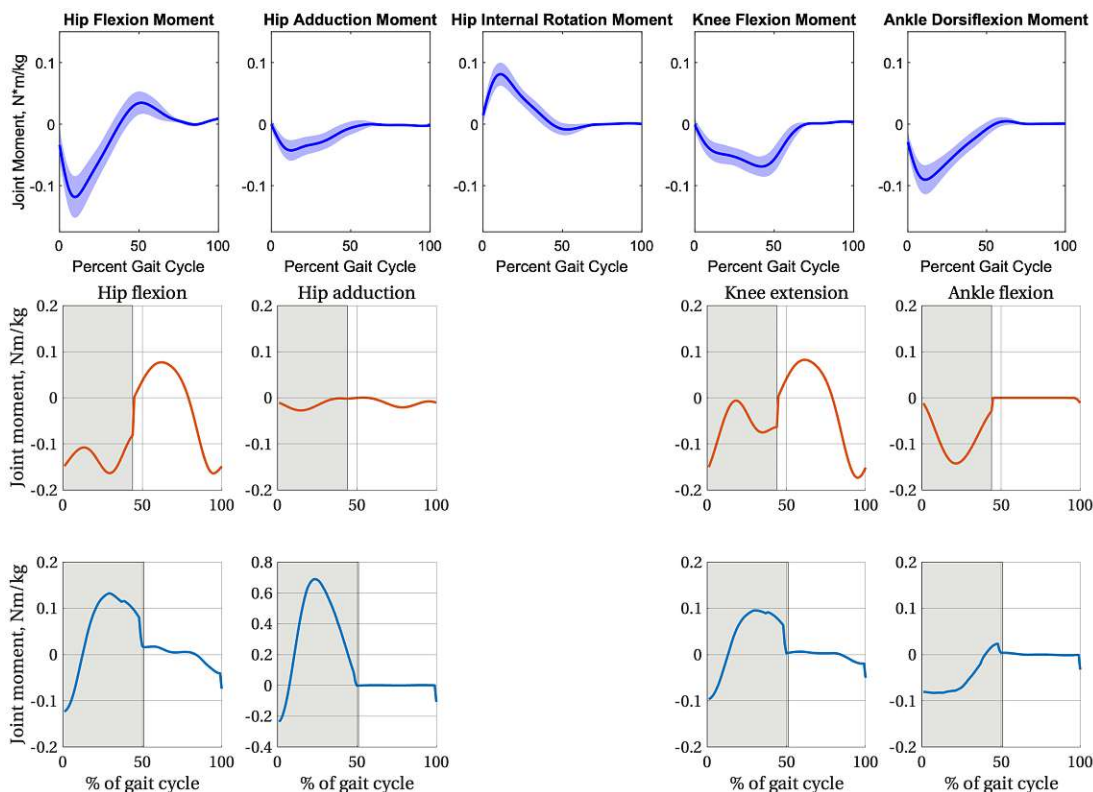


Figure 4.6: Results of the inverse dynamics step of Dienes et al. [2022] and of both models, top: results of Dienes et al. [2022], middle: 2018 model, bottom: 2024 model. Displayed with stance phase first for better comparison to Dienes et al. [2022] results.

Comparing the net joint moments results (inverse dynamics) of the validated 2018 mouse hindlimb model to the ones of the rat hindlimb model, the following statements can be made: Firstly, ankle flexion seems to be very similar in both animals, as the models showed very similar progressions of the graphs for the ankle dorsiflexion moment (see red graphs in Figure 4.6). Regarding knee extension, the graph of the 2018 mouse model shows first extension and then flexion during the swing phase, while the rat model graph shows no change in knee flexion moment. During stance phase, both models exhibit knee flexion, but to different extents. Due to possibly different hip fixations in space, hip graphs do not match.

Upon comparing the results of Dienes et al. [2022] to the results of the 2024 model, more similarities can be observed, which, explained by the existence of a second leg in the 2024 model and the therefore more similar kinematics of the hip, seem plausible. The ankle dorsiflexion moment again follows a similar path, despite starting at a lower value than in the rat model. The knee flexion moment of the 2024 model starts in flexion, but is mainly in the extension range during stance phase, which is similar to the rat model. Both models exhibit a knee flexion moment of close to zero at swing phase, which is new in the mouse model comparing the 2018 and 2024 version. The hip adduction moment is a lot higher in the 2024 model than what Dienes et al. [2022] reported for the rat model, but the curves of the hip flexion moment are again following a similar path.

To conclude, the 2024 model was certainly an improvement to the 2018 model, but has its limitations that will be addressed in the *Limitations* section.

## 4.2 Finite Element modeling outcomes

### 4.2.1 Changes induced by a higher elastic (tensile) modulus

Two different elastic (tensile) moduli were implemented to check the influence on stress and strain results, based on considerations and previous activities of the research group.

As listed in the results, a higher elastic (tensile) modulus did not necessarily result in lower stresses as might expected (see Table 3.2 for an overview). It did result in a lowering of maximum compressive stresses along the axis pointing laterally and tensile stresses along the axis pointing posteriorly in the 37% section. Maximum compressive stresses along the axis pointing posteriorly were not changed by the higher elastic (tensile) modulus in the 37% section. All other maximum stresses, i.e. tensile and compressive stresses along the longitudinal axis and tensile stresses along the axis pointing laterally and posteriorly were higher than in the 17 GPa simulation. This is explored in more detail in the following paragraphs.

Looking at the two S22 stress profiles in Figure 4.7, pictured for a second time for better comparison, it becomes apparent that not only do the maximum tensile stresses rise by more than 2 MPa in this particular case, but the compressive stresses fall to a significantly lower value, losing more than 5 MPa (more than a third of the original value) in this case. On top, the stress profiles visibly differ in the first and second main direction. There are three possible explanations for this: 1) the mechanical contribution of the fibula changes with the allocated cortical stiffness, 2) the muscle attachments are not accurate and 3) the model has not converged yet.

Hypothesis 1 was tested and is further explained here. Tibia and fibula (which is not shown in the graphs of the FE results due to insignificantly low stress and strain values) are connected

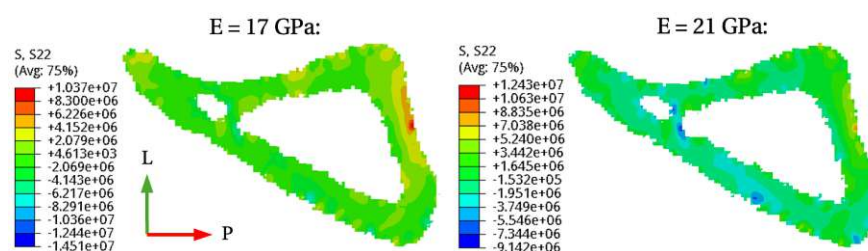


Figure 4.7: Stress results into y-direction of TP3 for better comparison

## 4. Discussion

	37%		50%	
	17 GPa	21 GPa	17 GPa	21 GPa
<b>TP1</b>	0.38780	0.38783	0.37532	0.37532
<b>TP2</b>	0.17052	<b>0.17040</b>	0.13583	<b>0.13581</b>
<b>TP3</b>	0.63974	0.63976	0.64733	0.64736
<b>TP4</b>	0.15168	0.15170	0.15626	0.15627

Table 4.2: Forces normal to 37% and 50% sections given in N. Indicated in bold are forces that are smaller in the 21 GPa simulation.

proximally via the tibiofibular interface. Due to their slightly curved but different shapes, the two connected parts could influence each other depending on their respective cortical stiffness, resulting in a shift in how the load is distributed through the tibiofibular structure. To test this hypothesis, the forces normal to the 37% and 50% section were extracted and can be seen in Table 4.2. If this hypothesis was true, the forces normal to the sections would need to be lower in the 21 GPa simulation, which was not the case for three out of four time points. In addition, differences usually only occurred to the third or fourth decimal place, which can be considered negligible in view of the accuracy of FE models. Next to the forces normal to the sections, the location of the centroid of each section would also have to shift to a location closer to the fibula in the 21 GPa simulation, which could not be observed with the naked eye.

It could be the case that the muscle attachments are not precise and therefore also influence the stress and strain profiles with higher elastic (tensile) moduli (hypothesis 2), but this was not investigated further as it would have gone beyond the scope of this thesis.

The third hypothesis of the model not having converged yet was also not tested due to the lack of original  $\mu$ CT data and time. Another approach to possibly solving this issue would be to switch from hexahedral to tetrahedral elements, which would make the mesh less prone to problems originating from the many corners and edges of the hexahedral elements.

The observed stress profile variations in the first and second main direction with small differences could for some parts also be due to numerical noise (not valid for big differences such as seen for S22 at TP3, pictured in Figure 4.7). In general, the numerical results of S11 and S22 are also an order of magnitude smaller compared to the third main direction, which is the longitudinal direction and also the direction of main interest.

In contrast to the stress results, maximum strains into all main directions got lower due to the higher elastic (tensile) modulus both in the 37% and the 50% section.

Looking at Figure 4.8, where the changes in elastic (tensile) modulus for one time point (TP3) are displayed in longitudinal direction, the direct influences can be observed. While the stresses in the 37% and 50% sections changed little or not at all in this direction and the stress and strain profiles also remained the same, the change in the elastic (tensile) modulus had an impact on both the maximum tensile and compressive strains in both sections.

### 4.2.2 Muscle variation studies

Two different setups of the model were tested with regard to muscles. First, the influence of a single muscle, M. semitendinosus, was evaluated, as the muscle attaches to the bone close to the sections of interest (37% and 50%). As stated in the results section, the muscle increased the maximum compressive stresses by 0.78% and decreased maximum tensile stresses by 0.25%. This resulted in changes of the tensile maximum strain by 0.3% higher values and 0.28% lower values for the compressive maximum strain. It was therefore deemed appropriate to include muscles closer to the sections of interest with moderate force progressions if implemented with multi-point constraints to reduce stress concentration.

The second study was conducted to check for the influence of smaller muscles. Consequently, only muscles producing at least at one time point of the stance phase more than 0.05 N force

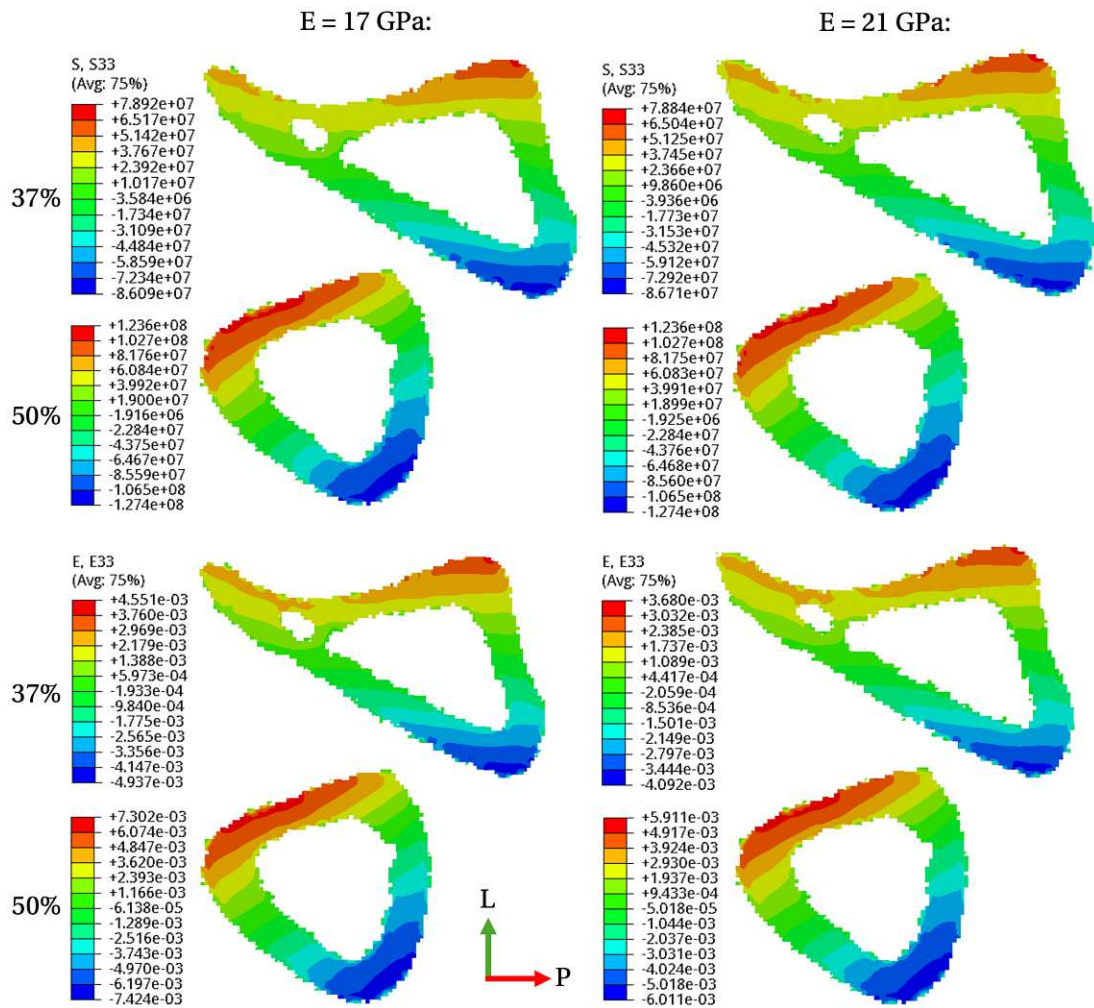


Figure 4.8: Effect of elastic (tensile) modulus variation for one time point (TP3), displayed in longitudinal direction.

were included in the model. With regard to the found results, i.e. that the results of a simulation with all muscles and a simulation with only the “main players” produced greatly different stress and strain maximum values (see Figure 4.9), it was first argued that muscles producing smaller forces are of great importance and cannot be left out. This is also supported by literature (Martin et al. [1998], Burr [1997], Lu [1997]), where Lu [1997] in particular points out that muscles apply tensile forces, thereby increasing compressive axial force levels in the bone at the site of attachment (replicated in the first muscle study). Burr [1997] even states that loads inflicted on bones due to muscle forces are greater than those triggered by gravitational forces associated with weight.

The latter claim was indeed tested and - consistent with the logic of the results gained for the variation study described above - stresses and strains were expected to decrease to levels reported by De Souza et al. [2005], Sugiyama et al. [2012], Patel et al. [2014] for the tibial compression test if only joint reaction forces are applied to the FE model. Instead, the results obtained (which are not presented in this work) were rather counterintuitive - instead of reduced strain magnitudes, the exclusion of the muscles (which in effect equates to a reduction in load) led to increases in specific strain tensor components. The reasons for these observations have not yet been clarified and suggest that further in-depth studies and a review of the numerical implementation could be beneficial to address this finding exhaustively.

#### 4.2.3 Variation of force application constraint area

As stated in the results section, the variation of the area of which the movement was restricted to the point where forces and moments calculated for the knee joint were applied, influenced

#### 4. Discussion

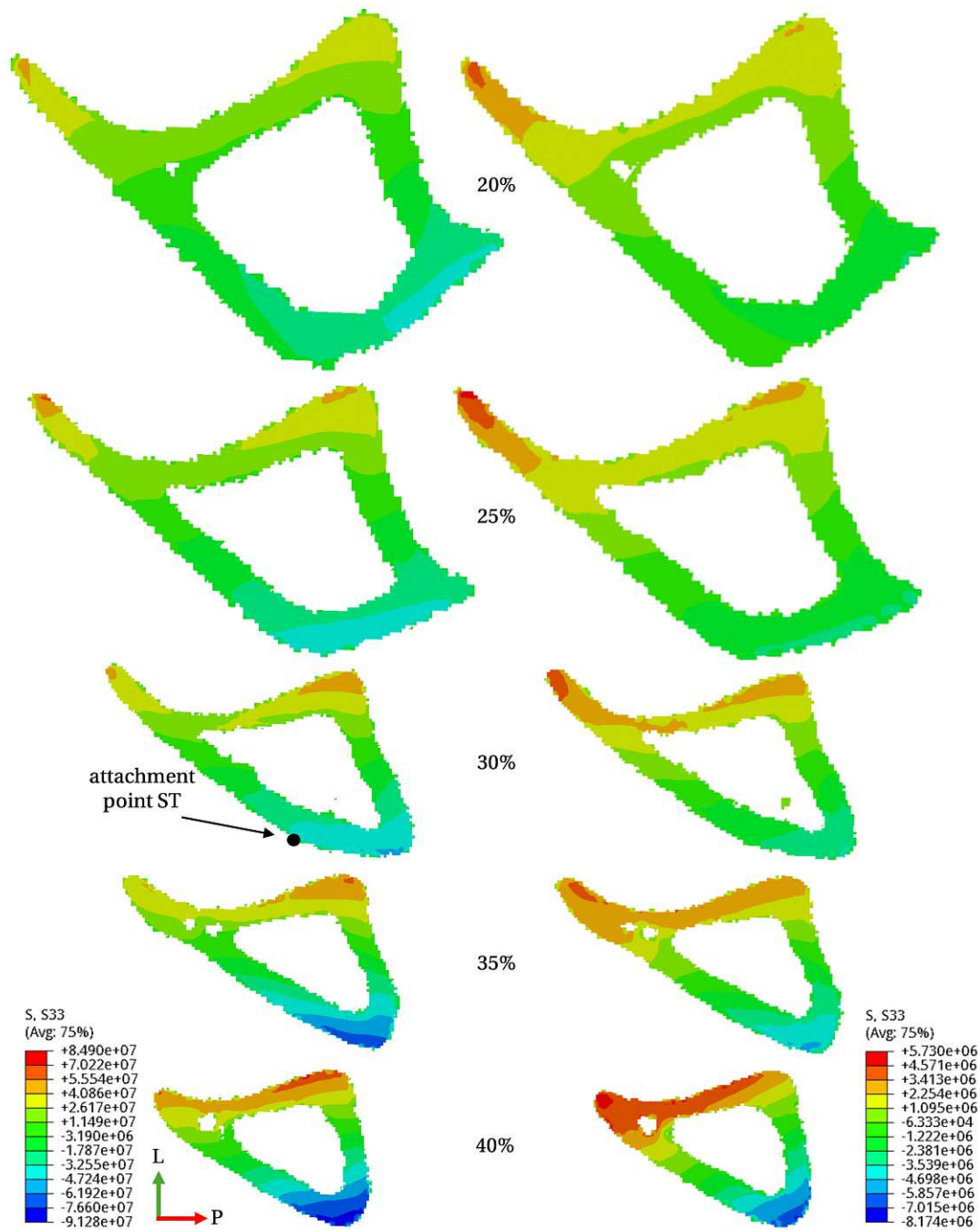


Figure 4.9: Comparison of stress profiles along the proximal bone, left: simulation using all muscles, right: simulation using only the "main players".

the results only in the 37% section, by 2.79% higher tensile and 2.27% lower compressive stresses and 1.7% higher tensile and 0.72% lower compressive strains with a smaller area at the points of contact between the femoral condyles and the tibial plateau. Therefore, there is certainly potential in improving the location of the area of force application constraints in further studies, but its effect was judged to be small enough for first calculations and a proof-of-concept of the presented modeling pipeline.

The choice of the used boundary conditions in general is further discussed in the *Limitations* section.

#### 4.2.4 Results of the bending and torsional moments

Bending and torsional moments were highest (with one exception,  $M_{x_{50}}$ ) in TP3 (see Figure 3.13), which – taking into account the results of the joint reaction analysis results of the knee joint (see Figure 3.5), the results for the muscle activation (see Figure 3.4) and the kinematics displayed in Figure 2.9 – seems plausible. Moments around the x-axis (pointing posteriorly/caudally) were higher than moments around the y-axis (pointing laterally, see Figure 2.12), indicating that there was more bending of the bones “to the lateral side” than “to the front” in response to loading. One could therefore argue that recording motion of animals in 3D instead of just in one plane is even more important to obtain more accurate results.

#### 4.2.5 Comparison of FE results to other results in literature

De Souza et al. [2005], in order to validate a tibial compression model, reported strains measured with longitudinally oriented strain gauges at the tibial midshaft not only due to axial loading but also due to walking and jumping motion of female mice. They found that tensile and compressive strains predominate on the lateral and medial surfaces, respectively, which was also the case in this study (compare Figure 3.12, column on the right). Value-wise, the results although differ. While De Souza et al. [2005] report approx.  $200 \mu\epsilon$  and  $-300 \mu\epsilon$  for normal walking activity (although stating that they did not necessarily record peak strains due to strain gauge placement), the corresponding values of the present study are between  $-2516 \mu\epsilon$  and  $4847 \mu\epsilon$  along the longitudinal axis. This is more than a tenth-fold increase. Also when comparing the running motion of the present study to a 30 cm jump also recorded by De Souza et al. [2005], where close to  $-600 \mu\epsilon$  and  $400 \mu\epsilon$  were measured, the present study results are a lot higher. The tested loads during the tibial compression test, ranging from five to 13 N, elicited compressive and tensile strains of  $-1500 \mu\epsilon$  and  $2000 \mu\epsilon$ , still significantly below the calculated strains of this study, but also influenced by the strain gauge placement.

Prasad et al. [2010], whose MS model and kinematics to gain the loading conditions were already discussed above, reported peak tensile and compressive strains at the diaphyseal cross-section, 1.5 mm proximal to the tibia-fibula junction. This could come close to the 50% cross section of this study. They reported values in a similar range as De Souza et al. [2005] did, with maximum tensile strains of  $321 \pm 25 \mu\epsilon$  and maximum compressive strains of  $-368 \pm 30 \mu\epsilon$ . As observed in this study, they also note that the neutral axis rotated minimally during stance phase and the strain profile reported by them matches the one gained in this study nicely after adjusting for the different orientations by rotating by 90 degrees.

Peak tensile strains for walking activity in this range were also reported by Sugiyama et al. [2012], stating that a dynamic peak load of 2 N in the tibial compression test resulted in similar levels of peak strain. A compressive strain of  $-5000 \mu\epsilon$  arose under loading with the highest dynamic load magnitude of 14 N, which, according to the authors, occurs during vigorous activities in animals. The maximum strain values of this study,  $-7424 \mu\epsilon$  and  $7302 \mu\epsilon$  for the 50% section, are larger than this, but not by much.

Comparing the results of the present study to the results of Pickering et al. [2021], who reported strain profiles induced by a 10 N tibial compression test and gained with a similar FE model, the range of occurring strains match well. With an elastic modulus of 17 GPa, Pickering et al. [2021] reported maximum values of around  $-6000 \mu\epsilon$  and  $4000 \mu\epsilon$  for the 37% section, for which in the present study, values of  $5086 \mu\epsilon$  and  $-4937 \mu\epsilon$  were calculated.

To conclude, experimental data in literature in general supports strain values much lower (by factor 10) than found in this study. The data are mostly gained in combination with the tibial compression test (De Souza et al. [2005], Sugiyama et al. [2012], Patel et al. [2014]), where no forces are acting on the bone due to muscle activity. Strains during walking and jumping are also reported (De Souza et al. [2005], Prasad et al. [2010]), but either the authors themselves note that the reported values are not the maximum strains that occur due to limitations in strain gauge placement, or it is unclear whether the reported data are peak values in the strict sense or rather average values over a wide area.

### 4.3 Limitations

One of the main limitations of this work is the quality of the input data for the musculoskeletal model. The kinematics recorded by Charles et al. [2018], despite being, to the best of our knowledge, the open-source available online, are compromised by the fact that they were recorded at running speeds almost twice as high as considered normal cage running speeds (Neumann et al. [2009], Serradj and Jamon [2009]) and used by other studies (Prasad et al. [2010], Dienes et al. [2022]). Furthermore, joint angles were derived from digitized landmark coordinates of single strides, recorded with cameras from the lateral and dorsal view. As Dienes et al. [2022] point out, values for sagittal plane kinematics reported in literature vary significantly in their raw angles. Information on circumduction or vaulting, classic compensation patterns in rodents, are missed by 2D motion capture evaluating solely the sagittal plane. Charles et al. [2018] did also incorporate information of the dorsal view, but this does not result in the recording of full 3D gait kinematics as can be gained by reflective marker recordings. However, it must also be noted that the size of mice, even more so in comparison to the rats of Dienes et al. [2022], makes the use of 3D reflective marker motion capture more difficult and its applicability limited.

In the 2018 model, no GRFs are implemented in the mediolateral (ML) direction. The reason given by Charles et al. [2018] is that the recorded data was too noisy to be accurately included in the simulation. However, the 2024 model contains GRFs in ML direction that are considerably high. When comparing the curves in Figure 2.5, it can be guessed that the course of these was adapted to the course of the vertical GRF, as the curves are very similar after an initial drop of ML. As Schmitt et al. [2010] point out, the ML component is still little researched, mainly because of its high variability, but in contrast to the rather high progression across the stance phase assumed by James Charles, they state that it is also usually relatively small, often less than 10% of an animal's body weight.

While care was taken to use data from as few different mice as possible for the input to the FE model (according to Charles et al. [2018], the kinematics used to actuate the model were recorded on a different mouse than the mouse used in the anatomy study to build the MS model), the FE model itself was not generated on  $\mu$ CT data of the mouse used for the MS model. This could not be avoided.

As knee joint kinetics serve as an input to the FE model, one limitation is the simplicity of the knee joint modeled as a simple hinge joint, as more elaborate and physiological models exist in literature (Andersen et al. [2017]). An implementation of a more physiological joint was although out of scope for this project.

Next, the way in which the forces and moments are applied and the boundary conditions have great potential for improvement. As Bavi et al. [2024] point out, constraining the distal end in all DOFs is anything but physiological, as all muscles that run over the ankle joint but attach to the tibia and thereby exert a force on it must be excluded. Furthermore, the dynamics of the neuromuscular-skeletal system, which is used to calculate the forces and moments, are not respected. However, in accordance with the interest in the 37% and 50% section at the proximal end of the bone, this limitation was accepted.

Another limitation concerns the occurrence of inconsistent and counterintuitive results in relation to the increased stress results using a higher elastic (tensile) modulus and the subtraction or reduction of certain muscle forces, as already discussed in Sections 4.2.1 and 4.2.2. Future work will include revising this aspect, which may lead to improved (i.e., more reliable) results provided by the FE analysis. Nevertheless, it should be emphasized that the model does provide stress and strain distributions that appear to be correct, considering for comparison the results of Prasad et al. [2010]. Ascertaining the exact reasons of the reported numerical anomalies was beyond the scope of this thesis — additional in-depth studies, including revisiting the numerical implementation are necessary to validate the reported results.

## Conclusion

In summary, this work developed a comprehensive modeling pipeline for the assessment of stress and strain patterns in the mouse tibia during the stance phase. To achieve this, an MS mouse hindlimb model was used first to obtain physiological loading conditions for the subsequent FE analysis step. These include joint reaction forces and moments as well as forces of muscles attaching to the proximal part of the tibia. With the FE model, stresses and strains were determined at two sections of interest (37% and 50% viewed proximally) and bending and torsional moments were calculated.

To explore different applications of this technique, three different simulation settings were investigated. It was shown that muscles that attach near a section of interest with moderate exertions of force do not have a strong influence on the stress and strain profiles in that section thanks to the specific implementation. The simulation with only five muscles implemented showed completely different results to the simulation with all muscles included and further studies not reported in the present thesis revealed general inconsistencies regarding the inclusion of muscles. Any conclusions drawn from these results must therefore be regarded with caution. It was also shown that an increase in elastic (tensile) modulus did not necessarily result in a reduction of stresses as expected. Sources for this mismatch remain to be identified.

For the future, attention can be focused on identifying the reasons for the inconsistent behavior, for example by creating another, differently meshed model and repeating the analyses. In addition, better and more substantiated kinematic and kinetic input to the MS model and more physiological, less simplified boundary and loading conditions for the FE model could be implemented. Nevertheless, the developed approach to determine spatio-temporal stress and strain patterns in the murine tibia in response to loading induced by habitual movement may be considered a significant step beyond the state-of-the-art in the field.



# Appendix

## Additional figures

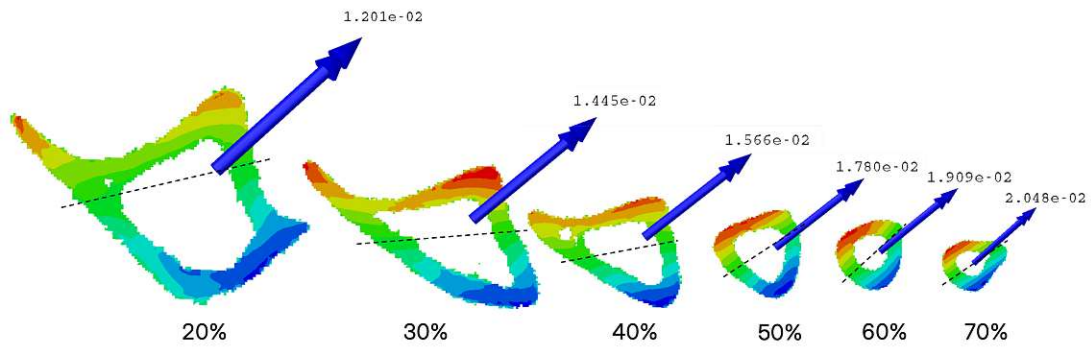


Figure 6.1: Resultant moment over sections for TP3, E = 17 GPa

## Input data to the FE model

### Location of knee joint in space [m]

<b>x</b>	0.0019138
<b>y</b>	0.0027233
<b>z</b>	0.0184996

### Joint reaction analysis output, [N] and [Nm]

	$F_x$	$F_y$	$F_z$	$M_x$	$M_y$	$M_z$
<b>TP1</b>	0.1947	-0.73202	0.013668	-0.001627	-0.000358	-0.000088
<b>TP2</b>	0.59634	-0.9538	-0.39299	0.0049371	0.0013727	0.0000285
<b>TP3</b>	1.1526	-0.93934	-0.438	0.0048663	0.0023288	0.0001286
<b>TP4</b>	0.17713	-0.10958	-0.009644	-0.000059	-0.000040	0.0000018

Table 6.1: Input data for the FE model regarding the location of the knee joint and knee joint reaction forces and moments.

	BFP_caudal	BFP_cranial	BFP_mid	RF	SM	SOL	ST	TP	VI	VL	VM
<b>Attachments on bone surface [m]</b>											
<b>x</b>	0.004124	0.002359	0.003707	0.001164	0.001774	0.003789	0.001697	0.002185	0.001138	0.001231	0.001089
<b>y</b>	0.002739	0.003174	0.003476	0.002035	0.000253	0.002208	0.000309	0.002137	0.001985	0.002083	0.001959
<b>z</b>	0.013611	0.017120	0.015689	0.016951	0.014741	0.010552	0.012597	0.015296	0.016854	0.016957	0.016930
<b>Components of force in main axes tp1 [N]</b>											
<b>x</b>	0.010035	0.036264	0.017834	-0.012819	0.168066	0.000127	0.015199	0.000263	-0.000580	-0.006962	-0.002382
<b>y</b>	-0.000233	0.002361	0.000910	0.005174	0.049753	-0.000021	0.002519	-0.000202	0.000261	0.003124	0.000528
<b>z</b>	0.013911	0.049934	0.026090	0.034200	0.229567	-0.001189	0.019639	-0.002379	0.002441	0.019074	0.007546
<b>Components of force in main axes tp2 [N]</b>											
<b>x</b>	-0.000145	0.000262	-0.000195	-0.008692	-0.000046	0.001429	-0.000586	0.001863	-0.001926	-0.202555	-0.026202
<b>y</b>	0.000004	0.000013	-0.000007	0.003508	-0.000011	-0.000239	-0.000080	-0.001448	0.000868	0.090894	0.005807
<b>z</b>	-0.000117	0.000183	-0.000146	0.023188	-0.000036	-0.013397	-0.000443	-0.017220	0.008103	0.554948	0.082989
<b>Components of force in main axes tp3 [N]</b>											
<b>x</b>	0.000591	0.000783	0.000485	-0.195998	0.002484	0.000503	0.000620	0.000922	-0.001621	-0.201203	-0.024264
<b>y</b>	-0.000023	0.000035	0.000016	0.079102	0.000616	-0.000085	0.000085	-0.000720	0.000731	0.090287	0.005378
<b>z</b>	0.000370	0.000364	0.000255	0.522910	0.001446	-0.004748	0.000366	-0.008566	0.006822	0.551243	0.076852
<b>Components of force in main axes tp4 [N]</b>											
<b>x</b>	0.005521	0.007265	0.006536	-0.019243	0.017510	0.000080	0.011950	0.000246	-0.000605	-0.024027	-0.003671
<b>y</b>	-0.000244	0.000352	0.000239	0.007766	0.004822	-0.000019	0.001904	-0.000196	0.000273	0.010782	0.000814
<b>z</b>	0.004308	0.004390	0.004512	0.051338	0.012998	-0.001009	0.009023	-0.002274	0.002545	0.065827	0.011626

Table 6.2: Input data for the FE model regarding muscles.

# List of Figures

1.1	Differentiation paths of bone cells	2
1.2	Interplay between different cytokines	3
1.3	Bone remodeling cycle	4
1.4	Homeostatic bone adaptation mechanism	6
1.5	Schematic drawing of the tibial compression test	8
2.1	Workflows used for this work	11
2.2	Mouse hindlimb model version 2018	12
2.3	Mouse hindlimb model version 2024	12
2.4	Kinematic input to the workflow provided by Charles et al. [2018]	13
2.5	Ground reaction forces recorded by Charles et al. [2018]	13
2.6	The inverse problem	13
2.7	Coordinate reference frames	15
2.8	Difference between anatomical and effective attachment sites	15
2.9	Overview over time points	17
2.10	Result of the registering of bones on top of each other	18
2.11	Comparison of meshes	19
2.12	Voxel-based FE model used for the analysis	19
2.13	Location of knee joint reference point and multi-point constrained area on the tibial plateau	20
2.14	Illustration of the locations of the sections of interest	20
2.15	Multi point constraint schematic drawing	20
2.16	Location and size of smaller multi-point constrained area on the tibial plateau tested	21
3.1	Muscle forces of the 2018 model	23
3.2	AJR results for knee joint, 2018 version	24
3.3	AJR results for ankle joint, 2018 version	25
3.4	Muscle forces of the 2024 model	25
3.5	AJR results for knee joint, 2024 version	26
3.6	AJR results for ankle joint, 2024 version	27
3.7	Stress results for the 37% section, E = 17 GPa	28
3.8	Stress results for the 50% section, E = 17 GPa	29
3.9	Shear stress results for the 37% section, E = 17 GPa	30
3.10	Shear stress results for the 50% section, E = 17 GPa	31
3.11	Strain results for the 37% section, E = 17 GPa	32
3.12	Strain results for the 50% section, E = 17 GPa	33
3.13	Graphical representation of Table 3.1	33
3.14	Stress results for the 37% section, E = 21 GPa	35
3.15	Stress results for the 50% section, E = 21 GPa	36
3.16	Shear stress results for the 37% section, E = 21 GPa	37
3.17	Shear stress results for the 50% section, E = 21 GPa	38
3.18	Strain results for the 37% section, E = 21 GPa	39
3.19	Strain results for the 50% section, E = 21 GPa	40
3.20	Stress results for the 30% section, E = 21 GPa, attachment site SM	40
3.21	Stress and strain results for sections 20 to 40%	41
3.22	Stress (top) and strain (bottom) results for sections 37% and 50%	42
3.23	Variation of area of force constraint	42

4.1 ID results of both models	44
4.2 Gait cycle of the 2018 model	45
4.3 Gait cycle of the 2024 model	45
4.4 AJR comparison of knee joint results	46
4.5 AJR comparison of ankle joint results	47
4.6 Comparison of inverse dynamics results of both models to Dienes results	48
4.7 Stress results into y-direction of TP3 for better comparison	49
4.8 Variation of the elastic (tensile) modulus	51
4.9 Comparison of stress profiles along the proximal bone	52
6.1 Resultant moment over sections for TP3, E = 17 GPa	57

# List of Tables

2.1 Attachment point modeling of included muscles in the model. . . . .	16
3.1 Bending and torsional moments for all time points, E = 17 GPa. . . . .	31
3.2 Maximum values of the FE simulations for 17 GPa and 21 GPa. . . . .	41
4.1 Comparison of the model used by Prasad et al. [2010] to the model used in this study . . . . .	48
4.2 Forces normal to 37% and 50% sections given in N. . . . .	50
6.1 Input data for the FE model regarding the location of the knee joint and knee joint reaction forces and moments. . . . .	57
6.2 Input data for the FE model regarding muscles. . . . .	58



# Bibliography

- E. M. Aarden, P. J. Nijweide, and E. H. Burger. Function of osteocytes in bone. *Journal of Cellular Biochemistry*, 55(3):287–299, 1994. doi: <https://doi.org/10.1002/jcb.240550304>
- A. N. Ahn, E. Furrow, and A. A. Biewener. Walking and running in the red-legged running frog, *kassina maculata*. *Journal of Experimental Biology*, 207(3):399–410, 2004. doi: <https://doi.org/10.1242/jeb.00761>.
- T. Akay, H. J. Acharya, K. Fouad, and K. G. Pearson. Behavioral and electromyographic characterization of mice lacking epha4 receptors. *Journal of Neurophysiology*, 96(2):642–651, 2006. doi: <https://doi.org/10.1152/jn.00174.2006>.
- M. S. Andersen, M. De Zee, M. Damsgaard, D. Nolte, and J. Rasmussen. Introduction to force-dependent kinematics: theory and application to mandible modeling. *Journal of Biomechanical Engineering*, 139(9):091001, 2017.
- A. Y. Babil, E. Eghan-Acquah, L. E. Diamond, R. Barrett, C. P. Carty, M. Barzan, A. Nasser, D. G. Lloyd, D. J. Saxby, and S. Feih. Effect of different constraining boundary conditions on simulated femoral stresses and strains during gait. *Scientific Reports*, 14(1):10808, 2024. doi: <https://doi.org/10.1038/s41598-024-61305-x>.
- P. J. Besl and N. D. McKay. Method for registration of 3-d shapes. In *Sensor Fusion IV: Control Paradigms and Data Structures*, volume 1611, pages 586–606, 1992. doi: <https://doi.org/10.1109/34.121791>.
- L. F. Bonewald and M. L. Johnson. Osteocytes, mechanosensing and wnt signaling. *Bone*, 42(4):606–615, 2008. doi: <https://doi.org/10.1016/j.bone.2007.12.224>.
- J. B. M. Bourguery. *Traité complet de l’anatomie de l’homme*. *Osteologie*, 1832.
- D. B. Burr. Muscle strength, bone mass, and age-related bone loss. *Journal of Bone and Mineral Research*, 12(10):1547–1551, 1997. doi: <https://doi.org/10.1359/jbmr.1997.12.10.1547>.
- D. B. Burr, C. Milgrom, D. Fyhrie, M. Forwood, M. Nyska, A. Finestone, S. Hoshaw, E. Saiag, and A. Simkin. In vivo measurement of human tibial strains during vigorous activity. *Bone*, 18(5):405–410, 1996. doi: [https://doi.org/10.1016/8756-3282\(96\)00028-2](https://doi.org/10.1016/8756-3282(96)00028-2).
- T. J. Chambers, J. A. Darby, and K. Fuller. Mammalian collagenase predisposes bone surfaces to osteoclastic resorption. *Cell and Tissue Research*, 241:671–675, 1985. doi: <https://doi.org/10.1007/BF00214590>.
- J. P. Charles, O. Cappellari, A. J. Spence, D. J. Wells, and J. R. Hutchinson. Muscle moment arms and sensitivity analysis of a mouse hindlimb musculoskeletal model. *Journal of Anatomy*, 229(4):514–535, 2016. doi: <https://doi.org/10.1111/joa.12461>.
- J. P. Charles, O. Cappellari, and J. R. Hutchinson. A dynamic simulation of musculoskeletal function in the mouse hindlimb during trotting locomotion. *Frontiers in Bioengineering and Biotechnology*, 6:61, 2018. doi: <https://doi.org/10.3389/fbioe.2018.00061>.
- Y. Chen and G. Medioni. Object modelling by registration of multiple range images. *Image and Vision Computing*, 10(3):145–155, 1992. doi: [https://doi.org/10.1016/0262-8856\(92\)90066-C](https://doi.org/10.1016/0262-8856(92)90066-C).

- P. Cignoni, M. Callieri, M. Corsini, M. Dellepiane, F. Ganovelli, and G. Ranzuglia. Mesh-Lab: an Open-Source Mesh Processing Tool. In V. Scarano, R. D. Chiara, and U. Erra, editors, *Eurographics Italian Chapter Conference*, 2008. ISBN 978-3-905673-68-5. doi: <https://doi.org/10.2312/LocalChapterEvents/ItalChap/ItalianChapConf2008/129-136>.
- K. A. Clarke and J. Still. Gait analysis in the mouse. *Physiology & Behavior*, 66(5):723–729, 1999. doi: [https://doi.org/10.1016/S0031-9384\(98\)00343-6](https://doi.org/10.1016/S0031-9384(98)00343-6).
- J. C. Crockett, M. J. Rogers, F. P. Coxon, L. J. Hocking, and M. H. Helfrich. Bone remodelling at a glance. *Journal of Cell Science*, 124(7):991–998, 2011. doi: <https://doi.org/10.1242/jcs.063032>.
- R. D. Crowninshield. Use of optimization techniques to predict muscle forces. *Journal of Biomechanical Engineering*, 100:88–92, 1978. doi: <https://doi.org/10.1115/1.3426197>.
- J. Currey. What should bones be designed to do? *Calcified Tissue International*, 36:7–10, 1984. doi: <https://doi.org/10.1007/BF02406127>.
- R. L. De Souza, M. Matsuura, F. Eckstein, S. C. F. Rawlinson, L. E. Lanyon, and A. A. Pitsillides. Non-invasive axial loading of mouse tibiae increases cortical bone formation and modifies trabecular organization: a new model to study cortical and cancellous compartments in a single loaded element. *Bone*, 37(6):810–818, 2005. doi: <https://doi.org/10.1016/j.bone.2005.07.022>.
- S. L. Delp, F. C. Anderson, A. S. Arnold, P. Loan, A. Habib, C. T. John, E. Guendelman, and D. G. Thelen. Opensim: open-source software to create and analyze dynamic simulations of movement. *IEEE Transactions on Biomedical Engineering*, 54(11):1940–1950, 2007. doi: <https://doi.org/10.1109/TBME.2007.901024>.
- J. Dienes, B. Hicks, C. Slater, K. D. Janson, G. J. Christ, and S. D. Russell. Comprehensive dynamic and kinematic analysis of the rodent hindlimb during over ground walking. *Scientific Reports*, 12(1):19725, 2022. doi: <https://doi.org/10.1038/s41598-022-20288-3>.
- J. A. Dienes, X. Hu, K. D. Janson, C. Slater, E. A. Dooley, G. J. Christ, and S. D. Russell. Analysis and modeling of rat gait biomechanical deficits in response to volumetric muscle loss injury. *Frontiers in Bioengineering and Biotechnology*, 7:146, 2019. doi: <https://doi.org/10.3389/fbioe.2019.00146>.
- A. Erdemir, T. M. Guess, J. Halloran, S. C. Tadepalli, and T. M. Morrison. Considerations for reporting finite element analysis studies in biomechanics. *Journal of Biomechanics*, 45(4): 625–633, 2012. doi: <https://doi.org/10.1016/j.jbiomech.2011.11.038>.
- F. G. Evans. *Stress and strain in bones*. Charles C. Thomas, Springfield, IL, 1957.
- M. R. Forwood and C. H. Turner. Skeletal adaptations to mechanical usage: results from tibial loading studies in rats. *Bone*, 17(4):197–205, 1995. doi: [https://doi.org/10.1016/8756-3282\(95\)00292-L](https://doi.org/10.1016/8756-3282(95)00292-L).
- S. P. Fritton and C. T. Rubin. In vivo measurement of bone deformations using strain gauges. In *Bone Mechanics Handbook*, pages 8–34. CRC Press, Boca Raton, 2001.
- H. M. Frost. Bone “mass” and the “mechanostat”: a proposal. *The Anatomical Record*, 219(1): 1–9, 1987. doi: <https://doi.org/10.1002/ar.1092190104>.
- H. M. Frost. On our age-related bone loss: Insights from a new paradigm. *Journal of Bone and Mineral Research*, 12(10):1539–1546, 1997. doi: <https://doi.org/10.1359/jbmr.1997.12.10.1539>.
- H. M. Frost. The utah paradigm of skeletal physiology: an overview of its insights for bone, cartilage and collagenous tissue organs. *Journal of Bone and Mineral Metabolism*, 18:305–316, 2000. doi: <https://doi.org/10.1007/s007740070001>.
- H. M. Frost. Bone’s mechanostat: a 2003 update. *The Anatomical Record Part A: Discoveries in Molecular, Cellular, and Evolutionary Biology: an Official Publication of the American Association of Anatomists*, 275(2):1081–1101, 2003. doi: <https://doi.org/10.1002/ar.a.10119>.

- R. J. Full and M. S. Tu. Mechanics of a rapid running insect: two-, four- and six-legged locomotion. *Journal of Experimental Biology*, 156(1):215–231, 1991. doi: <https://doi.org/10.1242/jeb.156.1.215>.
- Y. C. Fung and R. Skalak. *Biomechanics: mechanical properties of living tissues*. Springer Science+Business Media New York, 1981. doi: <https://doi.org/10.1007/978-1-4757-2257-4>.
- B. G. Galerkin. Series solution of some problems of elastic equilibrium of rods and plates. *Vestnik inzhenerov i tekhnikov*, 19(7):897–908, 1915.
- G. Galilei. *Discorsi e dimostrazioni matematiche intorno a due nuove scienze*. Lodewijk Elzevir, Leiden, 1638.
- T. S. Gross, S. Srinivasan, C. C. Liu, T. L. Clemens, and S. D. Bain. Noninvasive loading of the murine tibia: an in vivo model for the study of mechanotransduction. *Journal of Bone and Mineral Research*, 17(3):493–501, 2002. doi: <https://doi.org/10.1359/jbmr.2002.17.3.493>.
- G. F. Harris and J. J. Wertsch. Procedures for gait analysis. *Archives of Physical Medicine and Rehabilitation*, 75(2):216–225, 1994. doi: [https://doi.org/10.1016/0003-9993\(94\)90399-9](https://doi.org/10.1016/0003-9993(94)90399-9).
- W. C. Hayes and B. Snyder. Towards a quantitative formulation of Wolff's law in trabecular bone. *Mechanical Properties of Bone*, 45, 1981.
- N. C. Heglund. A simple design for a force-plate to measure ground reaction forces. *Journal of Experimental Biology*, 93(1):333–338, 1981. doi: <https://doi.org/10.1242/jeb.93.1.333>.
- H. D. Hibbitt. Abaqus/epgen—a general purpose finite element code with emphasis on nonlinear applications. *Nuclear Engineering and Design*, 77(3):271–297, 1984. doi: [https://doi.org/10.1016/0029-5493\(84\)90106-7](https://doi.org/10.1016/0029-5493(84)90106-7).
- James Charles. Private communication, 12.11.2024 and 18.11.2024.
- Z. F. G. Jaworski. Lamellar bone turnover system and its effector organ. *Calcified Tissue International*, 36:46–55, 1984. doi: <https://doi.org/10.1007/BF02406133>.
- Z. F. G. Jaworski, M. Liskova-Kiar, and H. K. Uhthoff. Effect of long-term immobilisation on the pattern of bone loss in older dogs. *The Journal of Bone & Joint Surgery British Volume*, 62(1):104–110, 1980. doi: <https://doi.org/10.1302/0301-620X.62B1.6985912>.
- W. S. Jee, T. J. Wronski, E. R. Morey, and D. B. Kimmel. Effects of spaceflight on trabecular bone in rats. *American Journal of Physiology-Regulatory, Integrative and Comparative Physiology*, 244(3):310–314, 1983. doi: <https://doi.org/10.1152/ajpregu.1983.244.3.R310>.
- W. L. Johnson, D. L. Jindrich, R. R. Roy, and V. R. Edgerton. A three-dimensional model of the rat hindlimb: musculoskeletal geometry and muscle moment arms. *Journal of Biomechanics*, 41(3):610–619, 2008. doi: <https://doi.org/10.1016/j.jbiomech.2007.10.004>.
- G. Karsenty, H. M. Kronenberg, and C. Settembre. Genetic control of bone formation. *Annual Review of Cell and Developmental Biology*, 25(1):629–648, 2009. doi: [10.1146/annurev.cellbio.042308.113308](https://doi.org/10.1146/annurev.cellbio.042308.113308).
- P. Katsimbri. The biology of normal bone remodelling. *European Journal of Cancer Care*, 26(6): 1–5, 2017. doi: <https://doi.org/10.1111/ecc.12740>.
- J. S. Kenkre and J. H. D. Bassett. The bone remodelling cycle. *Annals of Clinical Biochemistry*, 55(3):308–327, 2018. doi: <https://doi.org/10.1177/0004563218759371>.
- M. Korn, M. Holzkothen, and J. Pauli. Color supported generalized-icp. In *2014 International Conference on Computer Vision Theory and Applications (VISAPP)*, volume 3, pages 592–599. IEEE, 2014. doi: <https://doi.org/10.5220/0004692805920599>.
- J. Kular, J. Tickner, S. M. Chim, and J. Xu. An overview of the regulation of bone remodelling at the cellular level. *Clinical Biochemistry*, 45(12):863–873, 2012. doi: <https://doi.org/10.1016/j.clinbiochem.2012.03.021>.

- L. E. Lanyon. Functional strain as a determinant for bone remodeling. *Calcified Tissue International*, 36:56–61, 1984. doi: <https://doi.org/10.1007/BF02406134>.
- L. E. Lanyon. Functional strain in bone tissue as an objective, and controlling stimulus for adaptive bone remodelling. *Journal of Biomechanics*, 20(11-12):1083–1093, 1987. doi: [https://doi.org/10.1016/0021-9290\(87\)90026-1](https://doi.org/10.1016/0021-9290(87)90026-1).
- L. E. Lanyon. Osteocytes, strain detection, bone modeling and remodeling. *Calcified Tissue International*, 53:102–107, 1993. doi: <https://doi.org/10.1007/BF01673415>.
- L. E. Lanyon. Using functional loading to influence bone mass and architecture: objectives, mechanisms, and relationship with estrogen of the mechanically adaptive process in bone. *Bone*, 18(1):S37–S43, 1996. doi: [https://doi.org/10.1016/8756-3282\(95\)00378-9](https://doi.org/10.1016/8756-3282(95)00378-9).
- H. Leblond, M. L'Espérance, D. Orsal, and S. Rossignol. Treadmill locomotion in the intact and spinal mouse. *Journal of Neuroscience*, 23(36):11411–11419, 2003. doi: <https://doi.org/10.1523/JNEUROSCI.23-36-11411.2003>.
- E. M. Lepicard, P. Venault, A. Abourachid, E. Pellé, G. Chapouthier, and J.-P. Gasc. Spatio-temporal analysis of locomotion in balb/cbyj and c57bl/6j mice in different environmental conditions. *Behavioural Brain Research*, 167(2):365–372, 2006. doi: <https://doi.org/10.1016/j.bbr.2005.10.001>.
- T. W. Lu. Influence of muscle activity on the forces in the femur: an in-vivo study. *Journal of Biomechanics*, 30:1101–1106, 1997. doi: [https://doi.org/10.1016/S0021-9290\(97\)00090-0](https://doi.org/10.1016/S0021-9290(97)00090-0).
- R. B. Martin, D. B. Burr, and N. A. Sharkey. *Skeletal Tissue Mechanics*. Springer New York, NY, 1998. doi: <https://doi.org/10.1007/978-1-4757-2968-9>.
- G. H. Meyer. Die architektur der spongiosa. *Archiv für Anatomie, Physiologie und wissenschaftliche Medizin*, 34:615–628, 1867.
- M. Millard, T. Uchida, A. Seth, and S. L. Delp. Flexing computational muscle: modeling and simulation of musculotendon dynamics. *Journal of Biomechanical Engineering*, 135(2): 021005–1–021005–11, 2013. doi: <https://doi.org/10.1115/1.4023390>.
- J. R. Mosley, B. M. March, J. Lynch, and L. E. Lanyon. Strain magnitude related changes in whole bone architecture in growing rats. *Bone*, 20(3):191–198, 1997. doi: [https://doi.org/10.1016/S8756-3282\(96\)00385-7](https://doi.org/10.1016/S8756-3282(96)00385-7).
- M. Neumann, Y. Wang, S. Kim, S. M. Hong, L. Jeng, M. Bilgen, and J. Liu. Assessing gait impairment following experimental traumatic brain injury in mice. *Journal of Neuroscience Methods*, 176(1):34–44, 2009. doi: <https://doi.org/10.1016/j.jneumeth.2008.08.026>.
- J. Park, Q. Zhou, and V. Koltun. Colored point cloud registration revisited. In *Proceedings of the IEEE international Conference on Computer Vision*, pages 143–152, 2017. doi: <https://doi.org/10.1109/ICCV.2017.25>.
- T. K. Patel, M. D. Brodt, and M. J. Silva. Experimental and finite element analysis of strains induced by axial tibial compression in young-adult and old female c57bl/6 mice. *Journal of Biomechanics*, 47(2):451–457, 2014. doi: <https://doi.org/10.1016/j.jbiomech.2013.10.052>.
- A. T. M. Phillips, C. C. Villette, and L. Modenese. Femoral bone mesoscale structural architecture prediction using musculoskeletal and finite element modelling. *International Biomechanics*, 2(1):43–61, 2015. doi: <https://doi.org/10.1080/23335432.2015.1017609>.
- E. Pickering, M. J. Silva, P. Delisser, M. D. Brodt, Y. Gu, and P. Pivonka. Estimation of load conditions and strain distribution for in vivo murine tibia compression loading using experimentally informed finite element models. *Journal of Biomechanics*, 115:110–140, 2021. doi: <https://doi.org/10.1016/j.jbiomech.2020.110140>.
- P. Pivonka and S. V. Komarova. Mathematical modeling in bone biology: From intracellular signaling to tissue mechanics. *Bone*, 47(2):181–189, 2010. doi: <https://doi.org/10.1016/j.bone.2010.04.601>.

- P. Pivonka, J. Zimak, D. W. Smith, B. S. Gardiner, C. R. Dunstan, N. A. Sims, T. J. Martin, and G. R. Mundy. Model structure and control of bone remodeling: a theoretical study. *Bone*, 43(2):249–263, 2008. doi: <https://doi.org/10.1016/j.bone.2008.03.025>.
- P. Pivonka, A. Park, and M. R. Forwood. Functional adaptation of bone: the mechanostat and beyond. In *Multiscale Mechanobiology of Bone Remodeling and Adaptation*, pages 1–60. Springer, 2017. doi: [https://doi.org/10.1007/978-3-319-58845-2\\_1](https://doi.org/10.1007/978-3-319-58845-2_1).
- J. Prasad, B. P. Wiater, S. E. Nork, S. D. Bain, and T. S. Gross. Characterizing gait induced normal strains in a murine tibia cortical bone defect model. *Journal of Biomechanics*, 43(14):2765–2770, 2010. doi: <https://doi.org/10.1016/j.jbiomech.2010.06.030>.
- W. Ritz. Über eine neue methode zur lösung gewisser variationsprobleme der mathematischen physik. *Journal für die reine und angewandte Mathematik*, 1909. doi: <https://doi.org/10.1515/crll.1909.135.1>.
- J. R. Rochester and K. A. Clarke. Gait analysis in the rat as a model for the study of peripheral vascular disease. *Physiology & Behavior*, 55(4):723–726, 1994. doi: [https://doi.org/10.1016/0031-9384\(94\)90051-5](https://doi.org/10.1016/0031-9384(94)90051-5).
- H. Roesler. The history of some fundamental concepts in bone biomechanics. *Journal of Biomechanics*, 20(11-12):1025–1034, 1987. doi: [https://doi.org/10.1016/0021-9290\(87\)90020-0](https://doi.org/10.1016/0021-9290(87)90020-0).
- W. Roux. Der züchtende kampf der teile, oder die 'teilauslese' im organismus. (theorie der funktionellen anpassung'). *Wilhelm Engelmann*, 1881.
- C. T. Rubin and L. E. Lanyon. Regulation of bone mass by mechanical strain magnitude. *Calcified Tissue International*, 37:411–417, 1985.
- N. Rucci. Molecular biology of bone remodelling. *Clinical Cases in Mineral and Bone Metabolism*, 5(1):49–56, 2008.
- D. Schmitt, A. C. Zumwalt, and M. W. Hamrick. The relationship between bone mechanical properties and ground reaction forces in normal and hypermuscular mice. *Journal of Experimental Zoology Part A: Ecological Genetics and Physiology*, 313(6):339–351, 2010. doi: <https://doi.org/10.1002/jez.604>.
- E. Schönau. Paediatric osteology: new developments in diagnostics and therapy. In *Excerpta Medica. International congress series*. Elsevier Science Publishers, 1996.
- L. M. Schutte, M. M. Rodgers, F. E. Zajac, and R. M. Glaser. Improving the efficacy of electrical stimulation-induced leg cycle ergometry: an analysis based on a dynamic musculoskeletal model. *IEEE Transactions on Rehabilitation Engineering*, 1(2):109–125, 1993. doi: <https://doi.org/10.1109/86.242425>.
- A. Segal, D. Haehnel, and S. Thrun. Generalized-icp. In *Robotics: Science and Systems*, volume 2, page 435, 2009. doi: <https://doi.org/10.15607/RSS.2009.V.021>.
- N. Serradj and M. Jamon. The adaptation of limb kinematics to increasing walking speeds in freely moving mice 129/sv and c57bl/6. *Behavioural Brain Research*, 201(1):59–65, 2009. doi: <https://doi.org/10.1016/j.bbr.2009.01.030>.
- A. Seth, J. L. Hicks, T. K. Uchida, A. Habib, C. L. Dembia, J. J. Dunne, C. F. Ong, M. S. DeMers, A. Rajagopal, M. Millard, et al. Opensim: Simulating musculoskeletal dynamics and neuromuscular control to study human and animal movement. *PLoS Computational Biology*, 14(7):e1006223, 2018. doi: <https://doi.org/10.1371/journal.pcbi.1006223>.
- M. A. Sherman, A. Seth, and S. L. Delp. Simbody: multibody dynamics for biomedical research. *Procedia Iutam*, 2:241–261, 2011. doi: <https://doi.org/10.1016/j.piutam.2011.04.023>.
- T. M. Skerry. One mechanostat or many? modifications of the site-specific response of bone to mechanical loading by nature and nurture. *Journal of Musculoskeletal and Neuronal Interactions*, 6(2):122–127, 2006.

- R. V. Southwell. *Relaxation methods in theoretical physics: a continuation of the treatise Relaxation methods in engineering science*. Clarendon Press Oxford, 1946.
- T. Sugiyama, A. Yamaguchi, and S. Kawai. Effects of skeletal loading on bone mass and compensation mechanism in bone: a new insight into the “mechanostat” theory. *Journal of Bone and Mineral Metabolism*, 20:196–200, 2002. doi: <https://doi.org/10.1007/s007740200028>.
- T. Sugiyama, L. B. Meakin, W. J. Browne, G. L. Galea, J. S. Price, and L. E. Lanyon. Bones’ adaptive response to mechanical loading is essentially linear between the low strains associated with disuse and the high strains associated with the lamellar/woven bone transition. *Journal of Bone and Mineral Research*, 27(8):1784–1793, 2012. doi: <https://doi.org/10.1002/jbmr.1599>.
- H. E. Takahashi. *Spinal disorders in growth and aging*. Springer, 1995.
- S. L. Teitelbaum. Osteoclasts: what do they do and how do they do it? *The American Journal of Pathology*, 170(2):427–435, 2007. doi: <https://doi.org/10.2353/ajpath.2007.060834>.
- A. G. Torrance, J. R. Mosley, R. F. L. Suswillo, and L. E. Lanyon. Noninvasive loading of the rat ulna in vivo induces a strain-related modeling response uncomplicated by trauma or periosteal pressure. *Calcified Tissue International*, 54:241–247, 1994. doi: <https://doi.org/10.1007/BF00301686>.
- C. H. Turner, M. P. Akhter, D. M. Raab, D. B. Kimmel, and R. R. Recker. A noninvasive, in vivo model for studying strain adaptive bone modeling. *Bone*, 12(2):73–79, 1991. doi: [https://doi.org/10.1016/8756-3282\(91\)90003-2](https://doi.org/10.1016/8756-3282(91)90003-2).
- C. H. Turner, M. Forwood, J. Y. Rho, and T. Yoshikawa. Mechanical loading thresholds for lamellar and woven bone formation. *Journal of Bone and Mineral Research*, 9(1):87–97, 1994. doi: <https://doi.org/10.1002/jbmr.5650090113>.
- M. J. Turner, R. W. Clough, H. C. Martin, and L. J. Topp. Stiffness and deflection analysis of complex structures. *Journal of the Aeronautical Sciences*, 23(9):805–823, 1956. doi: <https://doi.org/10.2514/8.3664>.
- R. J. van Arkel, L. Modenese, A. T. M. Phillips, and J. R. T. Jeffers. Hip abduction can prevent posterior edge loading of hip replacements. *Journal of Orthopaedic Research*, 31(8):1172–1179, 2013. doi: <https://doi.org/10.1002/jor.22364>.
- J. Wolff. Über die bedeutung der architektur der spongiosa. *Zentralblatt für die medizinische Wissenschaft*, 4:223–234, 1869.
- T. J. Wronski and E. R. Morey. Skeletal abnormalities in rats induced by simulated weightlessness. *Metabolic Bone Disease and Related Research*, 4(1):69–75, 1982. doi: [https://doi.org/10.1016/0221-8747\(82\)90011-x](https://doi.org/10.1016/0221-8747(82)90011-x).
- T. J. Wronski and E. R. Morey. Effect of spaceflight on periosteal bone formation in rats. *American Journal of Physiology-Regulatory, Integrative and Comparative Physiology*, 244(3):305–309, 1983a. doi: <https://doi.org/10.1152/ajpregu.1983.244.3.R305>.
- T. J. Wronski and E. R. Morey. Inhibition of cortical and trabecular bone formation in the long bones of immobilized monkeys. *Clinical Orthopaedics and Related Research*, 181:269–276, 1983b.
- P. Yang, G.-P. Brüggemann, and J. Rittweger. What do we currently know from in vivo bone strain measurements in humans? *Journal of Musculoskeletal and Neuronal Interactions*, 11(1):8–20, 2011.
- O. C. Zienkiewicz. The birth of the finite element method and of computational mechanics. *International Journal for Numerical Methods in Engineering*, 60(1):3–10, 2004. doi: <https://doi.org/10.1002/nme.951>.
- A. C. Zumwalt, M. Hamrick, and D. Schmitt. Force plate for measuring the ground reaction forces in small animal locomotion. *Journal of Biomechanics*, 39(15):2877–2881, 2006. doi: <https://doi.org/10.1016/j.jbiomech.2005.10.006>.